Uniwersytet
ŁÓDZKI

Wydział Fizyki i Informatyki Stosowanej

Łukasz Klepczarek

Relativistic reflection from accretion disks in Seyfert galaxies and black-hole binaries: black hole spin and geometrical parameters of the X-ray source and the disk

Praca doktorska

wykonana pod kierunkiem

prof. dr hab. Andrzeja Niedźwieckiego (promotor)

oraz

dra Michała Szaneckiego (promotor pomocniczy)

w Katedrze Astrofizyki

WFIS UŁ

Łódź 2023

Acknowledgments

I would like to thank my supervisors prof. dr hab. Andrzejowi Niedźwieckiemu and dr. Michałowi Szaneckiemu for their invaluable guidance and deep knowledge as well as for their continuous support with a great deal of patience during finalization of this thesis.

Contents

1 Introduction

The study of compact objects, i.e. white dwarfs, neutron stars, and black holes, is a central problem of modern astrophysics as they are among nature's most peculiar creations. Very high mass combined with their relatively small radius gives a very high density compared to usual atomic matter. Extreme conditions prevail around these objects, giving rise to extraordinary phenomena such as intense high-energy radiation, gamma-ray bursts, and relativistic jets. Compact objects have been studied using their electromagnetic signals for over five decades and recently also using gravitational waves, yet many details of involved physical processes remain to be understood. This dissertation focuses on some aspects of the X-ray production in the inner parts of accretion flows surrounding black holes, which can be studied through the analysis of the radiation reflected from the accretion disk. Specifically, I investigate constraints on the X-ray corona in the X-ray binary Cyg X-1 and in the Seyfert galaxy 1H 0707–495 by application of new reflection models developed in our group. I also discuss effects relevant for a proper implementation of the motion of the corona. In this introductory section, I briefly review the current state of knowledge in the study of astrophysical black holes and at the end, in Section 1.9, I summarize it and give a more specific statement of the subject of my research presented in this dissertation.

1.1 Astrophysical black holes - basic properties

The possibility of the existence of black holes emerged as a consequence of Newton's theory of gravity at the end of the 18th century when John Michell and Piere-Simon Laplace deduced that the escape velocity from the surface of an object of very high mass and very low radius can exceed the speed of light if the radius is lower than the critical radius. This would make the object completely dark and invisible for detection. In 1915, Albert Einstein published the General Theory of Relativity. The first solution to the equations of Einstein's theory by Karl Schwarzschild was the description of a non-rotating, uncharged black hole. Another more general solution describing rotating but uncharged black holes was found by Roy Kerr in 1963. In 1965, Ezra Newman generalized the Kerr solution to rotating, charged

compact objects. In this thesis, only the Kerr black holes are taken into account. To characterize these objects only two parameters are needed, namely mass M and angular momentum J. To describe the latter, it is a common practice to use a dimensionless spin parameter a, defined as:

$$a = \frac{cJ}{GM^2}, \tag{1}$$

where G is the gravitational constant and c is the speed of light. For $-1 \leq a \leq 1$ the Kerr solution has an event horizon at $R_{\rm hor} = (1 + \sqrt{1 - a^2})R_{\rm g}$, where $R_{\rm g} = GM/c^2$ is the gravitational radius. For a non-rotating black hole, $R_{\rm Sch} \equiv R_{\rm hor}(a = 0) = 2GM/c^2$ is referred to as the Schwarzschild radius.

Black holes initially attracted interest mainly from the theoretical perspective with their unique feature of having an event horizon, recognized by David Finkelstein in 1958. At that time the existence of such objects in the Universe seemed to be unrealistic to the astronomy community. Identification of the X-ray source, Cygnus X-1, in the early 1970s, as the first stellar-mass black hole candidate, and then a large number of later similar discoveries, has led to the change of the dominating view on that matter.

Direct observations of black holes are not possible, however, detection of radiation from the gas surrounding these objects is viable. Matter falling onto them may convert its gravitational potential energy into radiation and this accretion process can be very efficient energetically (Frank et al. 2002). For an object of mass M and radius R, the gravitational potential energy released by the accretion of mass m on to its surface is $\Delta E_{\rm acc} = GMm/R$ and then a higher compactness ratio M/R implies a more effective release of energy. For a characteristic radius $R \sim$ a few $R_{\rm g}$, the loss of the gravitational energy is $\Delta E_{\rm acc} \sim 0.1mc^2$. If total $\Delta E_{\rm acc}$ is converted into radiation, the radiative efficiency is $\eta \equiv L/(\dot{M}c^2) \sim 10\%$, where L is the total luminosity and $\dot{M} = {\rm d}m/{\rm d}t$ is the accretion rate.

However, the transfer of outward momentum, coming from radiation to the accreting material through scattering and absorption, can be a limiting factor for the accretion rate of such an accretion system. Assuming that the falling material is a fully ionized hydrogen and the accretion flow is spherically symmetric, the maximum luminosity, called the Eddington luminosity, can be determined by the

condition that the radiative pressure exerted on the accreting material is balanced by the gravitational force towards the centrum of mass:

$$L_{\rm Edd} = \frac{4\pi G M m_{\rm p} c}{\sigma_{\rm T}} \simeq 1.3 \times 10^{38} \left(\frac{M}{M_\odot}\right) {\rm erg\ s^{-1}} \tag{2}$$

where $m_{\rm p}$ is the proton mass, $\sigma_{\rm T}$ is the electron Thomson cross section, and $M_\odot$ is the mass of Sun. The corresponding Eddington accretion rate is $\dot{M}_{\rm Edd} = L_{\rm Edd}/c^2$ (in some works the Eddington accretion rate is defined taking into account the radiative efficiency, i.e. $\dot{M}_{\rm Edd} = L_{\rm Edd}/\eta c^2$, with typically $\eta = 0.1$).

In all real accretion systems the accreting gas will possess an angular momentum and this will lead to the formation of an accretion disk. In the classical model of a Keplerian, optically thick disk (Novikov & Thorne 1973; Shakura & Sunyaev 1973), often referred to as a Novikov-Thorne disk, the radiative efficiency is $\eta = 1 - e_{\rm ISCO}$, where $e_{\rm ISCO}$ is the specific energy at the innermost stable circular orbit (ISCO). All the basic formulae for the Kerr metric, in particular those for $R_{\rm ISCO}$ (the ISCO radius) and $e_{\rm ISCO}$, have been derived in an extremely useful article of Bardeen et al. (1972). Accretion of matter with net angular momentum spins up the black hole and the maximum value of a for accretion in Novikov-Thorne model is $a = 0.998$ (Thorne 1974). Therefore, $a = 0.998$ is the maximum value of the spin considered in astrophysical modelling. As a approaches this limit, $R_{\rm ISCO}$ decreases and η increases considerably. Specifically, $R_{\rm ISCO} = 6R_{\rm g}$ and $\eta = 0.06$ for $a = 0$, but $R_{\rm ISCO} = 2R_{\rm g}$ and $\eta = 0.19$ for $a = 0.95$, and $R_{\rm ISCO} = 1.24R_{\rm g}$ and $\eta = 0.32$ for $a = 0.998$.

Two classes of black holes were established by strong observational evidence: stellar-mass, with masses in the range $M \simeq (3 - 100)M_\odot$, and supermassive, with $M \simeq (10^5 - 10^{10})M_\odot$. The mass gap between these two classes may be partially filled by the intermediate-mass black holes, with $M \simeq (10^2 - 10^4)M_\odot$, but the evidence for their existence is not as strong as for the two other classes. The intermediate-mass black holes are not considered in this dissertation.

1.2 Stellar-mass accreting black holes

The stellar-mass black holes are formed in supernova explosions at the final stage of the evolution of heavy stars. The maximum mass of a neutron star is around

$(2-3)\ M_\odot$ (e.g. Rhoades & Ruffini 1974; Sabbadini & Hartle 1973; the exact value is not known as it depends on the equation of state of matter at nuclear and higher densities, which is currently uncertain). A final evolution product with a mass lower than this limit can be supported by the quantum neutron pressure. For a compact remnant above this limit, the gravitational collapse forms a black hole. The mass of the remnant depends on the metallicity of the progenitor star, i.e. the fraction of its mass in elements heavier than helium (as they have larger cross sections than lighter elements), which determines the mass loss rate by stellar winds. Stellar evolution simulations indicate that stellar-mass black holes may have a mass in the range $(3-100)\ M_\odot$ and at least 10^8 such objects should have been formed in our Galaxy (e.g. Brown & Bethe 1994). However, it is a challenging task to detect them. So far this has only been possible for the ones in binary systems, in which the companion object serves as a donor of the accreting matter, which generates a strong X-ray emission. The presence of a compact object is then indicated by observations of the X-ray radiation and its identification as a black hole relies on the dynamical measurement of its mass through observations of a companion star. Currently only about 20 black holes in X-ray binaries with a dynamical measurement of the mass are known (and about 50 black-hole candidates without a dynamical constraint of the mass)[1].

There are two classes of X-ray binary systems: low-mass X-ray binaries (LMXBs) and high-mass X-ray binaries (HXMBs), where *low* and *high* refers to the mass of a companion star. This classification is related to the observational appearence.

LMXBs have a stellar companion, which is less massive than the compact object, usually within $\lesssim 3M_\odot$. In these systems, a donor star transfers its mass by filling its Roche lobe. LMXBs are usually transient sources, spending most of the time in a quiescent state with a very low, often not observable, brightness in the X-ray band. The prolonged (from several months to decades) quiescent states are interrupted by outbursts, for periods ranging from days to months, during which the luminosity often increases to values comparable to the Eddington limit. Such outbursts and quiescence periods are possibly explained by the disk instability model (e.g. Lasota 2001), which explains also the outbursts observed in cataclysmic variables. In this

[1] a relatively complete list, current as of 2020, is available at https://universeathome.pl/universe/blackholes.php

mechanism the steady mass transfer from the companion builds up the quiescent disk, increasing its temperature, until it reaches the value triggering the hydrogen ionization instability, which increases the mass accretion rate. The increased accretion rate is maintained until the outer disk temperature drops below the hydrogen ionization temperature. A notable LMXB in which the outburst, observed since 1992, is much longer than in any other known LMXB is GRS 1915+105. It is still active in X-rays in 2023, although since 2018 its observed flux has dropped significantly, mostly due to Compton-thick obscuration (Miller & Homan 2023). This long duration of its outburst is likely related with its very long orbital period of 33.5 days (as compared to periods of several hours to a few days in other LMXBs), implying a very large size of the disk, which during quiescence builds up a huge reservoir of mass (Done et al. 2004). Another notable LMXB is GX 339-4, which exhibits regular outbursts every few years and allows for detailed studies of state transitions (Section 1.5).

HMXBs have a massive stellar companion, $\gtrsim 10 M_{\odot}$. They are bright, persistent sources without quiescent periods. In these systems the transfer of mass occurs regularly due to the stellar wind of the donor star. The mass accretion rate is typically much higher than in LMXBs, giving a higher outer disk temperature, which is then always above the hydrogen ionization instability. Currently only one black-hole HMXB is known in our Galaxy, Cyg X-1, and three other in nearby galaxies, LMC X-1, LMC X-3 and M33 X-7.

1.3 Active galactic nuclei

Whereas indications for the existence of stellar-mass black holes came from both the observations and the stellar-evolution theories, for supermassive black holes the arguments for their presence in the Universe are purely observational. First, concentrations of a large mass in a relatively small volume were inferred at the centers of a large number of nearby galaxies and interpreted as supermassive black holes with $M \sim 10^5 - 10^{10}\ M_{\odot}$ as the only astrophysically plausible objects satisfying the observational constraints. The strongest constraints come from observations of the motion of individual stars in the center of our Galaxy, which indicate the presence of the black hole with $M \simeq 4 \times 10^6\ M_{\odot}$ (Ghez et al. 2008), and from

studying the motion of the gas in the nucleus of NGC 4258, which indicates the presence of the black hole with $M \approx 4 \times 10^7\ M_\odot$ (Miyoshi et al. 1995). According to the current view, every galaxy, possibly except for small ones (lighter than our Galaxy), has a supermassive black hole at its center. The second piece of information came with observations of energetic phenomena in galactic nuclei that could not be attributed to stars. Particularly important was the discovery of quasars (Schmidt 1963) in which the nuclear sources outshine the rest of the host galaxies and yet show large-amplitude variations on a time of days, indicating the extremely small (in the galactic scale) size of the source. It was soon realized that this activity should be attributed to a process of accretion of matter onto a supermassive black hole (e.g. Salpeter 1964), which idea was extensively elaborated over the next two decades (as reviewed in Rees 1984).

Phenomena associated with the nuclear activity of galaxies have been independently discovered in several types of astronomical studies, which have led to a variety of empirical characterizations of these objects, collectively referred to as active galactic nuclei (AGN). In a relatively recent review Padovani et al. (2017) describe about 40 classes of AGNs defined at different levels of detail. This rich phenomenology is not specifically relevant to the main subject of this dissertation, then, I only briefly note that it can be systematized within the so-called unification model (Antonucci 1993; Urry & Padovani 1995). The two basic classes are radio-loud (about 10%) and radio-quiet (about 90%) AGNs. The main difference between the two can be explained by the presence of strong jet structures in the former, in which radio radiation is produced by synchrotron emission. Other apparent differences can be explained by orientation effects and the presence of a dust torus obscuring the central region in objects seen from the side, which explains the difference between type 1 (e.g. Seyfert type 1 galaxies, broad-line radio galaxies) seen from above, and type 2 objects (e.g. Seyfert type 2 galaxies, narrow-line radio galaxies) seen from the side. Even stronger orientation effects occur for radio-loud objects, which are seen as blazars (in which the Doppler-boosted jet emission surpasses the nuclear emission) when observed from directions along the direction of the jet, and as radio galaxies when observed at larger angles. Apart from the presence or absence of the jet structures and the orientation effects, the accretion rate is a major factor

determining the form of accretion and associated variations in spectral properties (Section 1.5).

In recent years, the direct images of the environment near the event horizons of the supermassive black holes in the center of galaxy M87 (Event Horizon Telescope Collaboration et al. 2019) and in the center of our Galaxy (Event Horizon Telescope Collaboration et al. 2022), obtained by the Event Horizon Telescope, confirmed that our understanding of AGNs is correct. The general features of these images, i.e. a deficit of radiation (called the shadow) in the center of the image, surrounded by a slightly asymmetric bright ring of emission, are consistent with theoretical predictions made before these observations. Remarkably, the extents of the shadow regions are consistent with the sizes of the event horizons of these two black holes for their independently estimated masses.

1.4 Accretion disks

Basic principles of accretion appear to be well understood, as summarized in the canonical monography of Frank et al. (2002). The general mechanism of any accretion disk involves the conversion of the gravitational potential into heat by the viscous stresses, while transporting angular momentum outward. However, the disks may have different forms depending on what happens to the heat (whether it is radiated away or not) and how the heat is converted to radiation, which then translates to the observational appearance of the disk.

The classical model of a Keplerian, optically thick disk was developed by Shakura & Sunyaev (1973) and generalized to the Kerr metric by Novikov & Thorne (1973). The model assumes that the heat generated by viscosity is radiated locally in a roughly black-body form (distortions due to processes in the surface layers are typically described by the color correction of this spectrum), so the radiation emitted at each radius is given by the Planck function with $T(r) \propto r^{-3/4}$, with modifications close to the inner edge (assumed to be at the ISCO) related to the assumption that the stress vanishes at the ISCO. The exact $T(r)$ distribution for the disk in the Kerr metric is given in Page & Thorne (1974). The model further assumes that the gas free-falls within the ISCO without any radiation. As noted in Section 1.1, these accretion disks are radiatively efficient. Most of the energy is released in

the inner part of the disk (within the inner few tens of gravitational radii), where the temperature reaches $\sim 10^5$ K for a supermassive black hole and $\sim 10^7$ K for a stellar-mass black hole, leading to radiation primarily in the UV and in the X-rays, respectively. Indeed the dominant emission is observed in these bands in quasars and in the luminous states of X-ray binaries (more specifically, in the soft state, Section 1.5).

However, already in the early 1970s, observations of Cyg X-1 (Tananbaum et al. 1972) showed that the above picture does not apply when the luminosity falls below $\sim 0.01 L_{\rm Edd}$ (and the same was later observed in other X-ray binaries and in AGNs). At these lower luminosities the observed spectra are not those of black bodies, but instead have a form of emission of optically thin gas with electron temperature $T_{\rm e} \sim 10^9$ K. This prompted the search for an alternative form of an accretion flow.

The essential ideas of the model likely describing accretion at low accretion rates were developed by Shapiro et al. (1976), who realized that the disk will be optically thin and hot if it consists of a two-temperature plasma, with electrons much cooler than ions. Several factors contribute to the self-consistency of this model. The ions cannot cool efficiently by radiation (due to large mass), therefore, they retain most of their viscous heat and reach temperatures close to virial. The pressure of these hot ions maintains a large geometrical thickness and this keeps the gas in a low-density state. The low density allows the plasma to retain its two-temperature character, because Coulomb coupling between ions and electrons is inefficient. The low density also makes the plasma optically thin, and then electrons radiate mainly through the synchrotron emission and its Comptonization, producing hard X-ray component dominating the spectrum, such as observed in low-luminosity systems. The model was further extensively developed in a number of works following those of Narayan & Yi (1995), Abramowicz et al. (1995), and Abramowicz et al. (1996). In particular, a crucial role of advection for the stability of these solutions was recognized and they were named as advection dominated accretion flows (ADAF). The ADAFs can exist only at low accretion rates, $\dot{M} \lesssim 10^{-2} \dot{M}_{\rm Edd}$, because at higher values the density becomes large enough for efficient Coulomb cooling of ions, leading to the collapse of the flow. ADAFs are also typically radiatively inefficient, as the released energy is advected rather than radiated away.

Advection plays also a crucial role in another solution, proposed by Abramowicz et al. (1988) and referred to as the slim accretion disk model, which possibly applies to systems observed close to or above the Eddington limit. This solution describes an optically thick, quasi-Keplerian accretion flow with very high accretion rate, in which the radiative transfer from the disk interior is too slow and then the time-scale for radiative cooling is longer than that for advection. The dissipated energy is then carried with the inflow and partially lost under the black hole horizon.

The models briefly described above were studied using the analytic solutions with the phenomenological descriptions of the stresses, typically the Shakura-Sunyaev α prescription, where the shear stresses are assumed to be directly proportional to the pressure. The major later progress in this field involved identification of the origin of the turbulent viscosity as the magnetic rotational instability (Balbus & Hawley 1998). Magnetohydrodynamic simulations driven by this effect increase our understanding of accretion and jet production physics. However, their spectral predictions are still rather immature especially for the range of higher luminosities.

1.5 Spectral states

Black hole systems are observed in different spectral states, which are characterized by different relative contributions of the main spectral components: (1) the soft X-ray thermal component, which is well modeled by a multi-temperature black body from the inner accretion disk, (2) the hard X-ray non-thermal component, usually modeled as a power law and characterized by a photon index Γ (defined by $N(E) \propto E^{-\Gamma}$, where $N(E)$ is the photon spectrum), and (3) the reflection of the latter from the disk. The definition of spectral states follows from X-ray observations and is purely empirical. The definitions are based on energy and power density spectra, the latter representing the fast variability (e.g. Done et al. 2007; Remillard & McClintock 2006), however, the spectral states show also a clear correlation with radio properties (e.g. Fender et al. 2009).

Spectral transitions are observed in all systems which exhibit significant changes of luminosity, but can be most completely studied in transient systems, in which a typical outburst spans several orders of magnitude in luminosity and passes through the main spectral states. Transients exhibit systematic evolution of spectral pa-

rameters when presented e.g. in hardness–intensity diagram (shown in a schematic form e.g. in Fig. 3 of Remillard & McClintock 2006), where the horizontal axis represents the hardness of the source (which is the ratio between its luminosity in the chosen hard and soft X-ray bands, roughly relating to the spectral slope across these energy bands), and the vertical axis is for the total luminosity.

A transient typically spends most of the time in the quiescent state, with a very low luminosity, $L/L_{\rm Edd} \lesssim 10^{-6}$. It may be too faint to be observed, but even if it is detected the quality of data is too poor for detailed spectral studies. An object raising its luminosity during an outburst is first observed in the hard state, characterized by a dominating hard power-law component, with $\Gamma < 2$. The thermal component is either very faint and cool (characterized by temperature $\lesssim 0.1$ keV) or absent. The hard state is associated with the presence of a compact, mildly relativistic, steady radio jet, and clear correlations between the radio and X-ray intensities are observed.

A further increase of luminosity leads to the transition to the soft state, characterized by the dominant thermal component with the characteristic temperature ~ 1 keV. The non-thermal component is very weak and soft, with $\Gamma > 2$ (typically $\Gamma \sim 2.5$). The short-time scale variability is weak and the quasi-periodic oscillations are absent or very weak. In the soft state, the radio jet is not observed.

Transitions between the hard and the soft state can occur in a wide range of $L \simeq (0.01 - 0.5) L_{\rm Edd}$ and the spectral evolution is not uniquely correlated with L. The same black hole can show a different transition luminosity at different times (the hysteresis effect), but in all transients the hard-to-soft transition on the rise of an outburst takes place at larger luminosities than the reverse on the decline. At the hard/soft state transition, intermediate spectral properties are observed and these intermediate states are related with ejections of transient, highly relativistic jets.

Yet another state, very high (sometimes referred to as steep power-law), is observed when the luminosity approaches the Eddington limit. It shares some similarities with the soft state, as both states show a strong thermal component and a steep ($\Gamma > 2$) power-law component. However, the latter is strong in the very high state (whereas it is faint in the soft state). Furthermore, the very high state is associated with high-frequency quasi-periodic oscillations (which are absent in the

soft state).

The black-hole HMXBs are persistent sources and do not exhibit such a variety of states as LMXBs. The most studied source, Cyg X-1, shows only a small range of variability, with L changing by only a factor ~ 3 on long timescales (e.g. Zdziarski et al. 2002) and spends most of the time in the hard state. It occasionally moves to a softer state, typically for a few months, which is usually interpreted as the soft state but often can be also interpreted as the intermediate state because the nonthermal component is relatively strong. However, during the last decade, Cyg X-1 has spent significantly more time in the soft states than during previous observations and displayed two transitions, in 2013 and 2017, to a very soft state with a very weak high-energy tail (Kushwaha et al. 2021). LMC X-1 is always in the soft state. LMC X-3 is usually observed in the soft state and rarely in the hard state.

The spectral states should be related to configurations of an accretion flow, however, there are some significant uncertainties regarding this issue. More specifically, there are large controversies about the nature of the hard state, furthermore, the origin of the hard X-ray source is in general poorly understood in any state. On the other hand, there are no controversies about the thermal component, which is fully consistent with expectations for emission of an optically thick disk and then the soft state is explained by an optically thick accretion disk extending to the ISCO (e.g. Done et al. 2007). Another well understood issue concerns the radiative process producing the hard X-ray component, which in the hard state is observed with a thermal-like cut off indicating that this component is produced by thermal Comptonization in a plasma with an electron temperature ~ 100 keV, whereas in the soft and very high state extends unbroken beyond the sensitivity limit of current γ-ray detectors ($\simeq 500$ keV), indicating that it is produced by a nonthermal population of electrons (e.g. Zdziarski & Gierliński 2004). However, the geometry, location, and the heating process of the X-ray source is poorly understood. The hard X-ray source is then usually referred to as a corona without explicit specification of its properties.

The two types of spectra seen in the main states, hard and soft, could be naturally explained by the existence of two different forms of accretion flow, i.e. a hot, optically thin ADAF which can exist only at low luminosities, and a cool, optically thick disk which can exist at high luminosities. Then, the prevailing view for many years

involved a model with an outer optically-thick accretion disk being truncated at low luminosities, and replaced by a hot, optically-thin inner ADAF. In this model, a decreasing truncation radius leads to softer spectra, and the collapse of the hot flow when the disk reaches the ISCO explains the major hard-soft transition. This scenario is consistent with a number of effects observed in the X-ray spectra, the rapid X-ray variability and the radio jet behaviour (e.g. Done et al. 2007).

There are, however, two caveats to this model. First, our understanding of the mechanisms of truncation is very limited and the theoretical dependence of $R_{\rm in}$ on the luminosity remains unknown, which does not allow for a strict quantitative testing of the model predictions. Secondly, the truncated-disk model has been questioned by numerous results of fitting the relativistic reflection spectra, published over the last several years, where the existence of an untruncated disk has been claimed in the hard state. This last issue is related with the subject of my dissertation and will be discussed in more detail below.

The general spectral trends observed in AGNs are similar to those observed in X-ray binaries. Luminous AGNs, in particular quasars and bright Seyfert galaxies, exhibit a characteristic spectral feature, called the *big blue bump*, representing the thermal emission of optically thick disk around a supermassive black hole, furthermore, such objects often show a strong, broadened iron Kα line, which is commonly attributed to X-ray fluorescence of a cold accretion disk extending close to the black hole. On the other hand, in low-luminosity AGNs both the blue bump and the Kα line are typically weak or absent (e.g. Ho 2008). A particularly interesting class of AGNs are narrow-line Seyfert 1 galaxies (NLSy1s), which are typically found to have a near-Eddington or super-Eddington luminosities. NLSy1s exhibit steeper X-ray spectra than lower luminosity Seyferts and can possibly represent an analogue of the soft or very high state. NLSy1s are discussed in more detail in Section 4.

Finally, another interesting class of *changing-look AGNs*, in which dramatic flux and spectral changes are observed both in the X-rays and in the optical/UV, includes the changing-obscuration objects (showing strong variability of the line-of-sight column density), and the changing-state objects, in which no significant changes in the line-of-sight obscuration are observed. The latter allow to study spectral variability triggered by strong changes in the accretion rate. Interestingly, spectral evolution

similar to the soft-to-hard state transition in black hole binaries have been observed in these AGNs with (variable) $L/L_{\rm Edd} \sim 0.02$ (Noda & Done 2018).

1.6 Relativistic reflection spectroscopy

As described above, it has been empirically established that a source of X-ray radiation (the corona) is usually formed in the vicinity of accreting black holes. The X-ray irradiation of an optically thick disk, which is also often present in the inner parts of black hole systems, produces a reflection component of the spectrum through Compton scattering and absorption followed by re-emission. The original spectral shape of the illuminating radiation is significantly modified in the reflected spectra by involved processes. In the $\sim$ 10 eV to 10 keV energy range, the photoelectric opacity is larger than the electron scattering opacity and in this range the most significant absorption occurs, yielding large departures from the original continuum. Below $\sim$ 10 eV the free-free absorption and bremsstrahlung emission is important, but the related component in the reflected spectrum is often neglected in reflection studies. At energies larger than $\gtrsim$ 10 keV, the electron scattering opacity is larger than the photoelectric opacity because the cross section for photoelectric absorption decreases as $\propto E^{-3}$, and then the Compton scattering is the only important process.

Reflection from the inner parts of the disk is subjected to relativistic distortions, most apparent as the broadening and skewing of the spectral features. The X-ray reflection spectroscopy uses the spectral analysis for such characteristics, and may constrain the geometry of the X-ray corona, the truncation radius of the disk, and the spin of a black hole.

The reflection spectroscopy obviously requires observational data of good quality provided by suitable observational facilities. The ubiquity of reflection features in the spectra of accreting black holes was revealed by `Ginga` (Turner et al. 1989) and first relativistic profiles were discovered with `ASCA` (Tanaka et al. 1994). A further advancement was provided by `Suzaku` (Mitsuda et al. 2007), which operated between 2005 and 2015. Among the current generation of X-ray satellites, the most relevant for spectroscopic studies are `Chandra` (Weisskopf et al. 2002), `XMM-Newton` (Jansen et al. 2001), `NuSTAR` (Harrison et al. 2013), `NICER` (Gendreau et al. 2012), and `Insight-HXTM` (Zhang et al. 2020). The launch of `NuSTAR` in 2012

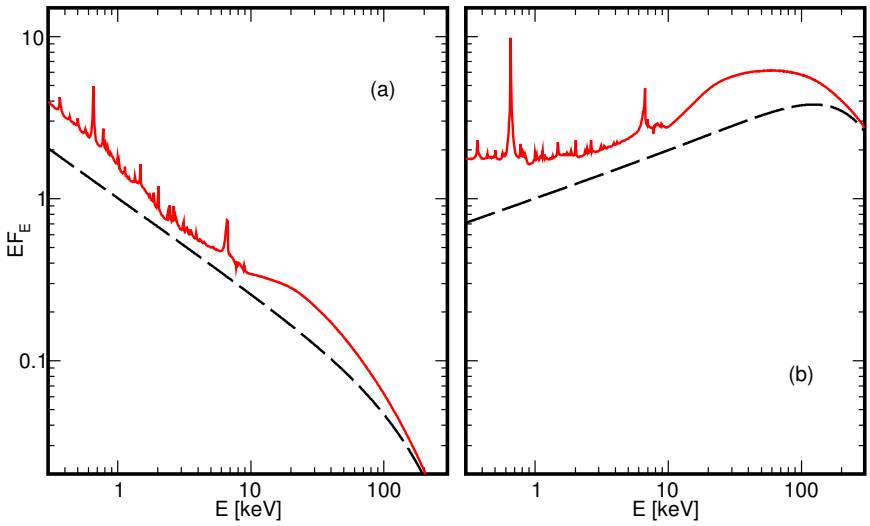

Figure 1: Incident (black dashed) and reflected (red solid) spectra in the rest-frame of the gas, computed with `hreflect` for the incident radiation with the photon index (a) $\Gamma = 1.7$ and (b) $\Gamma = 2.6$, and a high-energy cut-off corresponding to $kT_{\rm e} = 100$ keV. The reflector has the solar iron abundance, $A_{\rm Fe} = 1$, the ionization parameter $\xi = 10^3$, and the electron density $n_{\rm e} = 10^{15}$ cm^{-3}. The reflection strength is $\mathcal{R} = 1$.

has significantly contributed to progress in the field as it yields high signal-to-noise data out to 80 keV, covering the Compton hump at the high energy end of the reflection spectrum. *NuSTAR* has been especially effective when paired with observatories that provide higher spectral resolution at lower energies, typically with either `Suzaku` or `XMM-Newton`, and recently with `NICER`. Further advances are expected from planned instruments with excellent energy resolutions around the Fe K region; unfortunately, the status of `NewAthena`, a rescoped version of `Athena` X-ray observatory, which was expected to provide spectra of unprecedented sensitivity, is currently uncertain.

Relativistic spectroscopy is the main subject of this dissertation, therefore, below I give some technical details of theoretical models applied in it.

1.6.1 Rest-frame reflection

Figures 1 - 3 show the X-ray reflection spectra arising from a static material in flat space-time, irradiated by X-rays with spectrum produced by thermal Comptonization (the power-law with thermal-like cut-off). The most prominent features in these spectra are the Compton hump peaking at $\sim$ 20 keV, the Fe K-edge at 7–10 keV, and fluorescent emission lines. The Compton hump appears in the reflec-

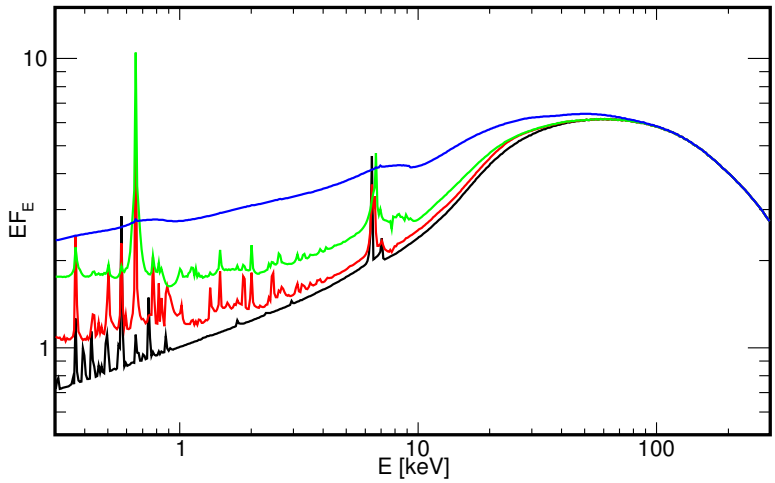

Figure 2: Reflected spectra in the rest-frame of the gas computed with `hreflect` for the incident radiation with the photon index $\Gamma = 1.7$ and $kT_{\rm e} = 100$ keV, assuming that the reflector is characterized by the solar iron abundance, $\mathrm{A_{Fe}} = 1$, the electron density $n_{\rm e} = 10^{15}$ cm^{-3}, and the ionization parameter $\xi = 10$ (black), 300 (red), 1000 (green) and 5000 (blue). The incident spectrum, not shown for clarity, is the same in all cases.

tion spectrum as a result of both photo-electric absorption of low-energy photons and Compton downscattering of high-energy photons. Observationally, the particularly important fluorescent lines are those emitted at energies $\gtrsim 1$ keV, because the Galactic absorption is negligible at these energies (as well as internal absorption, except for Compton-thick Seyfert 2 galaxies). The iron Kα line, emitted at 6.4 keV for neutral Fe atoms and at 6.97 keV for H-like Fe ions, is the dominant line. Its prominence is due to the high probability of fluorescent line emission for iron as well as the high abundance of iron as compared to other ions with spectral lines around 6 keV (like Mg or Ni), whose lines are then much weaker. In the soft X-ray range, particularly strong is the oxygen Kα line at ~ 0.65 keV.

The shape of the reflected spectrum is calculated by solving the coupled equations for the radiative transfer, the energy conservation, and the level population for relevant ions. The most advanced public models representing the solution of this problem are `reflionx` (Ross & Fabian 2005) and `xillver` (García et al. 2013). Both are table models involving large numbers of spectra found by radiative transfer calculations. In particular, `xillver` calculates the ionization balance by implementing the photoionization routines from the `XSTAR` code (Kallman & Bautista 2001). Both models assume Thomson scattering (with a first-order correction), which makes

them inaccurate at high energies[2].

Another popular reflection model, widely applied in X-ray reflection studies for many years, was developed by Magdziarz & Zdziarski (1995). Its version assuming a power-law incident spectrum is called `pexriv`, and the convolution version, allowing for any shape of primary radiation, is called `ireflect`. This model currently provides the most accurate description of the Compton hump, however, its treatment of ionization, following Done et al. (1992), is approximate and fails especially at high values of ξ. Then, Niedźwiecki et al. (2019) developed the hybrid reflection model, `hreflect`, which in the soft X-rays (i.e. below $E_{\rm merge} \simeq$ 10-30 keV; the exact value depends on the ionization parameter defined below) uses the reflection spectrum of `xillver` and in the hard X-rays (above $E_{\rm merge}$) uses the spectrum given by `ireflect`. The procedure of merging the two model spectra is described in detail in Niedźwiecki et al. (2019). This probably gives the most accurate treatment of ionized reflection using currently available models. Figures 1 - 3 show spectra computed using this model and illustrate the dependence of the reflection spectra on the spectral index of the incident spectrum, Γ, the iron abundance, $\rm A_{Fe}$, the electron density of the reflecting medium, $n_{\rm e}$, and the ionization parameter defined as

$$\xi = \frac{4\pi F_X}{n_{\rm e}} \tag{3}$$

where F_X is the irradiating flux in the 13.6 eV - 13.6 keV energy range. The ionization parameter is measured in units of erg cm $\rm s^{-1}$; below I give values of this parameter omitting this unit, which is a common practice in reflection literature.

Figure 1 shows the dependence on Γ for $\xi = 10^3$, which value characterizes most of the fitting results presented in these theses. In general, the reflected radiation obviously follows the intensity distribution of the illuminating radiation, i.e. a harder primary spectrum gives a harder reflected spectrum. For completeness of this description I note also that, as discussed e.g. by García et al. (2013), there occurs also a more intricate effect of the spectral shape of the ionizing radiation on the ionization structure of the gas, which then affects the reflected spectrum. In the limiting case of low ionization (which, through the definition of ξ, implies a weak illuminat-

[2]a new version of `xillver` fixing this problem was announced to be released soon by García et al. (2020), however, it is still not available at the time of completing this dissertation in 2023

ing flux) the heating of the reflecting medium is mostly due to photoionization. In this case, the heating rate decreases with the decrease of Γ, as this gives a lower number of low-energy photons for which the photoelectric opacity is the largest. Therefore, in the low-ionization case, a softer incident spectrum yields a hotter and more ionized gas (at a given ξ). An opposite effect occurs in the high-ionization case, where Compton heating dominates the heating of the gas. In the limiting case of very large ξ the gas temperature approaches the Compton temperature, at which the Compton heating is balanced by the Compton cooling. In this case, a softer incident spectrum yields a colder and less ionized gas (at a given ξ). I note, however, that in all my fittings results I found $\xi \sim 10^3$, at which both the Compton heating/cooling and photoionization heating/recombination cooling contribute significantly to the ionization structure.

Figure 2 illustrates the dependence on the ionization parameter. The low-ξ models are characterized by a strongly absorbed continuum and a large number of narrow emission lines. At higher ξ the continuum is less affected by the photoelectric opacity. In particular, at $\xi \gtrsim 200$ the ions of light elements are completely ionized, whereas the ions of the heavy elements are partially ionized. As a result of the decrease in opacity, the reflected spectra at high ξ are closer in shape to the original illuminating spectrum.

Figure 3 illustrates the dependence on the Fe abundance, A_{Fe}, and on the electron density, n_e. Large values of these two parameters may be relevant for modeling 1H 0707–495 (Section 4). Therefore, for this figure, I assume $\Gamma = 2.6$, characterizing this object spectra. The Fe Kα emission and absorption features are of major importance in the analysis of the reflection spectra and therefore all the reflection models allow to vary the Fe abundance, which is normalized to its solar value. The abundances of all other elements are fixed at their solar values. The abundance of iron obviously affects the strength of its emission and absorption features (see Figure 3a). In addition, the abundance of iron affects the opacity, and hence the photoionization heating rate, and then it also affects the ionization structure for other elements.

Figure 3b shows the impact of higher electron densities on the reflection spectrum. The reflection models traditionally assumed $n_e = 10^{15}$ cm^{-3}. This value

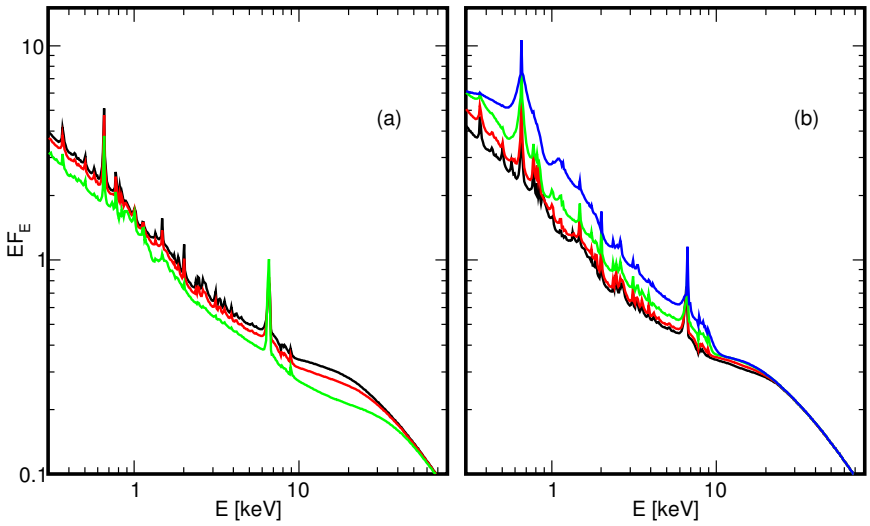

Figure 3: Dependence of the reflected spectra on (a) the iron abundance, and (b) the electron density. In both panels the reflected spectra are computed with `hreflect` for the incident radiation with $\Gamma = 2.6$ and $kT_{\rm e} = 100$ keV and the reflector characterized by $\xi = 10^3$. The incident spectrum (not shown for clarity), normalized at 1 keV, is the same in all cases. (a) $n_{\rm e} = 10^{15}$ cm^{-3} and $\rm A_{Fe} = 1$ (black), 3 (red), 10 (green), 20 (blue). (b) $\rm A_{Fe} = 1$ and $n_{\rm e} = 10^{15}$ cm^{-3} (black), 10^{17} cm^{-3} (red), 10^{18} cm^{-3} (green), 10^{19} cm^{-3} (blue).

may characterize the inner disks in AGNs, however, it is lower than expected for stellar black holes, and actually even for some AGNs it has been argued recently (e.g. García et al. 2016; Jiang et al. 2019) that $n_{\rm e}$ has to be higher than 10^{15} cm^{-3} to fit their X-ray spectra. Therefore, versions of the models allowing to fit this parameter, `xillverD` and `reflionxHD`, have been developed and publically released. At low densities ($n_{\rm e} \ll 10^{15}$ cm^{-3}) the reflected spectra are weakly dependent on $n_{\rm e}$. However, the rates of bremsstrahlung heating and cooling are proportional to $n_{\rm e}^2$ and these processes become important at high densities. At these high densities, the surface temperature of the disk increases with $n_{\rm e}$, as a result of a more efficient free-free absorption (García et al. 2016). Then, the ionization state is dependent on $n_{\rm e}$. The thermal broadening of discrete spectral features, resulting from the higher temperature, can be clearly seen in Figure 3b. Furthermore, the density affects the energy at which a quasi-thermal hump is formed in the reflection spectrum (Zdziarski & De Marco 2020), which is a relevant issue for modeling the soft X-ray spectra in black-hole binaries.

In the above short description, I focused on the shape of the reflected spectrum. Another important issue is the relative strength of reflection to the direct primary

emission. It is measured by the reflection fraction, $\mathcal{R}$, introduced in `pexriv` and then adopted in latter reflection models, defined as the ratio of the flux directed towards the observer to that towards the slab. With this definition $\mathcal{R} = 1$ corresponds to the reflection of an isotropic point source from a semi-infinite slab. Then, $\mathcal{R}$ can be related to the solid angle, Ω, subtended by the reflector at the X-ray source, $\mathcal{R} = \Omega/2\pi$.

Finally, I note shortcomings of the models in the `xillver` and `reflionx` families, available for data analysis (some of which affected my choices of the models in Sections 3 and 4). First, all these models assume that the disk density is constant along the vertical direction of the reflector, whereas in a disk we can expect that the density increases towards the disk center. Furthermore, all `xillver` models use reflection spectra calculated assuming that X-rays illuminate the disk with an angle $\theta = 45°$, and this incidence angle strongly affects the reflection spectrum (and therefore in `hreflect` the reflection strength is adjusted to that of `ireflect`). Yet another shortcoming is related to the description of the primary radiation. The table models necessarily use some specific forms of the incident spectrum. The only table model using the thermal Comptonization spectrum is `xillverCp`, which, however, applies a non-relativistic `nthcpomp` model (Zdziarski et al. 1996) which fails at relativistic temperatures. In `hreflect`, a precise Comptonization model, `compps` (Poutanen & Svensson 1996), is used and mapping of electron temperature is applied to partially compensate the shortcomings of `nthcpomp`. All other table models use the incident spectrum in the form of the power-law with an exponential cut-off. Furthermore, the models including spectra for $n_{\rm e} > 10^{15}$ cm^{-3}, i.e. `xillverD` and `reflionxHD`, include only one value of $E_{\rm cut} = 300$ keV, and finally `refionxHD` is tabulated only for $\Gamma \leq 2.3$ (which did not allow us to use this model in the research reported in Section 4).

1.6.2 Relativistic reflection

Models described in Section 1.6.1 give the reflection spectrum in the rest frame of the disk, but the spectrum seen by the distant observer is additionally affected by the Doppler shift and boosting, the gravitational redshift, and the light bending. In modeling the spectra of radiation reflected from the whole disk surface it is typically

assumed that the disk is described by the Novikov-Thorne model, with the gas in the disk moving on circular orbits in the equatorial plane of a Kerr black hole. The disk is assumed to be infinitesimally thin and its inner edge is sometimes fixed at the ISCO, $R_{\rm in} = R_{\rm ISCO}$, but the disk may be also truncated at a larger radius, $R_{\rm in} > R_{\rm ISCO}$, and in some version reflection from the material free falling within the ISCO is taken into account, i.e. $R_{\rm in} < R_{\rm ISCO}$. The relative contribution of reflection from various parts of the disk depends on the illumination pattern of the disk and then on the geometry of the primary X-ray source. This geometry is, however, highly uncertain, and two simplifying approximations are commonly applied. First, irradiation of the disk surface by a point-like source on the symmetry axis is assumed, in the setup called the lamppost geometry (the left panel in Figure 4). Secondly, even more often a phenomenological radial emissivity is assumed (with an azimuthal symmetry), without any explicit assumption about the geometry and location of the primary X-ray source. The latter (phenomenological) models usually use a power-law radial emissivity, $\varepsilon(R) \propto R^{-q}$, where q is the emissivity index, but often also a broken power-law, with different emissivity indices within and beyond the breaking radius, $R_{\rm br}$ (and sometimes even a double-broken power law).

The public relativistic reflection models include: `relxill` (Dauser et al. 2013), `kyn` (Dovčiak et al. 2004), `reflkerr` (Niedźwiecki et al. 2019), and `reltrans` (Ingram et al. 2019). The first three are available in the phenomenological as well as the lamppost versions, while `reltrans` works only with the lamppost set-up. Each of these families also has its own specific features addressing various aspects of spectral modeling. Importantly, while using different code architectures, the relativistic parts of these four model families are in good agreement (the comparison of the line shape among `relline`, `kyn`, and `reflkerr` is presented in Niedźwiecki et al. 2019).

Reflection models applied in data analysis commonly use the formalism of the transfer function, which describes the travel of photons in the Kerr metric and allows to separate the description of radiative processes in the rest-frame of the gas and the general relativistic transfer effects. The flux seen by a distant observer from the disk is computed as

$$N_{\rm disk}(E_{\rm o}, i) = \frac{1}{D^2} \int \mathcal{T}_{\rm do}(a, r, \theta_{\rm d}, i, g_{\rm do})\, N_{\rm em}(E_{\rm o}/g_{\rm do}, r, \theta_{\rm d}) 2\pi r\, {\rm d}r {\rm d}\mu_{\rm d} {\rm d}g_{\rm do}, \qquad (4)$$

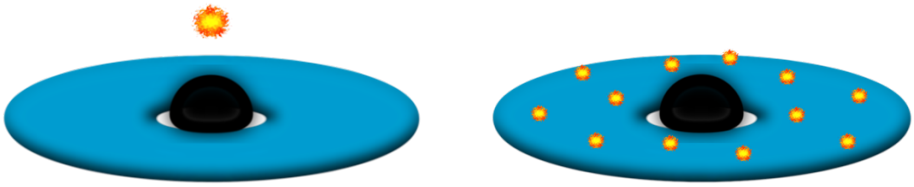

Figure 4: Corona geometries. Left panel shows the lamp-post geometry with a compact X-ray source on the symmetry axis. Right panel shows the geometry described by the `reflkerr` model (see text).

where $g_{\rm do} = E_{\rm o}/E_{\rm d}$ is the redshift factor, $E_{\rm o}$ and $E_{\rm e}$ are, respectively, the photon energy measured by the observer and the photon energy at the emission point in the rest-frame of the disk, $\mu_{\rm d} = \cos\theta_{\rm d}$, $\theta_{\rm d}$ is the emission angle in the disk frame, i is the viewing angle (i.e., the angle between the normal to the disk and the line of sight of the observer), $N_{\rm em}$ is the photon number intensity of the reflected radiation in the disk frame, D is the distance of the observer from the source, and $r = R/R_{\rm g}$ (general relativistic effects affecting the observed spectrum do not depend on M, unless temporal variability is considered, therefore, it is convenient to use the radial coordinate measured in the unit of gravitational radius). The radial integration is performed between $r_{\rm in}$ and $r_{\rm out} \geq 10^3$. The above convolution defines the disk-to-observer transfer function, $\mathcal{T}_{\rm do}$, whose definition adopted here follows Laor et al. (1990) and Laor (1991).

In the lamp-post model, the flux of the primary radiation seen by a distant observer is

$$N_{\rm direct}(E_{\rm o}, i) = \frac{1}{D^2}\mathcal{T}_{\rm so}(a, h, i)\, N_{\rm s}(E_{\rm o}/g_{\rm so}), \tag{5}$$

and the photon flux irradiating the disk at distance r is

$$N_{\rm d}(E_{\rm d}, r) = \mathcal{T}_{\rm sd}(a, r, h)\, N_{\rm s}(E_{\rm d}/g_{\rm sd}), \tag{6}$$

where $\mathcal{T}_{\rm so}$ and $\mathcal{T}_{\rm sd}$ are the corona-to-observer and corona-to-disk transfer functions, respectively, $g_{\rm so} = E_{\rm o}/E_{\rm s}$ and $g_{\rm sd} = E_{\rm d}/E_{\rm s}$ are the photon energy-shift factors, the subscripts 's', 'd' and 'o' denote quantities measured in the local source frame, in the local frame co-moving with the disk, and those observed by a distant observer, respectively, and $N_{\rm s}(E_{\rm s})$ is the photon number intensity produced at the corona. The transfer functions $\mathcal{T}_{\rm sd}$, $\mathcal{T}_{\rm do}$, and $\mathcal{T}_{\rm so}$, and the energy-shift factors $g_{\rm sd}$, $g_{\rm do}$ and $g_{\rm so}$, treat

the special and general relativistic effects affecting both the irradiating and observed fluxes. The transfer functions are constructed by calculating and tabulating a large number of photon paths.

The irradiating flux given by equation (6) allows to determine $N_{\rm em}(E_{\rm d})$ for equation (4) by applying one of the models described in Section 1.6.1. In the lamp-post model, all the irradiating and observed fluxes are strictly determined by the model geometry and then the relative normalization of the reflected and the directly observed components is also strictly determined. However, it has become a common practice in this research area to freely scale these components, i.e. to compute the total observed flux as

$$N_{\rm total} = N_{\rm direct} + \mathcal{R} N_{\rm disk}, \tag{7}$$

where $\mathcal{R}$ is the scaling parameter introduced in analogy to the reflection fraction defined in Section 1.6.1. I note, however, that for a given height of the lamp and given $r_{\rm in}$ of the disk, the solid angle subtended by the disk is strictly determined and hence the unphysical values of $\mathcal{R} \neq 1$ lack the geometrical justification. This issue is discussed in detail in Section 3.

In the lamp-post geometry, the spectrum irradiating the disk is radius-dependent, because $g_{\rm sd}$ is a function of the radius. Most notably, the spectrum seen in the disk frame, $N_{\rm s}(E_{\rm s}/g_{\rm sd})$, has different cut-off energies in different parts of the disk. In contrast, the phenomenological models typically assume that the irradiating spectrum and hence also the reflected spectrum, as seen in the disk frame, are radius-independent. The dependence on the radius in this (phenomenological) model is described by the radial emissivity

$$\epsilon(r) = \begin{cases} (r/r_{\rm br})^{-q_1}, & r \leq r_{\rm br}; \\ (r/r_{\rm br})^{-q_2}, & r \geq r_{\rm br}. \end{cases} \tag{8}$$

The approach to the direct component observed from the corona is different in different reflection models. In `reflkerr` it is assumed that this radiation is subject to the same transfer effects as the reflected radiation. Then, the total observed flux is given by equation (4), with the locally emitted spectrum including both the

primary and reflected components, i.e.

$$N_{\rm em}(E_{\rm d},\theta_{\rm d},r)=\varepsilon(r)\left[N_{\rm s}(E_{\rm d},\theta_{\rm d})+\mathcal{R}N_{\rm ref}(E_{\rm d},\theta_{\rm d})\right], \tag{9}$$

where, as above, $N_{\rm s}$ denotes the coronal spectrum and $N_{\rm ref}$ the corresponding reflection. This directly implements the corona covering the accretion disk at a low scale height, and co-rotating with it, in the so-called sandwich geometry. This approach to the model with empirical emissivities has two advantages. First, it represents a precise description of the (sandwich) disk-corona geometry, which is often considered in the literature. Secondly, it gives the physical meaning to the scaling parameter, $\mathcal{R}$, of reflection. $\mathcal{R}<1$ may be explained here as the attenuation of the reflected component due to scattering in the corona. $\mathcal{R}\gg 1$ implies that the model is probably not self-consistent. I also note that in all applications of `reflkerr` presented in this dissertation, I assume an isotropic emission of the corona, which corresponds to the physical model presented in the right panel of Figure 4, i.e. the corona actually represents a large number of isotropically emitting active regions. Alternatively, the corona may be a uniform, plane-parallel plasma covering the disk surface, however, in this case, the coronal emission is nonisotropic and the model is more complex.

Figure 5 illustrates the dependence of relativistic reflection on the inclination angle, the spin and the radial emissivity. The inclination angle determines the position of the peak of the iron line profile, often referred to as the blue peak, with larger inclinations corresponding to higher energies of the peak. Then, if the analyzed data have good quality and exhibit a pronounced peak of the line followed by an edge, the inclination is typically well defined. Under the usual assumption (but not necessarily correct) that the disk extends to the ISCO, the spin affects the spectrum as seen in Figure 5b. This spin effect results from the strong dependence of the extension of the red tail of relativistically broadened lines on the emitting radii. The radial emissivity also has a strong effect on the spectrum, see Figure 5c. I note that for extremely steep radial emissivities, with $q\gtrsim 5$ (claimed in some fitting results), the spectral features are severely smeared and the spectrum loses the characteristic shape, which allows to robustly identify the presence of reflection component, as shown by the blue line (for $q=5$) in Figure 5c. In this regime, the results of data analysis are extremely model-dependent, in particular, disentan-

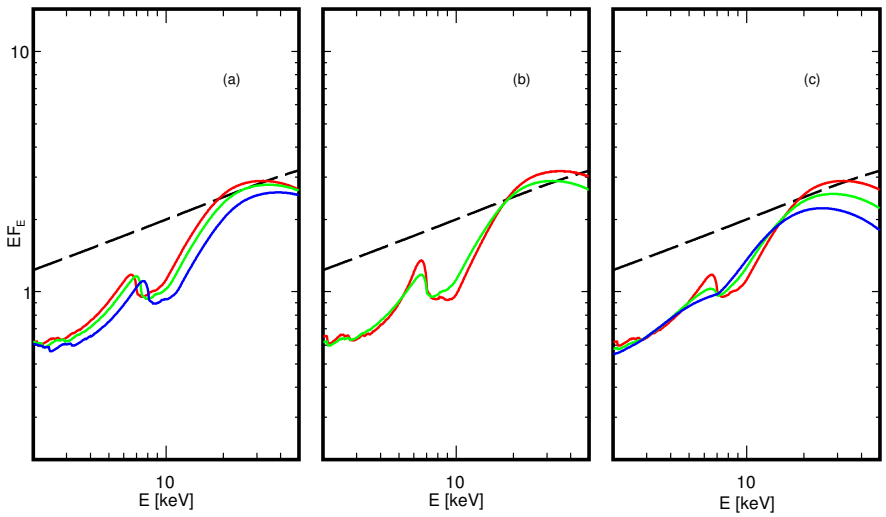

Figure 5: Effects of (a) inclination angle, (b) black-hole spin, and (c) radial emissivity, on the reflection spectrum computed with `reflkerr`. All models assume $\Gamma = 1.7$, $kT_{\rm e} = 100$ keV, $\mathrm{A_{Fe}} = 1$, $n_{\rm e} = 10^{15}$ cm^{-3}, $\xi = 1000$, $R_{\rm in} = R_{\rm ISCO}$, and $\mathcal{R} = 1$. The primary spectrum is the same in all cases and is shown by the dashed black line. (a) $q = 3$, $a = 0.998$ and $i = 30°$ (red), 45° (green), and 60° (blue). (b) $q = 3$, $i = 30°$ and $a = 0.998$ (green) and $a = 0$ (red). (c) $i = 30°$, $a = 0.998$ and $q = 3$ (red), 4 (green) and 5 (blue).

gling the reflection from the accretion disk and the absorption features (which are theoretically expected and typically indeed present) is problematic.

1.7 Spin measurements

The black hole spin is a key astrophysical parameter, which provides important information about the birth and the evolution of these objects, determines the radiative efficiency of their accretion systems, and may have a critical role in the production of powerful jet structures (e.g. Tchekhovskoy et al. 2010).

In the case of stellar-mass black holes in X-ray binaries, the value of the black-hole spin parameter is normally determined by the formation mechanism, because the amount of mass that can be transferred from the companion star to the black hole is modest and cannot appreciably change the black hole mass and spin angular momentum (see, e.g., King & Kolb 1999). On the contrary, for supermassive black holes in AGN, the value of their spin parameter is determined by the mass transferred from the host environment to the compact object and spin measurements can test different scenarios of galaxy evolution and merger (e.g., Barausse 2012; Sesana et al. 2014).

Analysis of the spectral data measured in black-hole systems allows to constrain the black-hole spin using two methods; the recent review of basic principles and results is presented by Reynolds (2021). One method uses the shape of the disk continuum in the thermal-dominated spectral states and assumes that the disk extends to the ISCO, which has a rather strong observational support in these states (Section 1.5). The spin can then be measured from fitting the disk spectrum if the distance to the source and the black-hole mass are independently measured. This method can be applied in black-hole binaries, where the disk emission peaks in the X-ray range. On the other hand, in AGNs the disk emission is expected to peak in the far-UV, which is unobservable due to interstellar absorption, and this method typically cannot be applied. The second method uses fits of reflection spectra and relies on the dependence of the radius of ISCO on the black-hole spin. Again an assumption is made that the accretion disk extends to the ISCO and then the spin is estimated as described in Section 1.6.2.

The disk continuum fitting method was first discussed by Zhang et al. (1997), refined in the GR framework by (Gierliński et al. 2001), and then further advanced and applied to several black-hole binaries in the soft state as reviewed e.g. by McClintock et al. (2014). The estimated spin values are typically high, in particular in HMXBs, which is in tension with the low black-hole spins inferred from analyses of merger events detected in gravitational waves (Section 1.8) as well as with expectations of the formation and evolution of stellar-mass black holes (e.g. Belczynski et al. 2021). This prompted Belczynski et al. (2021) and (Zdziarski et al. 2023a) to reconsider the foundations of the disk continuum fitting by taking into account an optically thick Comptonizing layer on the surface of the standard disk. They conclude that determinations of the spin using the continuum fitting method is highly sensitive to the assumptions about the disk structure, as presence of a warm Comptonizing skin can reduce the derived spin to a very small value.

As noted above, in AGNs the spin cannot be estimated from the peak temperature and luminosity of the disk continuum in AGNs. However, Davis & Laor (2011) used the disk model to measure $\dot{M}$ from the optical/UV flux (emitted at intermediate radii) and integrating the observed spectral energy distribution to estimate L, which allowed them to infer typically large spin values in their sample of AGN, with

indications of the increase of the spin with M.

The reflection spectroscopy (also called the iron line method) started with the discovery of a relativistic iron line profile in the Seyfert galaxy MCG–6-30-15 (Tanaka et al. 1995) and since then has been applied to a number of black-hole binaries and AGNs; the results collected e.g. by Reynolds (2021) and Bambi et al. (2021) indicate that almost all these objects contain a rapidly, in many cases maximally, rotating black holes. Many of these results, however, were made in hard spectral states in which the location of the disk inner radius is highly controversial and then these spin assessments are doubtful.

There have been significant recent developments in relativistic reflection spectroscopy, however, this method still involves some technical simplifications and then it is subject to major uncertainties, as reviewed e.g. by Bambi et al. (2021). I here note issues most relevant to the subject of my research. Assessments of an untruncated disk extending to the ISCO of a rapidly rotating black hole are usually accompanied by assessments of an extremely steep irradiation profile in the innermost few gravitational radii, with $q \gtrsim 4$ (and in many cases $q \simeq 10$), when modeled with empirical radial profiles. Such a steep irradiation can only be explained by an extremely compact corona located extremely close to the event horizon. Indeed, when described in the lamp-post geometry, often the extreme location of the lamp-post, almost on the horizon, is found. This has severe implications on the overall physical scenario (pointed out in Niedźwiecki et al. 2016), as a majority of photons emitted from such a corona are trapped under the event horizon and only very few of them are able to go to the observer, which implies a very small radiative efficiency. Also, the source is out of equilibrium between production of electron-positron pairs and their annihilation. Furthermore, the nature of the transition between the hard and soft states becomes difficult to understand if the disk extends to the ISCO in both of them. Another issue concerns a strong model dependence of the fitting results, as in many cases the same observations as those used by the authors claiming the disk extending to the ISCO (e.g. García et al. 2015b; for GX 339-4) have been fitted by others, who found the disk to be truncated (e.g. Dziełak et al. 2019; for the same data of GX 339-4). Similar examples for Cyg X-1 are discussed in Section 3.

1.8 Gravitational waves from binary black holes

Previous sections focused on electromagnetic observations, which for several decades had been the only domain of studying compact objects. In the last decade, the black-hole astrophysics has received a new window with the emergence of gravitational-wave astronomy. The frequency of the gravitational wave signal depends on the size of the source. The ground-based laser interferometers work in the frequency range from 10 Hz to 10 kHz, which makes them suitable to detect gravitational waves generated by stellar black holes orbiting in compact binary systems (i.e. consisting of two black holes or a black hole and a neutron star). The gravitational waves from binary systems of supermassive black holes have frequencies below 100 mHz and can be detected by future space-based laser interferometers. Very recently the pulsar timing array groups reported the evidence for nanohertz gravitational waves (Agazie et al. 2023) which may be generated by orbiting pairs of supermassive black holes.

The gravitational wave signal measurable with the current generation of gravitational wave detectors, i.e. Laser Interferometer Gravitational Wave Observatory (LIGO), Virgo and Kamioka Gravitational Wave Detector (KAGRA), can be produced by a stellar binary system only during the merger of its components. The first signal from the merging binary black-hole (BBH) system was detected by LIGO on 14th September 2015 (Abbott et al. 2016). This first source, GW150914, involved the merger of black holes with masses 36 $M_\odot$ and 31 $M_\odot$, which formed a final 63 $M_\odot$ black hole. Since then LIGO has completed three observing runs, during the last two was joined by Advanced Virgo and during the last one by KAGRA.

The merger of a BBH has three stages: (1) inspiral, when the two black holes are still separated and orbit their common center of mass, (2) coalescence, which is a violent process in which a few percent of the rest-mass energy of the system is radiated in a time of the order of milliseconds, producing a huge gravitational-wave luminosity of $\sim 10^{56}$ erg s^{-1}, and (3) ringdown, when the product of coalescence relaxes toward the Kerr metric. The waveform at the inspiral stage is affected by both the spins and masses of the merging objects and the analysis of the observed signal allows to put constraints on these parameters.

LIGO/Virgo/KAGRA have detected gravitational waves from 70 double black

hole mergers (Abbott et al. 2023). The observed merging black holes have masses in the range $\sim (3-100)\ M_\odot$. The most massive event, GW190521, had two merging black holes with the masses of $\sim 95\ M_\odot$ and $\sim 69\ M_\odot$. Furthermore, most of the merger events involve slowly spinning black holes, with the average spin parameter $a \simeq 0.2$. The strongest constraint on the individual spin value, $a < 0.07$, was found for the $23\ M_\odot$ black hole in GW190814. Then, the black holes measured via merger events tend to be more massive and slower spinning than black holes observed in X-ray binaries. Parameters characterising the latter are collected e.g. by Fishbach & Kalogera (2022). All currently known black holes in X-ray binaries have masses $M \lesssim 20\ M_\odot$ and the spins in the majority of them were found to be high, with $a \gtrsim 0.9$. HMXBs are likely the progenitors of the black hole-black hole mergers, as only in these systems the companion stars are massive enough to form a black hole. For the three known HMXBs with a sufficiently massive companions, LMC X-1, Cyg X-1, and M33 X-7, the estimated spin values are $a \gtrsim 0.9$. These discrepancies have lead Fishbach & Kalogera (2022) to propose that the two groups of black-hole binaries belong to different populations (with different formation scenarios).

However, Belczynski et al. (2021) found that the difference in masses is likely explained as the known HMXBs are in galaxies with relatively high metallicity, so their progenitor stars are subject to strong mass loss from winds which leads to a relatively low-mass black hole at the collapse. In contrast, gravitational waves allow for detection from low metallicity galaxies that produce more massive black holes.

The issue of the discrepancy between black hole spins in BBHs and HMXBs is examined by Belczynski et al. (2021) and Zdziarski et al. (2023a), as discussed in Section 1.7.

1.9 Summary and aims of PhD theses

Our understanding of accreting black holes has significantly progressed over the last 50 years. The large observational material has been substantially systematized by defining various classes of objects and various spectral states. On the theoretical side, it was recognized that various forms of accretion flows can exist, and the relation of the optically thick accretion to the thermally-dominated states observed in luminous systems was robustly established. On the other hand, the interpretation

of the states dominated by hard X-ray radiation remains a highly controversial issue, mostly due to mutually contradictory interpretations of X-ray reflection features. Some studies assess that the observed reflection spectra are consistent with the truncation of an optically thick disk and the formation of an optically thin flow in the inner part, which picture has strong support in the theory of ADAFs. Other groups, however, find that these features are dominated by reflection from the inner parts of an untruncated disk. This controversy is also related to assessments of the black hole spin. Reports of high values of the spin are made only by the latter groups, as the lack of truncation is essential for these estimations. The discrepancy between these reported values (of high a) and the gravitational-wave measurements, which are not affected by the complexity of accretion physics and assumptions made in the analysis, reiterates the question about the validity of the former results (i.e. those based on the reflection spectra).

Reflection spectroscopy currently represents the most advanced tool for studying the inner region of accretion flows, however, the applied reflection models involve a number of simplifications, and therefore care is needed in the interpretations of such studies. In this dissertation I take into account effects of a more physical description of the X-ray source than applied in previous works, specifically, I consider the effects of: (1) finite extent, (2) rotation, and (3) vertical motion of the source. Effect (3) was considered in Klepczarek et al. (2023), which is a part of this dissertation. Effects (1) and (2) were considered by Szanecki et al. (2020), which is not a part of this dissertation (I contributed to that work by making the data analysis). However, my results strongly rely on that work, therefore, in Section 2 I include a discussion of these effects (1 and 2), extending our previous works on this subject. In particular, I present a new analysis of the size of the corona for which it can be accurately approximated by a point-like source, as typically assumed in the lamp-post models.

An important application of the model with vertically outflowing X-ray source concerns the hard states of black-hole binaries, in which the observed reflection component is often weaker by a factor of several (e.g. by factor ~ 5 for Cyg X-1; Section 3) than expected for an isotropic source above an untruncated disc, e.g. Gierlinski et al. (1997), Di Salvo et al. (2001), Parker et al. (2015), Basak et al. (2017). This can be explained if reflection arises from either a truncated disk irradiated by a hot

inner flow (Esin et al. 1998), or a disk irradiated by a source moving away from it with mildly relativistic velocity (Beloborodov 1999). In Section 3 I present results of the application of the reflection model with an outflowing corona to the hard state observation of Cyg X-1 by `Suzaku` and `NuSTAR`. The analysis is aimed at constraining parameters of the X-ray source and the disk as well as the black-hole spin parameter, and assessment if the current quality of X-ray spectral data allows to discriminate between these two solutions (truncated disk and outflow). This analysis was presented in Klepczarek et al. (2023), which had a form of a letter and therefore included an abridged discussion of these results. Here I present a slightly extended discussion.

The primary motivation for considering the model with an extended corona concerned the idea put forward by Wilkins & Fabian (2012) and Wilkins et al. (2014), who proposed that the corona size can be estimated from parameters of empirical models fitted to the data. This proposed method, however, leads to misleading results, as thoroughly discussed in Szanecki et al. (2020). Szanecki et al. (2020) also presented the spectral model for 1H 0707–495, which shows one of the most extreme reflection features observed in accreting systems. However, the analysis presented in that work was limited to the 1.1–10 keV range. In Section 4, I present results of the work in which application of the model is extended to the full energy range of `XMM`, i.e. 0.3–10 keV. The analysis is again aimed at constraining parameters of the source. These results will be presented in Klepczarek, Niedźwiecki, Szanecki & Lubiński, in preparation.

The text in the following sections is written in the plural form, because I report results of research carried out jointly with my supervisor and co-supervisor. My contribution to the research was to make the reduction of data from the `Suzaku` and `NuSTAR` observations of Cyg X-1, and to carry out all steps of the analysis of Cyg X-1 and 1H 0707–495, in which I applied models developed by my collaborators. I also used these models to make new tests (with synthetic spectra) presented in Section 2, I used the transfer functions of these models to illustrate the discussed effects, and I made calculations for the outflow in the non-GR case.

2 Relativistic reflection: extended corona, rotation and outflow

As discussed in Section 1.6, relativistic reflection models are typically applied with either of the two approximations, i.e. the lamp-post geometry or phenomenological descriptions using power-law radial emissivities. The lamp-post geometry, first considered by Martocchia & Matt (1996) for estimating the enhanced irradiation of the inner disk by gravitational focusing in the mathematically simplest case, has been then used to compute the spectrum of the reflected radiation in a number of works (e.g. Dauser et al. 2013; Miniutti & Fabian 2004; Niedźwiecki & Życki 2008). An important motivation for the lamp-post geometry comes from attempts to constrain the black-hole spins using relativistic reflection spectroscopy (e.g. Reynolds 2021). These estimations typically require very centrally concentrated profiles, which can only be explained if the X-ray source is located very close to the black-hole horizon. While severe problems were pointed out for the lamp-post geometry, especially for extreme (close to event horizon) locations of the X-ray source (Niedźwiecki et al. 2016), it has an important advantage of predicting the spectral distortions by relativistic effects of the Kerr metric within their physical limits. This is in contrast to phenomenological models assuming an arbitrary radial distribution of reflection, in which nonphysically steep emissivities are often estimated, leading to nonphysical conclusions, as discussed by Szanecki et al. (2020) and briefly in Section 2.2 below.

While applications of lamp-post models give an estimation of the location of a corona required to explain the irradiation profile, they give no direct information about its allowable size. Another shortcoming of these applications concerns the free scaling of the reflection component, which procedure is tentatively attributed by the authors of such analyses to the corona kinematics. However, other relevant effects are then not taken into account, making this approach non-physical. In our group two models were developed, `reflkerr_elp` (for 'extended lamp-post') and `reflkerrV`, which allow us to study such effects in a self-consistent manner. These models closely follow the standard lamp-post model, except for taking into account the spatial extent and motion of an X-ray source, instead of treating it as point-like and static. In this section, the spectra predicted by these models are used to discuss

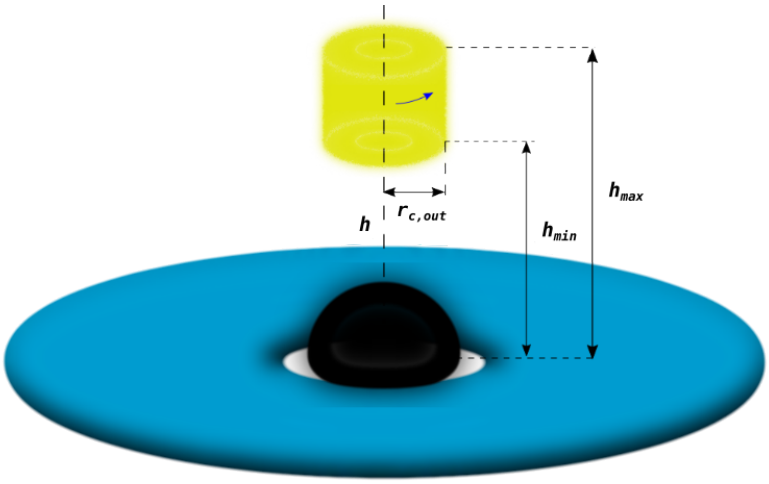

Figure 6: Geometrical set-up assumed in `reflkerr_elp`. The `reflkerrV` model assumes the same geometry, but with a vertical motion within the corona instead of its rotation.

the involved effects. In addition, the transfer functions of these models are used to illustrate the effects in the radial emission profiles.

2.1 Notation and construction of the models

We consider a Keplerian disk in the equatorial plane of the Kerr metric, irradiated by a cylindrical corona with radius $r_{\rm c,out}$, located symmetrically around the black-hole rotation axis between a lower height $h_{\rm min}$ and upper height $h_{\rm max}$, see Figure 6. This geometrical setup is the same for all models described below. The inclination angle of a distant observer is denoted by i. All length scales r, h are in units of the gravitational radius, $R_{\rm g} = GM/c^2$. We assume that the corona is uniform, i.e. its rest-frame emissivity is constant in Boyer-Lindquist coordinates. The inner radius of the disk is denoted by $r_{\rm in}$.

The above geometry is implemented in the `reflkerr_elp` model, developed in Szanecki et al. (2020), and in the `reflkerrV` model, developed in Klepczarek et al. (2023). The corona can be either static, or rotate (in `reflkerr_elp`), or be in the vertical motion (in `reflkerrV`). The construction of `reflkerr_elp` and `reflkerrV` closely follows that of the lamp-post models, as described in Section 1.6.2. In particular, the convolution of the general-relativistic effects with the rest-frame radiation spectra makes use of the transfer functions, which are constructed by tabulating a large number of photon trajectories. The source-to-disk and source-to-observer

transfer functions are tabulated in a grid including 51 bins in both $r_{\rm c} = r\sin\theta$ and $h = r\cos\theta$. We use 50 bins logarithmically spaced between $r_{\rm c} = 0.1$ and $r_{\rm c} = 50$, and the additional bin for $r_{\rm c} = [0, 0.1]$, and similarly 50 bins logarithmically spaced between $h = 0.1$ and 50, and the additional bin for $h = [0, 0.1]$. Then, in our parametrization of the model, both the $r_{\rm c,out}$ and $h_{\rm max}$ parameters can be fitted in the range of $[0.1, 50]$. To compute these transfer functions, we generated photon trajectories sampling the region at $0 \leq h \leq 50$ and $0 \leq r_{\rm c} \leq 50$ with uniform probability density; at each point, the initial direction in the source rest-frame was generated with an isotropic probability distribution. The photon trajectories were computed using the code developed by Niedźwiecki & Życki (2008). For the disk-to-observer transfer, we use the original transfer functions of our `reflkerr` model.

The models allow to use a free normalization of the reflection component by $\mathcal{R}$, where $\mathcal{R} = 1$ corresponds to the actual normalization for a given geometry. For the discussion below we also define the reflection strength, $\mathcal{R}_{\rm obs}$, defined here as the ratio of the observed reflected and direct fluxes in the 20-30 keV range.

2.2 Size

Figures 7 and 8 illustrate changes in the irradiation profiles and the corresponding reflection spectra resulting from the change of the spatial extent of the static X-ray source in the vicinity of the black hole horizon. For a relatively large corona with $h_{\rm max} = r_{\rm c,out} = 50$ and $h_{\rm min} = 0$, shown by the blue line, reflection from the innermost disk is strongly reduced. As the corona shrinks to $h_{\rm max} = r_{\rm c,out} = 15$ (green), 5 (red) and 1.5 (black) we see a clear increase in relativistic broadening as well as in $\mathcal{R}_{\rm obs}$. The latter results from the light bending, which is well known to increase the fraction of photons hitting the disk (Martocchia & Matt 1996). Note, however, that an extremely steep radial profile, such as required to explain an apparently extreme broadening of reflection features claimed in some fitting results, is obtained only for a very compact corona located almost on the event horizon, with $h_{\rm max} \lesssim 2$ and $r_{\rm c,out} \lesssim 2$. For larger corona sizes, the produced spectra do not exhibit a significant contribution of redshifted reflection and can be actually well approximated by a truncated disk model. To verify this, we simulated synthetic spectra for

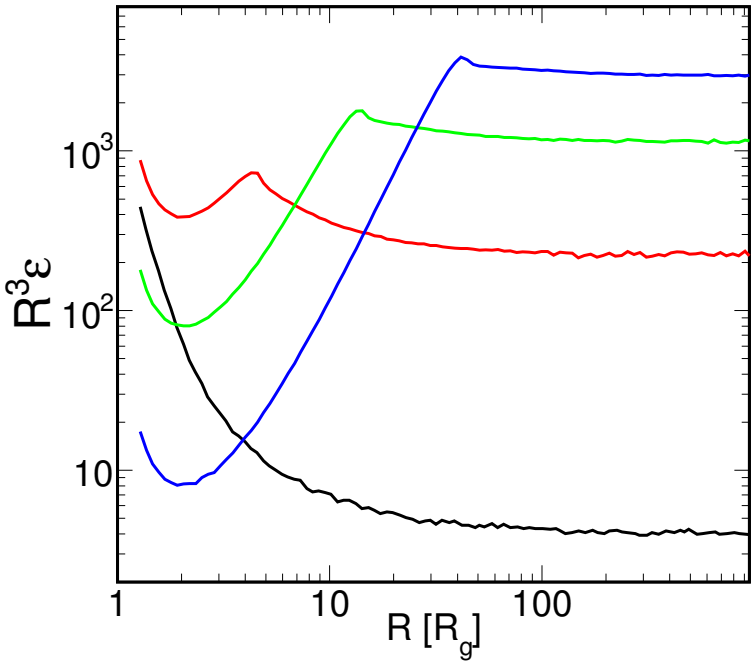

Figure 7: Radial irradiation/emission profiles for a static corona with $h_{\rm min} = 0$ and $r_{\rm c,out} = h_{\rm max} = 1.5$ (black), 5 (red), 15 (green), 50 (blue). All models assume $a = 0.998$ and $\Gamma = 2$ (the value of the photon index slightly affects the shape of steep part at $r \lesssim 2$, which is related to the blueshift of incident photons). The profiles are computed using the transfer function of `reflkerr_elp`. The normalization is arbitrary but in all cases it corresponds to the same total intrinsic luminosity of the corona. The emissivity ε is multiplied by R^3 to better illustrate deviations from the classical profile $\varepsilon \propto R^{-3}$.

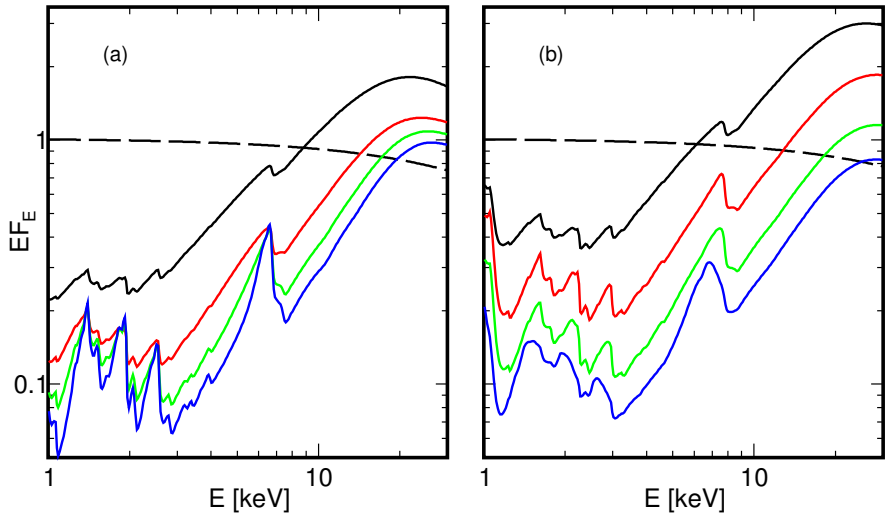

Figure 8: Reflected spectra for (a) $i = 30°$ and (b) $i = 60°$; the assumptions and color coding is the same as in Figure 7, i.e. the corona is static with $h_{\rm min} = 0$ and $r_{\rm c,out} = h_{\rm max} = 1.5$ (black), 5 (red), 15 (green), 50 (blue). In all cases $a = 0.998$, $r_{\rm in} = r_{\rm ISCO}$, $\Gamma = 2$, $\xi = 100$, $A_{\rm Fe} = 1$, and $n_{\rm e} = 10^{15}$ cm^{-3}. The primary spectrum is shown by the dashed line and all spectra correspond to the physical normalization, i.e. $\mathcal{R} = 1$.

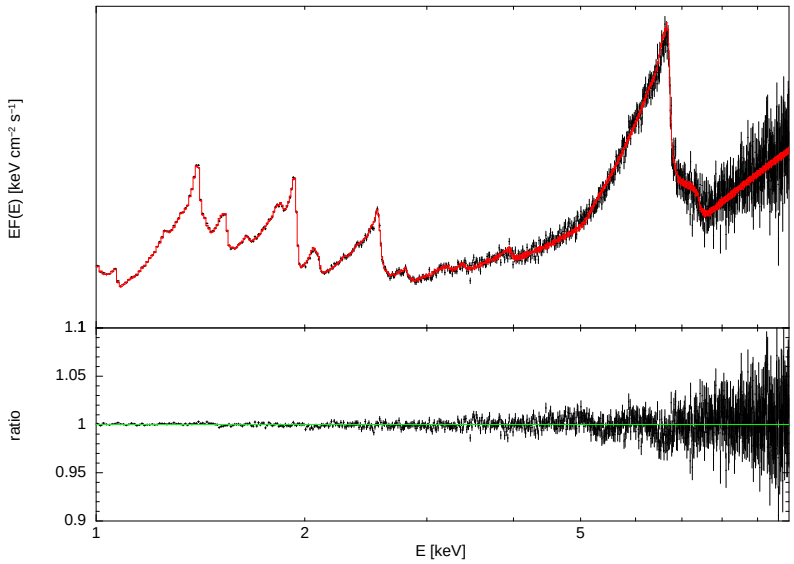

Figure 9: The black points show the synthetic spectrum of `NICER` observation for the model spectrum computed with `reflkerr_elp` with $h_{\rm max} = r_{\rm c,out} = 30$ and $h_{\rm min} = 0$; the red line shows the spectrum fitted with `reflkerr` for $q \simeq 3$ and $r_{\rm in} \simeq 15$ (see text). The lower panel shows the fit residuals given as the data-to-model ratio.

`NICER` observations using the `fakeit` command in `xspec` and adding Poisson noise to mimic statistical fluctuations expected in real observations, assuming the X-ray flux of 3×10^{-9} erg s^{-1} cm^{-2} in the 2–10 keV range (characteristic for bright X-ray binaries) and the exposure time of 100 ks. We generated spectra for parameters given in the caption of Figure 8 ($a = 0.998$, $r_{\rm in} = r_{\rm ISCO}$, $\Gamma = 2$, $\xi = 100$, $A_{\rm Fe} = 1$, $i = 30^\circ$) and several values of $h_{\rm max} = r_{\rm c,out}$. We then analyzed these spectra using the `reflkerr` model, allowing $r_{\rm in}$ and q to fit freely. In all cases we found good fits with $\chi^2/{\rm DoF} \lesssim 1.2$ (an example is shown in Figure 9) with the fitted $q \simeq 3$, $r_{\rm in}$ slightly lower than the corona size (see Figure 10), and the remaining parameters close to these assumed for the synthetic spectra (except for a, which is unconstrained for this large $r_{\rm in}$).

To further investigate the issue of the corona extent, we find the corona size for which it can be reasonably approximated by a point-like source. We generated synthetic `NICER` spectra with the same settings as above (in particular, the same flux and exposure time) using the `reflkerrD_lp` model, i.e. for a point-like source located at h, and we fitted them using `reflkerrD_elp` with a fixed size of the corona.

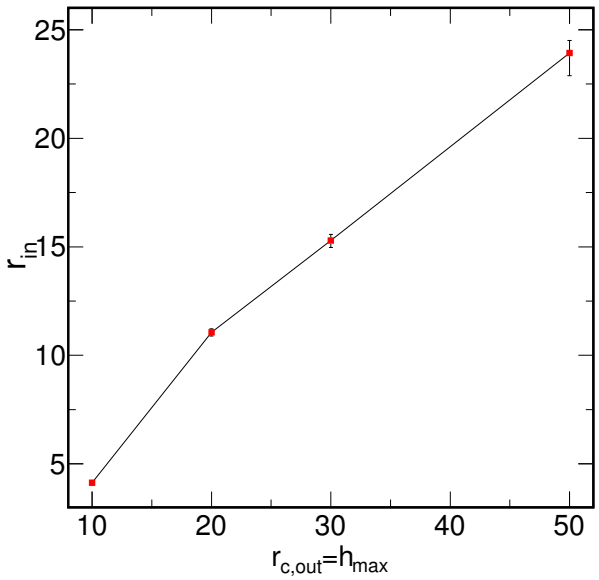

Figure 10: The values of $r_{\rm in}$ fitted to spectra generated for an untruncated disk irradiated by an extended corona (see text), shown as a function of the corona size.

For $h = 2.5$ we first set $r_{\rm c,out} = 0.2$, $h_{\rm min} = 2.3$, $h_{\rm max} = 2.7$, and then we increase both the radius and vertical size of the corona ($r_{\rm c,out} = 0.5$, $h_{\rm min} = 2$, $h_{\rm max} = 3$, and so on). We set $r_{\rm in} = r_{\rm ISCO}$ and we allow the remaining parameters (in particular, Γ, ξ, $A_{\rm Fe}$, i) to fit freely. Figure 11 shows the reduced χ^2 of the fits as a function of the size for $h = 2.5$, 5 and 7. We see that even for relatively large $h = 7$[3], only the small $r_{\rm c,out} = 0.2$ gives an acceptable approximation with $\chi^2/{\rm DoF} \simeq 1.1$. For larger sizes, the approximation quickly worsens and the residual plots in Figure 12 show increasing discrepancies.

Completing the discussion of the corona extent, in Figure 13 we compare results of `reflkerr_elp` with the empirical model fitted to `XMM` observation of a Seyfert galaxy, 1H 0707–495, by Wilkins & Fabian (2011). The comparison and related discussion were originally presented in Szanecki et al. (2020), and is restated here as it gives a clear example of nonphysical conclusions which can be related to simplified and indirect approaches applied in reflection modeling. The misleading interpretation of the empirical profile served also as an original motivation for the research reported in Section 4.

The red curve in Figure 13a shows the twice-broken power law emissivity fitted to average spectra of 1H 0707–495 by Wilkins & Fabian (2011), with the inner,

[3]the lamp-post model is typically fitted to data with smaller h

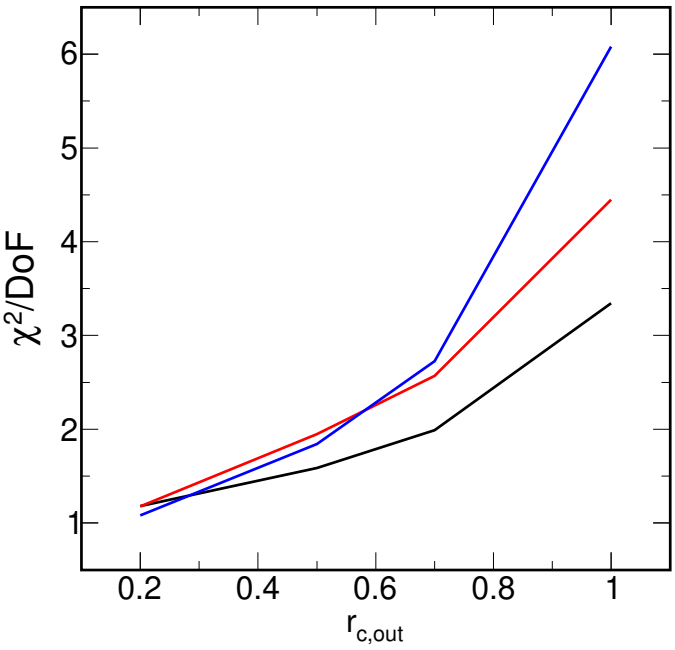

Figure 11: Reduced χ^2 as a function of the corona size, in the `reflkerr_elp` fits to the synthetic `NICER` spectrum for a point-like source at $h = 2.5$ (blue), 5 (red), and 7 (black); see text. The fitted spectra for $h = 2.5$ are shown in Figure 12.

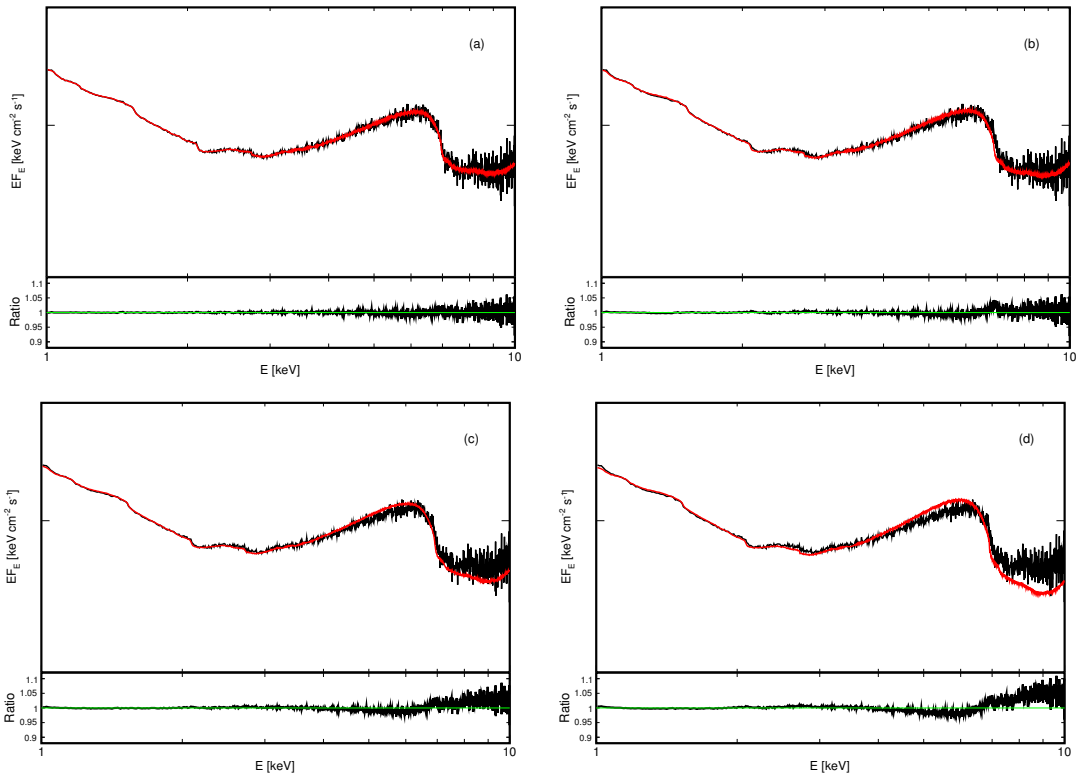

Figure 12: The black points show the synthetic spectrum of `NICER` observation for the model spectrum computed with `reflkerr_lp` with $h = 2.5$; the red lines show the spectrum fitted with `reflkerr_elp` with $r_{\rm c,out} = 0.2$ (a), 0.5 (b), 0.7 (c), and 1 (d) (see text).The lower panels show the fit residuals given as the data-to-model ratio.

middle and outer indices of $q_1 = 7.8$, $q_2 = 0$ and $q_3 = 3.3$, respectively, and the breaking radii of $r_{\rm br,1} = 5.6$ and $r_{\rm br,2} = 35$. Wilkins & Fabian (2012) argued that this inferred emissivity profile is consistent with that produced by an X-ray source with $r_{\rm c,out} \simeq r_{\rm br,2}$ (specifically, with $h_{\rm min} = 2$, $h_{\rm max} = 10$ and $r_{\rm c,out} = 30$). The blue curve in Figure 13a shows the actual emissivity of such an extended corona explicitly calculated with our `reflkerr_elp`. Our assumptions concerning the X-ray source are exactly the same as those of Wilkins & Fabian (2012), and indeed our radial profile agrees with theirs (Figure 15(b) in Wilkins & Fabian 2012). However, it differs substantially from the empirical profile of Wilkins & Fabian (2011). The empirical profile fitted to 1H 0707–495 indicates a major contribution of radiation reflected from $r < 5$, which suffers a strong redshift. However, while the irradiation profile produced by an extended source does steepen at $r \lesssim 5$ (due to the blueshift of photons arriving at this region from X-rays produced in the corona at larger distances), this effect is too weak to reproduce the extremely steep (with $q \simeq 8$) inner part of the empirical profile. The contribution of reflection arising from $r < 5$ is only 15 per cent for the actual profile of an extended corona irradiating the disc, whereas it equals 97 per cent for the empirical profile. The actual extended-corona model (i.e. `reflkerr_elp`) matches well to the change in q seen a larger radii, from $q \simeq 0$ at $r \lesssim r_{\rm c,out}$ to $q \simeq 3$ at $r \gtrsim r_{\rm c,out}$. This is a simple geometrical effect, reproduced also in flat space-time, however, it is of minor importance for the total reflection spectrum as so little of the total reflection signal is produced at these radii. The large difference in emissivity from the central regions translates into a clear difference in predicted spectra, as shown in Figure 13(b). The extended corona of Wilkins & Fabian (2012) does not give the same reflected spectrum as derived from the empirical emissivity profile fit to the data from 1H 0707–495.

2.3 Rotation

The finite size of the corona in `reflkerr_elp` means that we may include its dynamics. In the version of the model presented and applied in Szanecki et al. (2020) we assumed that the corona corotates with the disk, i.e. the angular velocity of the corona at $(r,\, \theta)$ equals the Keplerian velocity, $\Omega_{\rm K}(r_{\rm c})$, where $r_{\rm c} = r \sin\theta$. For $r_{\rm c} < r_{\rm ISCO}$ we assumed rigid rotation with $\Omega_{\rm K}(r_{\rm ISCO})$, where $r_{\rm ISCO}$ is the radius of

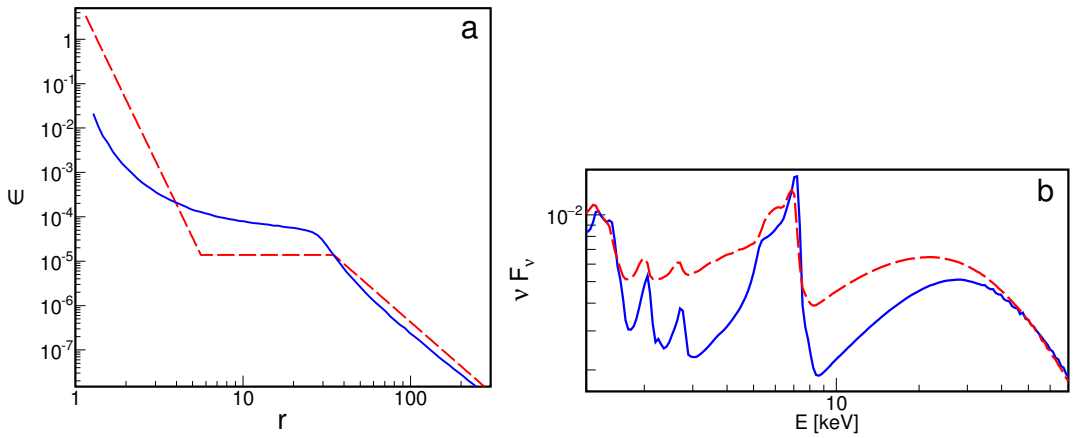

Figure 13: (a) The red line shows the twice-broken power law radial emissivity profile fitted to 1H 0707–495 by Wilkins & Fabian (2011), see text. The blue line shows the emissivity profile produced by the X-ray source with $h_{\rm min} = 2$, $h_{\rm max} = 10$, $r_{\rm c,out} = 30$ and $\Gamma = 3.1$. (b) Reflection spectra for the emissivity profiles shown in (a), with $\Gamma = 3.1$, $\xi = 53$, $A_{\rm Fe} = 9$, $i = 54°$ and $r_{\rm in} = r_{\rm ISCO}$; the difference of spectral shapes is only due to different amounts of relativistic distortion corresponding to the difference of the radial profiles. Figure readapted from Szanecki et al. (2020).

the innermost stable circular orbit. Our assumptions about co-rotation with the disk at $r_{\rm c} \geq r_{\rm ISCO}$ and rigid rotation at $r_{\rm c} < r_{\rm ISCO}$ appear to be natural, and are the only choices which can be justified *ab initio*. In the model applied here, however, we allow the angular velocity, Ω, to fit freely by scaling $\Omega_{\rm K}$. For parameters fitted to 1H 0707–495 in Section 4, i.e. low h and small $r_{\rm c,out}$, the change of Ω around $\Omega_{\rm K}$ results in moderate changes of $\mathcal{R}_{\rm obs}$ by a factor $\lesssim 2$, without a significant change of the spectral shape, as shown in Figure 14. The corresponding changes in the irradiation profile are shown in Figure 15.

We note that in some other ranges of parameters, rotation may have a larger effect, increasing $\mathcal{R}_{\rm obs}$ by a factor of ~ 10 and at the same time leading to significant changes of the observed shape of the reflected spectrum. These effects were discussed in Szanecki et al. (2020) and are not relevant to the results presented in this dissertation, therefore, this discussion is not repeated here.

2.4 Outflow

A source on the symmetry axis can be associated with the region of jet formation (e.g. Ghisellini et al. 2004) and then it is likely that such a source moves outward along the symmetry axis. Such a motion was considered by Dauser et al. (2013) and

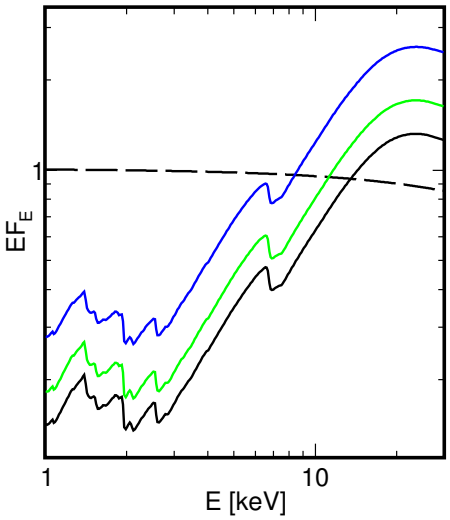

Figure 14: The dashed line shows the directly observed spectrum of the corona and the solid lines show the reflected spectra for $a = 0.998$, $r_{\rm in} = r_{\rm ISCO}$, $h_{\rm min} = 1.5$, $h_{\rm max} = 3.5$, $r_{\rm c,out} = 0.5$, $\Gamma = 2$, $\xi = 100$, $\mathrm{A_{Fe}} = 1$, $\mathcal{R} = 1$ and (black) $\Omega = 0$, (green) $\Omega = \Omega_{\rm K}$, and (blue) $\Omega = 1.5\Omega_{\rm K}$.

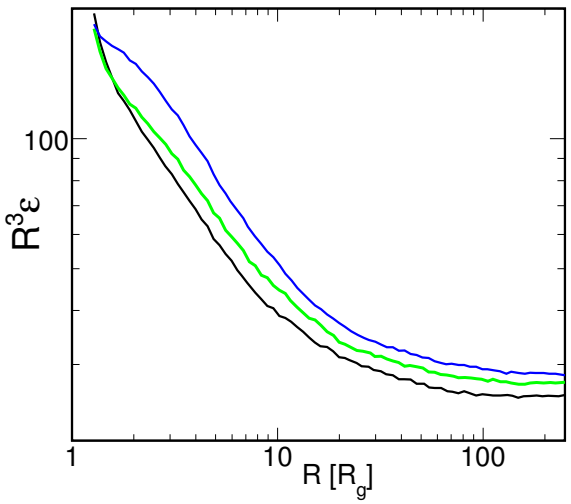

Figure 15: The change of the irradiation profile corresponding to the change of Ω for parameters given in the caption of Figure 14 and using the same color scheme.

it is implemented in their `relxilllpCp` model. The model has been applied e.g. by Porquet et al. (2021) and You et al. (2021) to find the velocity of the X-ray source. The other (public) relativistic reflection models, i.e. `kyn`, `reltrans` and `reflkerr`, and also the recent version 2.0 of `relxilllpCp`, allow scaling the predicted strength of reflection to approximate the effect of non-isotropic X-ray emission (the scaling parameter, $\mathcal{R}$, is defined in Section 1.6). This approach, however, neglects other effects resulting from the non-isotropy, in particular, the change of the radial emissivity profile (see e.g. fig. 9 in Fukumura & Kazanas 2007). Then, spectra predicted by these models for the scaling parameter significantly different from unity are not self-consistent and the results of their application may be unphysical. In particular, a non-isotropy sufficiently large to yield a substantial reduction of reflection would also remove the steep part of the profile close to the black hole, characteristic to the lamp-post model (see fig. 5 in Niedźwiecki et al. 2016), which effect is not accounted for in models with a free scaling of reflection.

Here we reconsider the effect of vertical motion of the X-ray source. We developed a new `xspec` model, `reflkerrV`, implementing it. Below we describe this model, compare it with `relxilllpCp`, and discuss differences between these models.

We consider an X-ray source on the symmetry axis of a Kerr black hole, as shown in Figure 6, except that the source now does not rotate. We take into account the spatial extent of the source with the same geometrical setup as in `reflkerr_elp`, i.e. we assume that it has a cylindrical shape with radius $r_{\rm c,out}$ and is located symmetrically around the black hole rotation axis between a lower height $h_{\rm min}$ and upper height $h_{\rm max}$. We assume that the emission region is static, however, electrons in it undergo a bulk motion in the direction perpendicular to the disk with velocity v as measured in the locally non-rotating frame (LNRF, Bardeen et al. 1972). In this assumption, we follow the physical model of Beloborodov (1999) with an X-ray source dominated by $e^{\pm}$ pairs, which are ejected away by the radiation pressure, immediately cool down and are replaced by newly created pairs.

The model `reflkerrV` is included in the `reflkerr` family and we strictly follow the theoretical framework described in Section 1.6.2, i.e. we construct the source-to-disk ($\mathcal{T}_{\rm sd}$) and source-to-observer ($\mathcal{T}_{\rm so}$) transfer functions by tabulating a large number of photon trajectories. We assume that the intrinsic X-ray emission is isotropic

and we generate photons with an isotropic distribution of initial directions in the frame co-moving with electrons. We then make the Lorentz transformation to the LNRF frame, we find the constants of motion and we compute the photon trajectory using the method of Niedźwiecki & Życki (2008). The fluxes of photons reaching the disk, tabulated in $\mathcal{T}_{\rm sd}$, and directly observed, tabulated in $\mathcal{T}_{\rm so}$, are affected by the relativistic aberration and Doppler effects, however, there is no retardation effect, see Rybicki & Lightman (1979); we discuss this issue below.

All `reflkerrV` spectra presented below in this Section are computed for $\Delta h \ll h$ and $r_{\rm c} \ll h$, which reproduces spectra for a point-like source, where $\Delta h = h_{\rm max} - h_{\rm min}$ and $h = (h_{\rm min} + h_{\rm max})/2$. This allows for safe comparison with `relxilllpCp`. Specifically, we set $\Delta h = 0.2$ and $r_{\rm c} = 0.2$ (which in all cases gives a precise imitation of a point-like source, see Section 2.2) and for brevity, we only give the values of h.

The outward motion of radiating electrons affects the observed spectrum through several effects: (i) weaker relativistic broadening due to reduced irradiation of the innermost disk; (ii) reduction of the incident flux due to the Doppler redshift and collimation away from the disk, (iii) decrease or increase (depending on i) of the directly received (i.e. not reflected) flux due to the Doppler shift and collimation; (iv) decrease of the high-energy cut-off of the incident spectrum due to the Doppler redshift; and (v) Doppler shift of the high-energy cut-off of the directly observed spectrum. The effect (iv) affects both the reflected Compton hump, whose shape is sensitive to the position of the high-energy cut-off (Magdziarz & Zdziarski 1995) and the soft X-ray part of the reflected spectrum (García et al. 2015a). For effects (iv) and (v) we note that it is important to properly shift in energy the precise Comptonization spectrum rather than to apply scaling of temperature in a non-relativistic Comptonization model, e.g. in `nthcomp` used in `relxill` and in `reltrans`. The latter approach may lead to nonphysical results if the implied rest-frame temperature is relativistic, see e.g. Szanecki et al. (2021).

Figure 16 illustrates these effects by showing changes in the reflection spectra corresponding to the increase of v. For face-on observers, this leads to an increasing reduction of the reflected component. However, the decrease in relativistic broadening for increasing v is also clear, as is the change in the shape of the Compton hump. Figure 17 shows the corresponding radial profiles, illustrating the above effect (i).

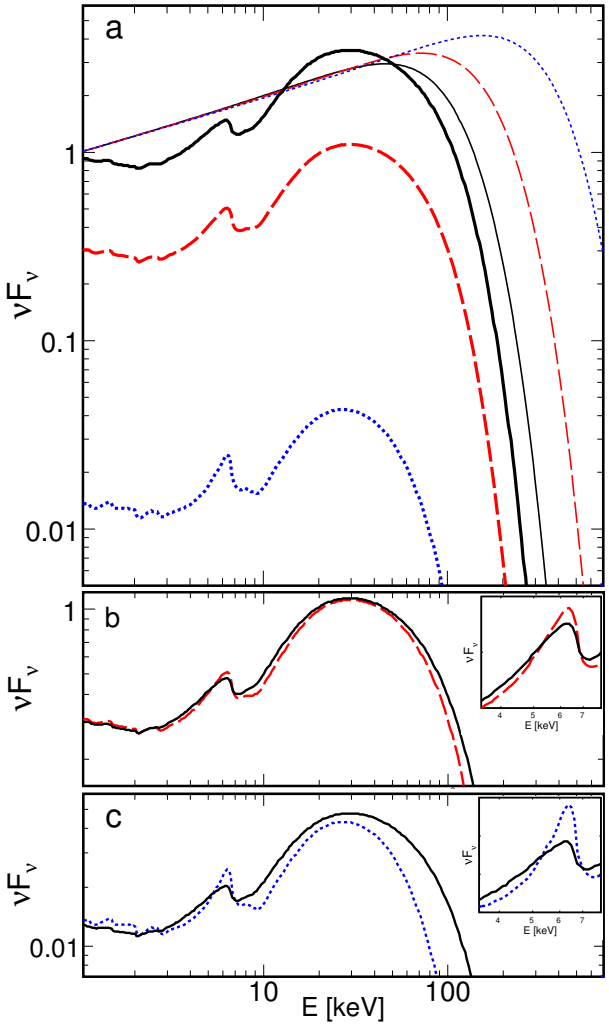

Figure 16: (a) Observed primary and reflected spectra for $a = 0.998$, $r_{\rm in} = r_{\rm ISCO}$, $h = 3$, $i = 20°$, $\Gamma = 1.7$, $kT_{\rm e} = 40$ keV and $\beta = 0$ (solid black), 0.44 (dashed red) and 0.88 (dotted blue), computed using `reflkerrV`. The ionization parameter $\xi = 10^3$ and the relative iron abundance $\mathrm{A_{Fe}} = 1$. Panels (b) and (c) show the same reflection spectra for $\beta = 0.44$ and 0.88, respectively, together with the reflection spectrum for $\beta = 0$ rescaled by $\mathcal{R} = 0.32$ in (b) and by $\mathcal{R} = 0.014$ in (c); the inner panels show the same focused on the Fe Kα line. The difference between spectra shown in the bottom panels gives the inaccuracy related with setting the reflection scaling parameter to values different from unity.

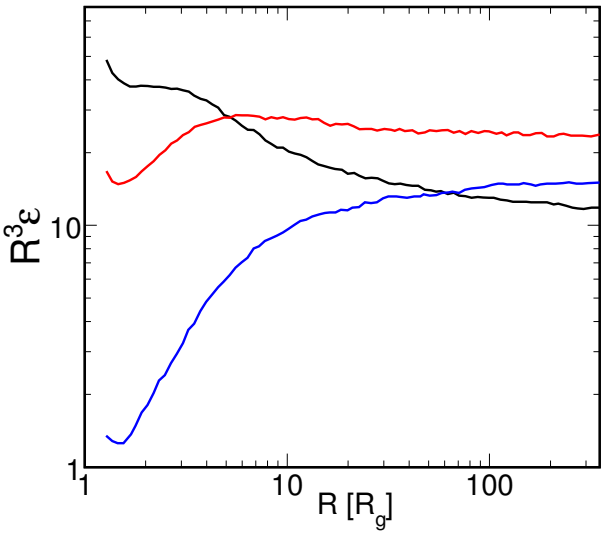

Figure 17: The change in the radial profile corresponding to the increase of the outflow velocity. Parameter settings and color coding are the same as in Figure 16, i.e. $a = 0.998$, $r_{\rm in} = r_{\rm ISCO}$, $h = 3$, and $\beta = 0$ (black), 0.44 (red) and 0.88 (blue).

All spectra presented in this section, correspond to the physical normalization of the reflected component, $\mathcal{R} = 1$[4], except for Figure 16bc and Figgure 18cd, where for illustration we use $\mathcal{R} < 1$. Allowing for a free normalization of reflection with respect to the directly observed component, which has become a common practice in applications of the LP model, takes into account only the above effects (ii) and (iii), neglecting the remaining ones. Panels (b) and (c) in Figure 16 illustrate inaccuracy related to approximating the non-isotropy of the X-ray source by simple rescaling of the reflection component.

In Figure 18 we compare spectra computed with `reflkerrV` and `relxilllpCp`. We note that the outflow effect was incorrectly implemented in version 2.0 and earlier versions of `relxilllpCp`. The corrected version 2.1[5] gives a systematically lower reflection strength than `reflkerrV`, which appears to be due different physical assumptions in these models, as discussed below.

We first estimate the factor by which the vertical motion decreases the amplitude of reflection. We denote by $\mathcal{F}$ the ratio of the energy flux directly reaching the observer to the luminosity intercepted by the disc. For a power-law spectrum with the photon spectral index Γ, we have $\mathcal{F}(\beta) \simeq \mathcal{F}(0)\mathcal{A}^{-1}\delta_{\rm obs}^2(\delta_{\rm obs}/\delta_{\rm eff})^{\Gamma-1}$, where the last term gives the change of the observed and incident fluxes due to the shift in

[4]technically, this scaling parameter is called `boost` in `relxilllpCp` and `rel_refl` in `reflkerrV`

[5]the description of outflow in `relxilllpCp` was corrected following the submission of our work, Klepczarek et al. (2023), which described the problem

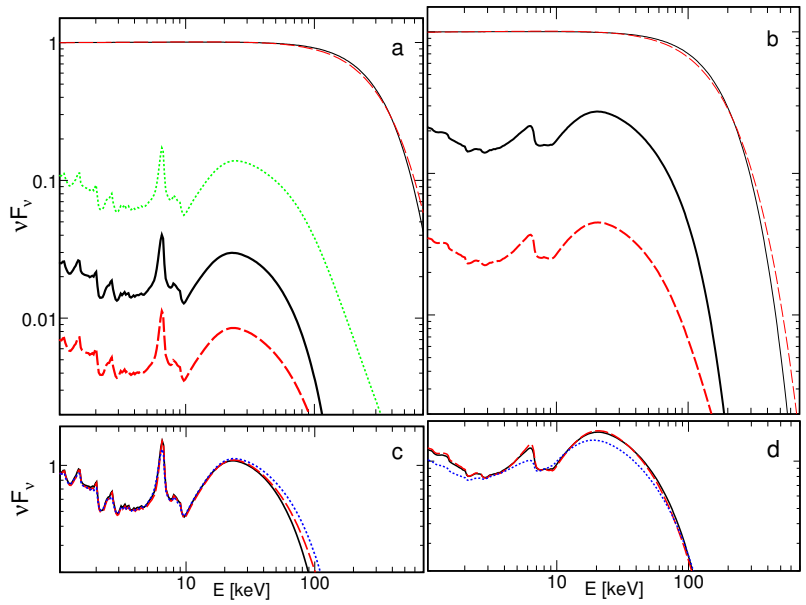

Figure 18: Comparison of the observed spectra computed with `reflkerrV` (solid black), `relxilllpCp` v. 2.1 (dashed red) and v. 2.0 (dotted green in panel a) for $\beta = 0.66$, $a = 0.998$, $r_{\rm in} = r_{\rm ISCO}$, $\theta = 20°$, $\Gamma = 2$, $\xi = 10^3$, $\mathrm{A_{Fe}} = 1$, (a,c) $h = 30$ and (b,d) $h = 2$. In `reflkerrV`, the (rest-frame) $kT_{\rm e} = 50$ keV. In `relxilllpCp`, $kT_{\rm e} = 100$ keV, for which its primary spectrum matches that of `reflkerrV` (compensating for the shortcomings of `nthcomp`, see Niedźwiecki et al. 2019). Panels (a,b) show spectra with the physical normalization of reflection. Panels (c,d) show the same spectra with the reflected components rescaled by (c) $\mathcal{R} = 36$ in `reflkerrV` and $\mathcal{R} = 130$ in `relxilllpCp` and (d) $\mathcal{R} = 5.6$ in `reflkerrV` and $\mathcal{R} = 35$ in `relxilllpCp`. The bottom panels show also the `reflkerrV` spectra for $\beta = 0$ and the same remaining parameters as the top panels, in particular $kT_{\rm e} = 50$ keV, and the physical normalization of reflection (blue dotted).

energy, $\delta_{\rm obs}^2$ is the aberration factor for the directly received photon flux, $\mathcal{A}$ denotes the reduction of the photon flux emitted toward the disc, $\delta_{\rm obs} = 1/[\gamma(1-\beta\mu)]$, $\mu = \cos i$, $\gamma = (1-\beta^2)^{-1/2}$, $\beta = v/c$, $\mathcal{F}(0)$ is for $\beta = 0$ and for the sake of discussion of the involved effects we defined the effective Doppler shift of photons reaching the disc, $\delta_{\rm eff} = \int \delta_{\rm irr}(r) n_{\rm ph}(r) r{\rm d}r / \int n_{\rm ph}(r) r{\rm d}r$, where $\delta_{\rm irr}(r)$ and $n_{\rm ph}(r)$ are the radius-dependent Doppler factor and flux of incident photons. The above expression for $\mathcal{F}(\beta)$ agrees to better than 1 per cent with equation (3) in Beloborodov (1999).

Neglecting the light bending, we have $\mathcal{A} = (1-\beta)$, which follows from $\mu = (\mu' - \beta)/(1-\beta\mu')$, where μ' is the cosine of the emission angle in the co-moving frame. At $h = 30$ and $\beta = 0.66$, we get $\delta_{\rm eff} \simeq 0.6$ and then, for $\Gamma = 2$ and $i = 20^\circ$, $\mathcal{F} \simeq 38\mathcal{F}(0)$. Taking into account the (weak) light bending at $h = 30$, we get $\mathcal{F}_{\rm GR} \simeq 36\mathcal{F}_{\rm GR}(0)$. We indeed find that the reflected component is reduced by this factor in `reflkerrV` (Figure 18a,c).

At low h, the beaming effect is less effective in the reduction of reflection, as the light-bending causes both $\delta_{\rm eff}$ and $\mathcal{A}$ to be larger than at large h. E.g. at $h = 2$ and $v = 0.66$, $\delta_{\rm eff} \simeq 1$ and $\mathcal{A} \simeq 0.9$ (the flux of photons directly observed increases at the expense of the flux of photons trapped by the black hole, however, the total flux of photons incident on the disk is weakly affected). Then, for $i = 20^\circ$ and $\Gamma = 2$, $\mathcal{F}_{\rm GR} \simeq 10\mathcal{F}_{\rm GR}(0)$. Moreover, while the total irradiating flux changes weakly, its radial distribution changes significantly; the photon flux irradiating the disk at $r < 2$ ($r > 6$) decreases (increases) by a factor of $\simeq 2$. As a result, the reflected component computed with `reflkerrV` for $i = 20^\circ$ and $\beta = 0.66$ is reduced by only a factor of $\simeq 0.18$ compared to $\beta = 0$ (see Figure 18b,d), as reflection from $r < 2$ contributes weakly to the observed reflection.

In the above, we neglected the retardation terms, because the emission region is located at a fixed h in our LP model. For an emission region receding from the disc, the retardation effect would have to be taken into account. Then, $\mathcal{F}(\beta)/\mathcal{F}(0)$ would be increased by $\delta_{\rm obs}/\delta_{\rm eff}$ at large h (i.e. neglecting GR), which gives the factor of $\simeq 3.3$ for the case shown in Fig. 18a, explaining the difference between `reflkerrV` and `relxilllpCp` v. 2.1. At this large h the retardation effect does not affect the spectrum of the reflected component, which arises mostly from a range of radii corresponding to a narrow range of $\delta_{\rm irr} \approx \delta_{\rm eff}$. We indeed note a good agreement

of the spectral shape of reflection computed with `reflkerrV` and `relxilllpCp`, see Fig. 18c. At low h, the retardation changes the relative contribution of photons reflected at different radii, which slightly affects the spectral shape, e.g. leading to $\lesssim 10$ per cent differences between the `reflkerrV` and `relxilllpCp` spectra in Figure 18d.

Models assuming a motion of the source itself (rather than a motion within it) should be applied using a vertically extended emission region with a large $h_{\rm max}$, rather than a point-like source, because typical observation times exceed the time-scale for mildly-relativistic propagation beyond $100R_{\rm g}$ even for supermassive black holes.

Finally, we note also that the reduction of reflection strength may be due to the intrinsic non-isotropy of the X-ray source instead of the kinematic collimation. The above remarks remain valid for such a case, i.e. the change of the radial profile corresponding to this non-isotropy should also be taken into account. `reflkerrV` can be used to self-consistently approximate these alternative non-isotropy effects, as the retardation obviously should not be included for such an approximation. A particularly relevant effect concerns the non-isotropy of the Comptonization process. This effect is implemented in the `compps` model and then can be accurately taken into account in spectral modeling. We note, however, that this non-isotropy is relatively weak (as compared to that due to the outflow) and leads to changes of the reflection strength by at most a factor of ~ 2 (see e.g. figure A1 in Niedźwiecki et al. (2019)).

2.5 Summary

We considered the effect of the vertical outflow at the X-ray source in the popular relativistic-reflection model assuming the lamp-post geometry. We pointed out effects involved in spectral formation and we implemented them in the new model, `reflkerrV`. We note differences with `relxilllpCp`, mostly in the reflection strength, related with the neglect of retardation effect in our model corresponding to our assumption of a steady location of the lamp-post source.

We discussed differences between the lamp-post model fitted with a free normalization of the reflected component and the model with a self-consistent description of

the non-isotropy of the X-ray source. In Section 3 we will show how these differences manifest themselves in the direct application for data analysis.

With good quality data, models assuming a point-like X-ray source give a good approximation for extremely compact coronae. We emphasize, that this property was found in the model assuming an untruncated disk. For $r_{\rm in} > r_{\rm ISCO}$, a good match occurs even for relatively extended coronae (with sizes corresponding to $r_{\rm in}$, see Section 3).

3 Hard-state of Cygnus X-1

3.1 Introduction

Cyg X-1 is probably the best studied black-hole system. The X-ray binary contains a black hole in a 5.6-day orbit with a more massive supergiant donor star. The parameters of the binary have been recently refined by Miller-Jones et al. (2021) to $i = 27.5^{+0.8}_{-0.6}{}^{\circ}$ for the binary inclination, $M = 21.2 \pm 2.2 M_{\odot}$ for the black hole and $M = 40.6^{+7.7}_{-7.1} M_{\odot}$ for the companion, and the distance $D = 2.22^{+0.18}_{-0.17}\,\mathrm{kpc}$. Miller-Jones et al. (2021) also assessed the black hole spin parameter to $a > 0.9985$ by disk continuum fitting method in the soft states. This would indicate that the black hole in Cyg X-1 was born with an extreme value of the spin, because in the binary system with a high-mass donor star, the black hole cannot have been spun up by accretion from its companion at the maximum (Eddington) rate, as that would require a much longer time than the lifetime of the donor ($\sim 4\,\mathrm{Myr}$). However, the robustness of the disk continuum method has recently been questioned, as noted in Section 1.8.

Cyg X-1 is usually observed in the hard state for which, using the reflection spectroscopy, some works found a disk extending to the ISCO of a rapidly rotating black hole (Parker et al. 2015; Reis et al. 2010), and some a truncated disk (Basak et al. 2017; Done & Zycki 1999; Yamada et al. 2013). For the particular observation performed simultaneously by `Suzaku` and `NuSTAR`, considered in detail in this section, Parker et al. (2015) found a description with a lamppost containing hybrid electrons at $h < 2$, $r_{\rm in} \simeq r_{\rm ISCO}$ and $a \simeq 1$. The same observation, however, was explained by Basak et al. (2017) with a model with $r_{\rm in} \gg r_{\rm ISCO}$ and unconstrained a, and a continuum described by two Comptonization components (the observational evidence that at least two such components are present in Cyg X-1 are reviewed by Basak et al. 2017). Basak et al. (2017) also pointed out some physical shortcomings in the hybrid model of Parker et al. (2015), namely, the unrealistic size of the X-ray source implied by the fitted `eqpair` parameters. The lamp-post models of both Parker et al. (2015) and Basak et al. (2017) assume a free reflection normalization, which they found to be lower by a factor $\gtrsim 5$ than predicted for the fitted lamp-post parameters. Below we use `reflkerrV` to demonstrate how these results are affected when the reduction of reflection is accounted for by beaming effects in a physically

consistent model.

The accretion geometry in the hard state of Cyg X-1 was recently probed with the X-ray polarization by the Imaging X-ray Polarimetry Explorer (Krawczynski et al. 2022; `IXPE`). This polarimetric measurement indicates that the X-rays are produced in a hot gas that is flattened in the direction orthogonal to the relativistic jet observed in the system, e.g. in the truncated disk/hot inner region geometry. This flattened corona must have a relatively high inclination to the observer, $i \gtrsim 45°$, which implies a misalignment between the binary axis and the black hole spin (Zdziarski et al. 2023b).

3.2 Data

We study here the `NuSTAR` and `Suzaku` observations of Cyg X-1 in its hard state. We consider the `NuSTAR` observation on 2014 May 20-21, OBSID 30001011007, and the `Suzaku` observation on 2014 May 19-22, OBSID 409049010, of which we use only the data simultaneous with the `NuSTAR`. We consider data from the FPMA and FPMB detectors onboard `NuSTAR` and from three `Suzaku` instruments, XIS1, PIN and GSO. In the data reduction, we followed the standard procedures, similarly to Parker et al. (2015) and Basak et al. (2017), and we found the data of all the detectors to be very similar to those obtained by these works. For `Suzaku` we used the standard reprocessing tool, `aepipeline` ver. 1.1.0, with its default settings and `CALDB` ver. 2016-06-07, and we generated response files with `xisrmfgen` and `xissimarfgen` ftools. The reduction of `NuSTAR` data was performed with `nupipeline` ftool and `nustardas` v1.4.1 from 2014-05-28 with standard settings and CALDB version files from 2015-03-16. All spectra were rebinned using the optimal binning of Kaastra & Bleeker (2016)

To verify that our data reduction is consistent with Parker et al. (2015) and Basak et al. (2017), we have refitted their lamp-post models to the present data[6] and obtained parameters very similar to those given in Table 4 of Parker et al. (2015) and Table 2 of Basak et al. (2017) for their model 4, with $\chi^2/\mathrm{DoF} = 665/488$ and 622/490, respectively.

[6]to recover their results we used the same reflection models as originally applied in these works, i.e. `relxilllp` ver. 0.2 for Parker et al. (2015) and `relxilllpCp` ver. 0.5 for Basak et al. (2017)

Table 1: Results of spectral fitting for our models with stratified Comptonization. All the models are defined as `tbabs*wind*(LP + compps + diskbb)`, where `LP` is described by `reflkerrV` in models 4 and 5, and `relfkerrG_lp` in model 6.

	4	5	6
		LP component	
h	$16.5^{+0.8}_{-1.6}$	$6.2^{+0.4}_{-2.2}$	$11.8^{+0.9}_{-3.1}$
a	$0.998^{+0}_{-0.998}$	0.998(f)	0.998(f)
β	$0.36^{+0.03}_{-0.01}$	$0.18^{+0.07}_{-0.07}$	$-$
$\delta_{\rm B}$	$-$	$-$	> 0.5
$r_{\rm in}$ $[R_{\rm g}]$	$r_{\rm ISCO}$(f)	$16.0^{+1.8}_{-2.0}$	$15.7^{+3.2}_{-2.4}$
i [°]	$41.7^{+0.8}_{-1.0}$	$39.6^{+1.7}_{-1.6}$	$41.1^{+2.9}_{-1.9}$
Γ	$1.71^{+0.01}_{-0.01}$	$1.72^{+0.01}_{-0.01}$	$1.72^{+0.01}_{-0.01}$
kT_e [keV]	46^{+2}_{-1}	64^{+5}_{-6}	69^{+2}_{-2}
$\rm A_{Fe}$	$2.0^{+0.1}_{-0.1}$	$2.1^{+0.2}_{-0.3}$	$2.1^{+0.1}_{-0.2}$
$\log_{10}(\xi)$	$2.86^{+0.02}_{-0.02}$	$2.88^{+0.04}_{-0.03}$	$2.86^{+0.03}_{-0.03}$
N	$1.33^{+0.08}_{-0.04}$	$1.35^{+0.04}_{-0.05}$	$1.32^{+0.03}_{-0.04}$
		`tbabs`	
N_H $[\times 10^{22}{\rm cm}^{-2}]$	$0.5^{+0.09}_{-0}$	$0.5^{+0.2}_{-0}$	$0.5^{+0.2}_{-0}$
	ionized absorber: `xstar` table model		
N_H $[\times 10^{22}{\rm cm}^{-2}]$	$2.5^{+0.1}_{-0.1}$	$2.5^{+0.2}_{-0.2}$	$2.4^{+0.1}_{-0.2}$
$\log_{10}(\xi)$	$5.00^{+0}_{-0.07}$	$5.00^{+0}_{-0.09}$	$5.00^{+0}_{-0.08}$
		`diskbb`	
$T_{\rm in}$ $[\times 10^{-2}{\rm keV}]$	$9.1^{+0.7}_{-1.9}$	$9.5^{+3.3}_{-2.5}$	$9.4^{+2.9}_{-2.3}$
N $[\times 10^{8}]$	$4.5^{+13}_{-2.6}$	$2.8^{+34}_{-2.7}$	$2.9^{+33}_{-1.7}$
		soft component: `compps`	
Γ	$2.97^{+0.25}_{-0.09}$	$3.05^{+0.37}_{-0.16}$	$2.91^{+0.36}_{-0.05}$
kT_e	7^{+1}_{-1}	7^{+28}_{-1}	6^{+1}_{-1}
N	$1.45^{+0.31}_{-0.08}$	$1.57^{+0.93}_{-0.33}$	$1.39^{+0.05}_{-0.04}$
χ^2/DoF	641/490	627/490	618/490

Notes: We use the same model of ionized absorber which was used by Parker et al. (2015) and Basak et al. (2017). The ionization parameter, ξ, is given in the unit of erg cm s^{-1}. The normalization, N, of Comptonization components gives the 1-keV flux in keV cm^{-2} s^{-1}. For the soft component we used the version of `compps` parametrized by Γ, see Niedźwiecki et al. (2019). (f) denotes a fixed parameter.

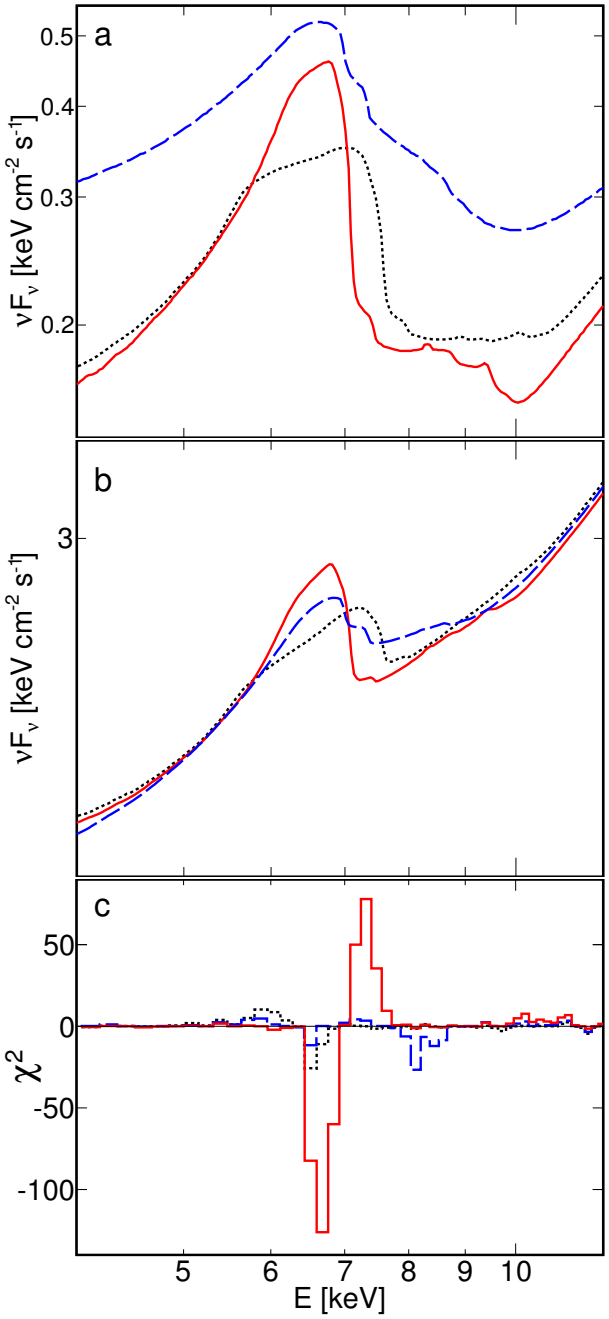

Figure 19: Illustration of spectral effects corresponding to using either an outflow or a free scaling of reflection in the model of Parker et al. (2015), see text. In all panels, the black dotted lines are for model 1 (with $\beta = 0$ and free $\mathcal{R}$), the red solid lines are for model 2 and the blue dashed lines are for model 3. Models 1 and 2 use the same parameters of `eqpair`, A_{Fe} and ξ, so the difference between the solid and dotted lines directly reflects the spectral differences shown in Figure 16bc. a) Reflection components. b) Total spectra. c) Fit residuals given as χ^2 contributions for `NuSTAR`; the FPMA and FPMB data are co-added for clarity of this figure.

3.3 Model

We use `reflkerrV`, described in Section 2.4, in which we convolve $\mathcal{T}_{\rm sd}$ with the rest-frame reflection model `hreflect` to find the radius-dependent reflection spectrum. As described in Section 1.6.1, `hreflect` is the hybrid model, using `xillver` (García et al. 2013) in the soft X-ray range and `ireflect` (Magdziarz & Zdziarski 1995) in the hard X-ray range, and applying correction on the temperature parameter in `xillver` to account for inaccuracies of `nthcomp` applied in `xillver` (Niedźwiecki et al. 2019). We convolve $\mathcal{T}_{\rm so}$ with the Comptonization model `compps` (Poutanen & Svensson 1996) to find the spectrum of the directly observed radiation. The model is parameterized by the electron temperature, $T_{\rm e}$, measured in the rest-frame of the X-ray source. The inclination angle of a distant observer is denoted by i.

We construct spectral models similar to those of Parker et al. (2015) and Basak et al. (2017), namely, we include the disk blackbody component modelled with `diskbb` (Mitsuda et al. 1984), the interstellar absorption modelled by `tbabs` with $N_{\rm H} = (5-7)\times10^{21}$ cm^{-2}, and the ionized absorber described by the model based on `XSTAR` (the model of absorber used in this section was computed by Michael Parker for Parker et al. 2015)

3.4 Results

We address here works which assumed a point-like lamp post. To make comparisons unaffected by the source extent in our model, we use `reflkerrV` spectra computed for $r_{\rm c,out} = 0.2$ and $\Delta h = h_{\rm max} - h_{\rm min} = 0.2$ (which in all cases gives a precise imitation of a point-like source, see Section 2.2) and for brevity, we only give the values of $h = (h_{\rm min} + h_{\rm max})/2$. This assumption is released when we find constraints on the corona size in the fitted models.

We first consider the solution of Parker et al. (2015) in which the primary continuum component is fully described by the hybrid Comptonization model `eqpair` (Coppi 1999). Similarly to Parker et al. (2015), we add to it the relativistic reflection, for which we use `reflkerrV`; we include only the reflection component of this model. To describe the normalization of the `reflkerrV` reflection relative to the `eqpair` continuum, we define $\mathcal{R}$ as the ratio of the 10-keV fluxes of the primary component of `reflkerrV` to that of `eqpair`. Setting $\beta = 0$ and allowing for a free

$\mathcal{R}$, we find the best-fit similar to that of Parker et al. (2015), with $a = 0.98^{+0.01}_{-0.01}$, $h = 1.3^{+0.1}_{-0.1}$, $r_{\rm in} = 2.3^{+0.1}_{-0.1}$, $i = 49.7^{+0.5^\circ}_{-1.4}$, $A_{\rm Fe} = 4.2^{+0.1}_{-0.1}$, $\log_{10}(\xi) = 2.98^{+0.02}_{-0.02}$ and $\mathcal{R} = 0.13^{+0.06}_{-0.01}$ at $\chi^2/{\rm DoF} = 655/487$ (model 1). Then, we set $\mathcal{R} = 1$ (i.e. the physical value) and use a free β. The corresponding spectral changes are shown in Figure 19. To illustrate the effect of self-consistent inclusion of the effects of non-isotropy instead of the free scaling of reflection, we first fix $A_{\rm Fe}$, ξ and the parameters of the primary component (`eqpair`) at the values found above for the model 1 and we allow only the relativistic-blurring parameters of `reflkerrV` to fit freely. This gives a very poor fit for $a = 0.25^{+0.01}_{-0.01}$, $h = 1.7^{+0.1}_{-0.1}$, $r_{\rm in} = 5.1^{+0.1}_{-0.1}$, $\beta \simeq 0.86^{+0.02}_{-0.04}$ and $i = 34.5^{+0.1^\circ}_{-0.2}$ (model 2) with $\Delta\chi^2 = +459$ with respect to our fit with model 1 and strong systematic residuals in the 6–8 keV range (the solid line in Figure 19c). Then, we allow all parameters of the model to fit freely. The change in relativistic blurring for $\beta > 0$ is then partially compensated by the change of $A_{\rm Fe}$ and ξ and we get $\chi^2/{\rm DoF} = 703/487$ for $a = 0.1^{+0.1}_{-0.1}$, $h = 2.2^{+0.2}_{-0.1}$, $r_{\rm in} = 6^{+1}_{-1}$, $A_{\rm Fe} \simeq 3.4^{+0.1}_{-0.2}$, $\log_{10}(\xi) \simeq 3.31^{+0.01}_{-0.01}$, $\beta \simeq 0.82^{+0.06}_{-0.12}$ and $i = 31^{+1^\circ}_{-1}$ (model 3). For the sake of the discussion below of the role of Comptonization of reflection in the X-ray corona in the original model of Parker et al. (2015) (i.e. with $\beta = 0$ and free $\mathcal{R}$), we also allowed $r_{\rm c,out}$ in model 1 to fit freely and we found the upper limit of $r_{\rm c,out} < 0.9$.

We then consider the model of Basak et al. (2017) with stratified Comptonization, i.e. we include an additional, soft Comptonization component. Model definitions and fitting results are shown in Table 1. We first assume $r_{\rm in} = r_{\rm ISCO}$ (model 4) and we find a good fit for $\beta \simeq 0.36$. We then allow $r_{\rm in}$ in `reflkerrV` to vary (model 5). The spin value cannot be constrained, therefore, we fix $a = 0.998$. In agreement with Basak et al. (2017) we find that $r_{\rm in} \simeq 16$ is preferred. Allowing for $r_{\rm in} > r_{\rm ISCO}$ improves the fit and this version represents our best spectral solution with `reflkerrV`. Reflection from such a truncated disk is still relatively strong and a subrelativistic outflow of the X-ray source at $\beta \simeq 0.2$ is needed to reduce it to the observed level.

Figures 20 and 21 show the probability distribution of parameters in model 5 obtained with the Markov Chain Monte Carlo (MCMC) method. For this MCMC analysis we allowed a, $r_{\rm c,out}$, $h_{\rm min}$ and Δh to fit freely. We see a correlation between i and $r_{\rm in}$ and we note that $i \simeq 45^\circ$ corresponding to $r_{\rm in} \simeq 20$ would be consistent

with assessment of inclination based on the IXPE measurement. The spin is unconstrained, with an insignificant ($\lesssim 1\sigma$) preference for high a (resulting from a minor dependence of the redshift of photons arriving to the disk on the space-time metric). For the geometry of the X-ray source we find $r_{\rm c,out} = 6.5^{+6.7}_{-6.4}$, $h_{\rm min} = 3.9^{+2.2}_{-1.9}$, $\Delta h = 4.3^{+4.8}_{-3.3}$. Then, the X-ray source may be relatively extended. At the main constraint that we find, $r_{\rm c,out} < r_{\rm in}$ and $h_{\rm max} < r_{\rm in}$, the irradiation of the surrounding disk follows $\varepsilon \propto r^{-3}$, which then appears to be preferred by the data.

Alternatively to an outflow, the reduction of reflection may be due to the presence of the X-ray source located on the opposite to observer side of the black hole (referred to as the bottom source), which is visible when the optically thick disk is truncated. This source negligibly contributes to the disk irradiation while significantly increasing the directly observed radiation, and thus reducing the reflection strength, see Niedźwiecki & Zdziarski (2018) and Niedźwiecki et al. (2019). To study such a solution, we use the `relfkerrG_lp` model of Niedźwiecki et al. (2019), with two symmetrically located, static X-ray sources (model 6). In this model, the attenuation of the bottom source is given by the parameter $\delta_{\rm B}$ (= 1 for a full contribution of this source). The model 6 gives our overall best spectral solution and we show it in Figure 22a,b.

Our fitted models indicate that reduced reflection from the central $16R_{\rm g}$ is preferred to fit the data, which may be explained by either an outflow or a disk truncation, see Figure 22c. The difference in relativistic broadening corresponding to these two cases is small, see Fig. 22d, yet it gives rise to the systematic difference in the Fe Kα range in the residuals for the fitted models, see Figure 22e.

3.5 Summary and discussion

We found that `reflkerrV` gives a good description of the X-ray spectrum of Cyg X-1 in its hard state for $\beta = 0.36$, which value is in approximate agreement with previous estimations of the outflow velocity from the amount of reflection in this object (e.g. Beloborodov 1999; Di Salvo et al. 2001; Malzac et al. 2001). This outflow velocity is also in agreement with the jet bulk velocity estimated by Malzac et al. (2009) from measurements of the optical nebula surrounding this X-ray source.

A good solution is found also in the model involving a truncated disk and the

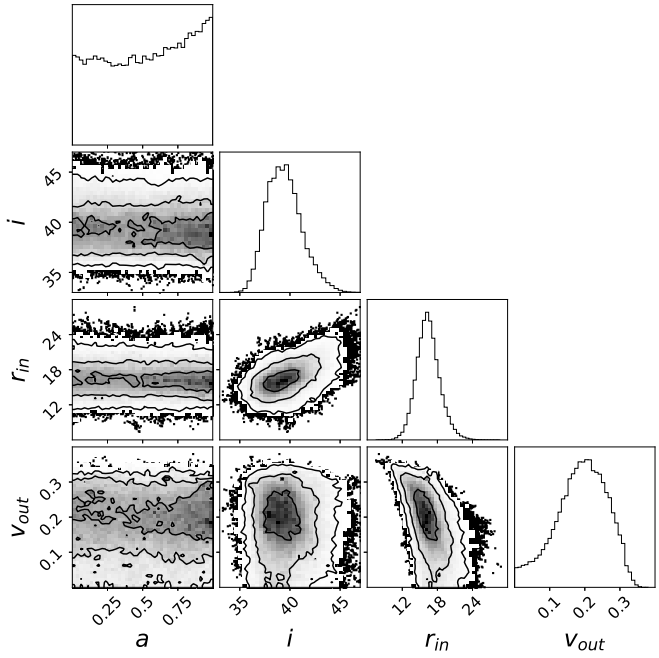

Figure 20: Probability distributions showing correlations between the a, i and $r_{\rm in}$ and β parameters of model 5 (see Table 1) fitted to Cyg X-1, obtained in the MCMC analysis using `xspec_emcee` implemented by Jeremy Sanders. The results of this analysis are presented using package `corner` (Foreman-Mackey 2016). The contours in the 2D plots correspond to the significance of $\sigma = 1, 2, 3$. The histograms show the probability distributions for the individual parameters.

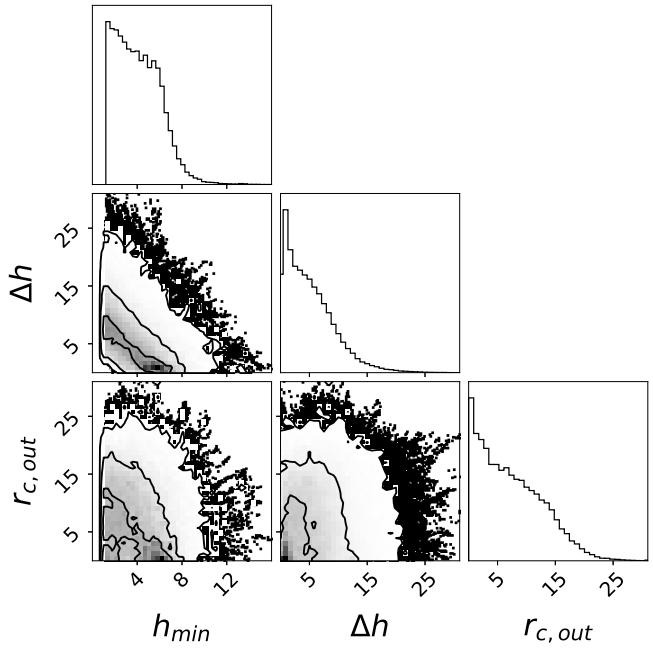

Figure 21: Probability distributions, obtained in the MCMC analysis, showing correlations between the geometrical parameters of the X-ray source in the analysis with model 5 extended by taking into account the size of the source.

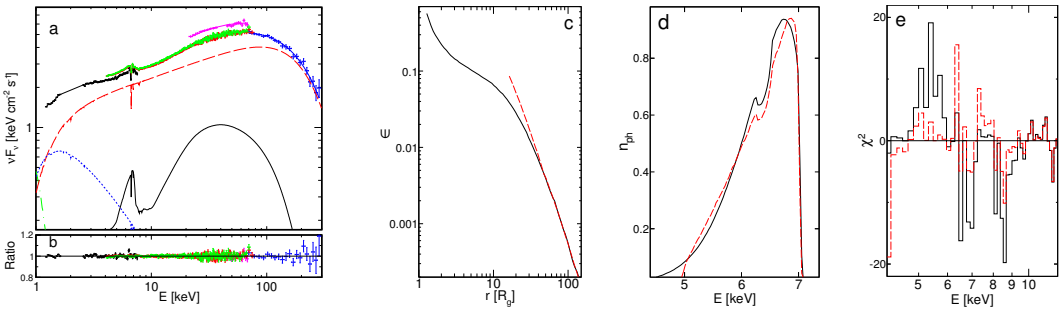

Figure 22: (a) Unfolded data and model spectrum for our model 6, see Table 1. The data points for FPMA, FPMB, XIS1, PIN and GSO are shown in red, green, black, magenta and blue, respectively. The red dashed line shows the Comptonization component of `reflkerrV` and the black solid line shows its reflection. The blue dotted line shows the disk blackbody and the green dot-dashed line shows the soft Comptonization. (b) Fit residuals given as the data-to-model ratio. For models 4 and 5, the model components and the data-to-model ratios are very similar to these shown in (a,b). Panels (c-e) illustrate the difference between model 4 (solid black) and model 6 (red dashed). (c) Radial emissivity profiles of reflection. (d) Profiles of an intrinsically narrow line with the rest-frame energy 6.4 keV, observed at $i = 41°$. (e) Fit residuals given as χ^2 contributions for `NuSTAR`; the FPMA and FPMB data are co-added for clarity of this figure.

source on the opposite side of the disk, partially visible through the optically-thin, central region. We note that the parameters fitted in it closely approximate the geometry of a truncated outer disk irradiated by the inner flow, with the two sources representing the parts of the flow on the opposite sides of the equatorial plane. In particular, in such a geometry the fitted Γ and $T_{\rm e}$ would correspond to the optical half-thickness of the flow of $\tau \sim 0.6$, implying attenuation of radiation from the bottom part of the flow by $\sim 50\%$, consistent with the fitted $\delta_{\rm B}$.

Both fitted models represent a very similar configuration, with the disk truncated at $r_{\rm in}$ and irradiated by the X-rays produced within the central region with a size smaller than $r_{\rm in}$. In both cases, the irradiation profile follows the same form, $\propto r^{-3}$. Then, verification of which of these solutions describes Cyg X-1, which would provide an essential diagnostic of the jet launching region, is not possible based on the shape of the reflected radiation alone. Possibly some more significant constraints could be found by including results of polarimetric measurements and, on the theoretical side, linking the relativistic reflection and the X-ray production models.

We also demonstrated how the lamp-post models fitted with a free normalization of the reflected component are affected when the model with a self-consistent description of the non-isotropy of the X-ray source is applied to explain the reduc-

tion of reflection strength. The related effects are most apparent in models with low h, where strong beaming is needed to counteract the light bending, e.g. in the model for Cyg X-1 of Parker et al. (2015). This model requires $\beta > 0.8$, significantly altering the relativistic blurring, which can be only partially compensated by the change of the model parameters and gives a poor fit formally disfavoring the `eqpair` solution with an outflow. Similarly, the self-consistent inclusion of the non-isotropy instead of the free scaling of reflection in the model with stratified Comptonization gives significantly different parameters, e.g. ξ and A_{Fe} lower by over a factor of 2, and much larger i compared to those reported by Basak et al. (2017).

We conclude that results obtained using the lamp-post model with a free scaling of reflection should be treated with extreme care and considered as nonphysical unless a self-consistent explanation for the reduction of reflection strength is given. Currently, such an explanation is lacking. This reduction can be self-consistently attributed to a non-isotropic emission only if the related change of the spectral shape is taken into account. We directly demonstrated this for the kinematic beaming, but the same is obviously true for any mechanism leading to a non-isotropic emission.

The observed reflection could be also lessened due to the Comptonization of reflection in the X-ray source (e.g. Steiner et al. 2017). This, however, would require the X-ray corona covering a large part of the inner disk, in contradiction to the assumptions of the lamp-post model, which is typically applied assuming a point-like source, representing a very compact corona. Indeed, when models allowing to fit the corona size are applied, it is found that the corona must be very compact, with the size of the order of a gravitational radius for the model of Parker et al. (2015) for Cyg X-1 and similarly for the Seyfert galaxy 1H 0707-495 (Szanecki et al. 2020; and Section 4), and we demonstrated explicitly in Section 2.2 that only a very compact corona can reproduce the results obtained with a point-like lamp post. Such compact coronae intercept a small fraction of reflected photons, making their Comptonization a negligible effect.

4 1H 0707–495

4.1 Introduction

1H 0707–495 ($z = 0.041$) is a NLSy1 and plays a crucial role in our understanding of this class of objects. NLSy1s host lower-mass supermassive black holes (10^6–$10^7 M_\odot$) and often show X-ray properties unique among AGNs, specifically, a very soft hard–X-ray continuum (with $\Gamma \sim 2.5$), a strong, highly variable soft excess emission, and rapid variability on time-scales of hours (e.g. Boller et al. 1996). The origin of the soft excess is unclear. It can be modeled by warm corona models (e.g. Jin et al. 2017), in which there is an optically thick corona with temperature $\lesssim 1$ keV in addition to the optically thin hot corona. This is similar to the warm Comptonization skin models applied in the X-ray binaries (Section 1.7). An alternative explanation of the soft excess is the reflection from the innermost region of the accretion disk (e.g. Crummy et al. 2006), in which the excess is reproduced by a blend of a series of emission lines in the soft X-ray band subject to a strong relativistic blurring.

In 1H 0707–495, the characteristic properties of NLSy1s, i.e. rapid variability and the strength of soft excess, are extreme. 1H 0707–495 gained a particular interest after the discovery of a sharp drop, by a factor of more than 2, in the spectrum at ~ 7 keV, during the first `XMM` observation (Boller et al. 2002). Two models explaining this feature were considered, partial-covering absorption by clouds of neutral material and ionized disk reflection, and both required an iron abundance much larger than solar. The source was then studied in subsequent `XMM` observations with longer exposure times and the measured spectral features and associated timing properties were attributed to the blurred reflection (Fabian et al. 2009; Zoghbi et al. 2010). The spectral variability was found to indicate that the spectrum is composed of at least two components, which are interpreted as a power law dominating in the 1 to 4 keV energy range and a reflection component outside this range. A negative time lag (calculated from the cross spectrum which is constructed from the Fourier transforms of the two light curves in the energy bands under study, following the formalism of Nowak et al. 1999) between the continuum-dominated energy band (1-4 keV) and the soft excess (0.3-1 keV) was revealed, showing that the direct hard emission leads the reflected emissions by ~ 30 s. These lags were interpreted as the

reverberation signal arising from light-travel time between the corona and inner disk, forming evidence that the observed radiation originates within a few gravitational radii of the black hole.

The relativistic reflection interpretation was further explored in a series of works aimed at the estimation of the geometry of the X-ray corona. Wilkins & Fabian (2011) estimated that the observed reflection is consistent with a twice-broken power-law form of the radial emissivity with an extremely steep profile in the inner regions of the disk (with $q_{\rm in} \simeq 8$, Figure 13). Wilkins & Fabian (2012) then claimed that this profile can be explained by an extended region of primary X-ray emission extending outwards to a radius of around $30R_{\rm g}$. This scenario was then applied in Wilkins et al. (2014) who inferred that the X-ray emitting corona expands radially by 30 per cent as the luminosity increases, contracting again as the luminosity decreases. These assessments, however, relied on indirect comparison of theoretical and empirical profiles. They were then critically revised by Szanecki et al. (2020) and the conclusions about a relatively large extent of the corona were found to be highly misguided. A corona extending out to tens of $R_{\rm g}$ gives a relatively weak irradiation of the innermost disk and cannot explain very broad features like those in the reflection model of 1H 0707–495. These issues were discussed in Section 2.2.

NLSy1s are often found to accrete at super-Eddington accretion rates of more than 10 times the Eddington limit (e.g. Jin et al. 2009). For 1H 0707–495, Done & Jin (2016) found an even larger value of ~ 200 times the Eddington limit, based on the observed optical/UV emission and parameters of relativistic reflection models. Such luminous disks should launch strong winds due to continuum radiation pressure (e.g. Ohsuga & Mineshige 2011). Indeed, a variety of nearby Seyfert galaxies, in particular NLSy1s, exhibit blueshifted absorption features above 7 keV, which are interpreted as an ultrafast (with the velocity $v > 10000$ km s^{-1}) outflow of a highly ionized material (e.g. Tombesi et al. 2010). Therefore, spectral properties of these sources may be affected by absorption, emission and scattering in a wind. Absorption has been considered as an alternative to reflection explanation for the observed features (Miller et al. 2008), but the proposed models are complex (with multizone absorption) and often give rather poor fits; e.g. an attempt to apply the wind model of Mizumoto et al. (2019) to 1H 0707–495 in Szanecki et al. (2020) gave a poor fit

despite restriction to only the 2–10 keV band (due to the limitations of the tabulated wind model).

For 1H 0707–495, hints for absorption lines from an ionized outflow were reported by Hagino et al. (2016) and Dauser et al. (2012), and evidence of emission lines from ionized outflow were found in the XMM/RGS spectra by Kosec et al. (2018). Attempts of the spectral description of this source attributed to absorption were then presented by Mizumoto et al. (2014) and Hagino et al. (2016), and they were extended for the description of the X-ray reverberation lags of the Fe K line by Mizumoto et al. (2019). However, no self-consistent model for the full energy range was presented so far. E.g. Mizumoto et al. (2014) describe the absorbers using empirical absorption edge components, while Hagino et al. (2016) and Mizumoto et al. (2019) limited their analysis to the 2–10 keV range.

In our previous work (Szanecki et al. 2020) we found a good description of 1H 0707–495 in the model including both the relativistic reflection and the ionized absorption. However, that analysis was restricted to the 1.1–10 keV range (following Wilkins et al. 2014; which we addressed in our work). Furthermore, we used a very approximate absorption model, in particular, assuming a solar abundance of iron despite finding a super-solar value in the reflection component (this problem, i.e. the use of inconsistent reflection and absorption models, concerns all other published models of this source). Here we extend our analysis by including the full XMM energy range of 0.3–10 keV, and we attempt to include a self-consistent absorption and photoionized emission models.

4.2 Data

We use the same datasets as in Szanecki et al. (2020). We consider 15 XMM observations of 1H 0707–495 between 2000 and 2011 with an exposure time longer than 10 ks, see e.g. table 1 in Hagino et al. (2016). The 15 spectra from the EPIC pn detector (Strüder et al. 2001) were extracted using the XMM-Newton Science Analysis Software (SAS) version 17.0.0, and the Current Calibration File released on 29-Mar-2019. For each observation the data were reduced separately. We applied the standard selection criteria with the PATTERN ≤ 4 condition and excluding periods with the 10–12 keV background rate above 0.4 counts per second. The source

spectra were extracted for a circular region having 60 arcsec in diameter. For the background spectra we have found optimal circular region using the `ebkgreg` tool, which was typically chosen to be a region of about 120 arcsec in diameter. The response files for each spectrum were generated with the `rmfgen` and `arfgen` tools.

The observation performed in January 2011 (Obs. ID 0554710801) caught the source in an extremely low state (Fabian et al. 2012) and is treated separately here; we refer to it as the very low (VL) state. The remaining fourteen observations are used together to build the spectra of three non-overlapping count rate intervals, with < 4, $4 - 6$ and $6 - 10$ counts/s (in the $0.2 - 10$ keV energy range), which we refer to as the low (L), medium (M) and high (H) state, respectively. This selection of flux-resolved spectra is similar to that used in Wilkins et al. (2014) and it is based on the assumption that the state of the X-ray source is determined by the X-ray flux. Spectral differences between these spectra could be then used to verify whether systematic changes of the source geometry correspond to the change of the observed flux.

Light curves of 1H 0707–495 with the time bin equal to 100 s were extracted with the same size of the source and background regions as the spectra and corrected with the `epiclccorr` tool. Using the light curves we created good time intervals (GTI) files for each of the 14 observations, applying the above count rate criteria. The count rate selected spectra were extracted using these GTI files, with appropriate response files. Finally, the spectra for each count rate range were summed with the `epicspeccombine` tool. The resulting spectra have total exposure times of 64.5 (VL), 313.5 (L), 318 (M) and 237.8 (H) ks. Our selection criteria for flux-resolved spectra are the same as those applied in Wilkins et al. (2014).

We consider the 0.3–10 keV range. For spectral binning we use the `specgroup` tool of SAS with the minimal signal-to-noise ratio for each channel set to 5 and the oversample parameter set to 3.

4.3 Model

To describe the reflection component, we apply our `reflkerr_elp` model (Section 2), with geometry shown in Figure 6, i.e. we assume that the corona is located around the symmetry axis and has a cylindrical shape, and we take into account its rotation.

We take into account two versions of the model, denoted as `[r]` and `[x]`, respectively, with rest-frame reflection described by either `reflionx` or `xillverD` (Section 1.6.1). All previous attempts of fitting the reflection spectra to 1H 0707–495, including our in Szanecki et al. (2020), used `reflionx`. On the other hand, García et al. (2016) argue that the density of 10^{15} cm^{-3} may be too low to fit this source and higher values ($\gtrsim 10^{19}$ cm^{-3}) may be relevant (however, their arguments are rather qualitative and they do not present an actual fit to the data in the energy range including the soft excess, for which the issue of density would be most relevant). Therefore, we consider also models `[x]` in which the density of the reflector is a free parameter. We did not use `hreflect` (which is originally applied in `reflkerr` models) because we consider only the data below 10 keV and improvements in the description of the Compton hump are not relevant.

To model warm absorbers, we used the absorption tables calculated with `XSTAR` (Kallman & Bautista 2001). We first used the `zxipcf` model, which was applied also in Szanecki et al. (2020) and gave a good description of the data. However, this model assumes that the ionizing radiation has a spectrum with photon index $\Gamma = 2.2$, which is much harder than the intrinsic spectrum of 1H 0707–495 ($\Gamma \sim 2.6$). Furthermore, `zxipcf` assumes a solar abundance of iron, whereas all spectral models of 1H 0707–495 find significantly super-solar values. We therefore calculated a new model, which we refer to as `warm26`, in which we assume $\Gamma = 2.6$ and use the iron abundance as a free parameter. The model includes the grid of ionization parameters, $-3 \leq \log_{10} \xi \leq 6$, column densities, $5 \times 10^{20} \leq N_{\rm H} \leq 5 \times 10^{24}$ cm^{-2}, and iron abundance $0.5 \leq \mathrm{A_{Fe}} \leq 20$. The blueshift corresponding to an outflow of the absorbing material is taken into account by allowing the redshift parameter in `zxipcf` and `warm26` to fit with negative values. Both `zxipcf` and `warm26` assume also that the absorber covers only some fraction, $f_{\rm cov}$, of the source, while the remaining $(1 - f_{\rm cov})$ of the spectrum is seen directly.

In our models with `zxipcf` we found strong indications of additional components, likely representing emission of a photoionized wind. We first described them using phenomenological gaussian components. However, in our final models we attempted to describe this emission using a self-consistent model. We calculated the emission

tables for $\Gamma = 2.6$ and variable iron abundance using `XSTAR`[7]. We refer to this model as `photem26`. `warm26` and `photem26` describe emission for almost the same plasma except for the turbulent velocity, which is set to $v_{\rm turb} = 200$ km s^{-1} in the former and 6000 km s^{-1} in the latter. A relatively high value of $v_{\rm turb}$ of several thousand km s^{-1} in the emitting material was directly estimated by Kosec et al. (2018), who also assessed that the outflow in 1H 0707–495 is stratified. Then, it is likely represented by a range of ξ and $v_{\rm turb}$[8].

Properties of the `warm26` and `photem26` models, relevant to our fitting results, are discussed in the Appendix.

4.4 Results

We have tested a large number of models and the results concerning the `reflkerr_elp` component appear very stable (e.g. the full dominance of reflection in models `[x]`, geometrical parameters of the corona indicating a very compact source). We present here selected results as models 1, which were the starting point for our analysis strictly following Szanecki et al. (2020), and models 2, which represent the final, most consistent versions found in our investigation.

4.4.1 Models 1

We first tried to extend the model of Szanecki et al. (2020) to the full energy range. We use neutral absorption described by `tbabs` and, following earlier works (Zoghbi et al. 2010, Dauser et al. 2012), we consider an additional black-body component in the soft X-ray range. The primary power-law and reflection components are described with `reflkerr_elp`, which, as described above, is convolved with either `reflionx` (in model `1[r]`) or `xillverD` (in model `1[x]`). We take into account the ionized absorber described with `zxipcf`. We fitted simultaneously the four spectra linking i for all four states. We found that such a version, i.e. `tbabs*zxipcf(reflkerr_elp + bbody)` gives a very poor description of the data. Then, we found a moderate improvement after adding the second `zxipcf` and the Gaussian line at ~ 6.5 keV,

[7] we consulted the author of `XSTAR`, Timothy Kallman, for setting of this code parameters optimal for our purpose

[8] obviously it would be optimal to construct a model spanning a full range of relevant parameters, including a range of $v_{\rm turb}$ and Γ as well as abundances of elements other then iron. However, such a task is not feasible. Computation of `warm26` and `photem26` took over two months.

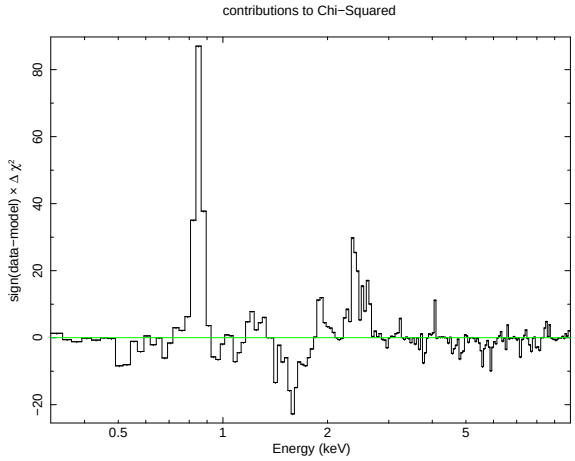

Figure 23: The fit residuals for spectrum M given as χ^2 contributions in a model similar to `1[x]` in Table 3, but refitted after neglecting the $\texttt{gaussian}_1$ component.

and a huge improvement after adding another Gaussian at ~ 0.9 keV. An example of residuals in the model fitted without this last component is shown in Figure 23. Apart from an obvious feature at 0.8–0.9 keV, we also see residuals in the 1–3 keV range, which are significantly reduced in the model including the second Gaussian thanks to the change of ξ and Γ. The definition of our final models and the fitting results are given in Tables 2 and 3 and the fitted spectra with contributions of the Gaussian and black-body components are shown in Figure 24. In models 1 we closely followed Szanecki et al. (2020) and we allowed $A_{\rm Fe}$ to fit independently in each state, we fixed $h_{\rm min} = 0$ in VL, $h_{\rm min} = r_{\rm hor}$ in L, M and H, $a = 0.998$, and the angular velocity $\Omega = \Omega_{\rm K}$ (i.e. rotation of the corona with Keplerian angular velocity; see Section 2.3 for details).

The fitted neutral column density in `tbabs`, $\simeq (7-8) \times 10^{20}$ cm^{-2}, is larger than Galactic (4.6×10^{20} cm^{-2}, see discussion in Dauser et al. 2012) and in agreement with values obtained by Dauser et al. (2012) and Kosec et al. (2018). The `bbody` component does not improve the fit to the VL spectrum in either version of the model and therefore it is neglected (for VL). For L, M and H spectra, the `bbody` component slightly improves (by $\Delta\chi^2 = -43$ for 6 parameters; two free parameters for each state) the fit only in model `1[r]`, where its flux gives a $\simeq (20-30)\%$ contribution at ~ 0.5 keV. This moderate contribution agrees with the results reported by Zoghbi et al. (2010) and Dauser et al. (2012), who also used the blurred `reflionx` reflection.

For model `1[x]`, the `bbody` component does not improve the fit and its contribution is constrained to at most 10%.

Properties of the `zxipcf` components are briefly discussed in the Appendix. The lower-$N_{\rm H}$ one, referred to as $\texttt{zxipcf}_2$, improves the fit by $\Delta\chi^2 = -73$ in model `1[r]` and by $\Delta\chi^2 = -109$ in model `1[x]` for 16 free parameters. It represents a highly ionized absorber outflowing at $\sim (30000 - 50000)$ km s^{-1}, which is consistent with the velocity of absorber reported in Dauser et al. (2012) and Kosec et al. (2018). The larger higher-$N_{\rm H}$ absorber, referred to as $\texttt{zxipcf}_1$, is crucial for obtaining any reasonable agreement with the observed spectra in our spectral setup especially in model `1[x]`, as without it the model spectra do not have a sufficient curvature. In the VL state the `zxipcf` components describe a virtually neutral absorber.

The line fitted at $\simeq 6.5$ keV, referred to as $\texttt{gaussian}_2$, represents a blueshifted Fe Kα emission. We do not find any indication of its presence in spectrum VL. It improves the fits by $\Delta\chi^2 = -62$ in model `1[r]` and by -91 in model `1[x]` for 9 free parameters. In our fitting procedure, the width of this line was constrained to $\sigma \leq 0.15$ keV, which corresponds to a Doppler broadening with $\lesssim 7000$ km/s. The $\texttt{gaussian}_1$ at ~ 0.9 keV is critical for the spectral model, improving the fits by $\Delta\chi^2 = -820$ in model `1[r]` and by -794 in model `1[x]` for 12 free parameters. It is fitted with almost the same peak energy in all spectra. As discussed in the Appendix, we presume that this component represents the blend of Fe lines in the 0.7–1 keV range predicted by photoionized emission models for $\xi = 100 - 1000$ and we checked that indeed at the spectral resolution of `EPIC pn` the blend of these lines may be represented by a single broad line component. A single Gaussian approximating the Fe XVII–XIX blend has a width $\sigma \lesssim 0.07$ keV and we used this constraint in our spectral modeling.

In `reflkerr_elp` we assumed that the corona rotates with the Keplerian angular velocity (within the ISCO, we assume the rigid rotation with the angular velocity at the ISCO), but we allowed the scaling parameter of reflection, $\mathcal{R}$, to vary. Interestingly, $\mathcal{R}$ is fitted with the physical value of $\mathcal{R} \sim 1$ in all cases except for model `1[r]` for H, but also in this case the physical solution is within the 3σ uncertainty of the best fit.

We allowed $r_{\rm in}$ to vary in all our models. We found a hint that the disk must

Table 2: Fitting results with model `1[r]` (with `reflionx`) to 1H 0707–495.
VL: `tbabs*zxipcf*zxipcf(gaussian + reflkerr_elp)`.
L,M,H: `tbabs*zxipcf*zxipcf(bbody + gaussian + gaussian + reflkerr_elp)`

	VL	L	M	H
		`tbabs`		
$N_{\rm H}$	$0.094^{+0.021}_{-0.014}$	$0.067^{+0.005}_{-0.005}$	$0.078^{+0.005}_{-0.006}$	$0.082^{+0.002}_{-0.002}$
		$\texttt{zxipcf}_1$		
$N_{\rm H}$	$12.8^{+1.4}_{-1.2}$	$144.0^{+59.0}_{-72.0}$	$143.0^{+47.0}_{-32.0}$	$72.0^{+85.0}_{-58.0}$
$\log_{10}(\xi)$	$1.1^{+0.1}_{-0.3}$	$3.8^{+0.2}_{-0.3}$	$3.2^{+0.4}_{-0.1}$	$4.1^{+0.1}_{-0.1}$
$f_{\rm cov}$	$0.94^{+0.01}_{-0.01}$	$1.00^{+0}_{-0.19}$	$0.63^{+0.06}_{-0.19}$	$1.00^{+0}_{-0.27}$
z	$0.04^{+0}_{-0.09}$	$-0.09^{+0.01}_{-0.01}$	$-0.06^{+0.01}_{-0.01}$	$-0.07^{+0.01}_{-0.01}$
		$\texttt{zxipcf}_2$		
$N_{\rm H}$	$0.3^{+0.2}_{-0.1}$	$3.8^{+1.2}_{-0.7}$	$4.7^{+4.4}_{-2.2}$	$2.5^{+3.7}_{-1.5}$
$\log_{10}(\xi)$	$0.1^{+0.2}_{-0.1}$	$3.5^{+0.4}_{-0.2}$	$3.4^{+0.1}_{-0.1}$	$3.4^{+0.1}_{-0.1}$
$f_{\rm cov}$	$1.00^{+0}_{-0.10}$	$0.50^{+0.10}_{-0.10}$	$1.00^{+0}_{-0.30}$	$1.00^{+0}_{-0.10}$
z	$-0.08^{+0.02}_{-0.03}$	$-0.13^{+0.02}_{-0.02}$	$-0.11^{+0.01}_{-0.01}$	$-0.15^{+0.01}_{-0.01}$
		`bbody`		
$kT_{\rm bb}$ [keV]	-	$0.11^{+0.01}_{-0.01}$	$0.10^{+0.01}_{-0.01}$	$0.11^{+0.01}_{-0.01}$
norm ($\times 10^{-5}$)	-	$4.4^{+1.0}_{-1.0}$	$6.7^{+1.3}_{-1.8}$	$6.4^{+1.1}_{-1.2}$
		$\texttt{gaussian}_1$		
E [keV]	$0.85^{+0.04}_{-0.05}$	$0.89^{+0.01}_{-0.01}$	$0.88^{+0.01}_{-0.01}$	$0.87^{+0.01}_{-0.01}$
σ [keV]	$0.04^{+0.03}_{-0.03}$	$0.05^{+0.01}_{-0.01}$	$0.06^{+0.01}_{-0.01}$	$0.07^{+0}_{-0.01}$
norm ($\times 10^{-4}$)	$8.5^{+4.6}_{-3.8}$	$1.1^{+0.2}_{-0.2}$	$2.5^{+0.6}_{-0.4}$	$2.5^{+0.1}_{-0.3}$
		$\texttt{gaussian}_2$		
E [keV]	-	$6.40^{+0.11}_{-0.09}$	$6.68^{+0.02}_{-0.08}$	$6.54^{+0.08}_{-0.08}$
σ [keV]	-	$0.15^{+0}_{-0.04}$	$0.15^{+0}_{-0.05}$	$0.15^{+0}_{-0.03}$
norm ($\times 10^{-6}$)	-	$1.0^{+0.3}_{-0.3}$	$1.3^{+0.4}_{-0.4}$	$1.9^{+0.3}_{-0.6}$
		`reflkerr_elp`		
$r_{\rm c,out}$	$1.32^{+0.37}_{-0.10}$	$0.10^{+0.79}_{-0}$	$0.10^{+0.57}_{-0}$	$1.49^{+0.07}_{-0.06}$
$h_{\rm max}$	$2.26^{+0.30}_{-0.46}$	$2.57^{+0.78}_{-0.50}$	$2.30^{+0.14}_{-0.10}$	$2.32^{+0.30}_{-0.22}$
$r_{\rm in}$	$1.91^{+0.22}_{-0.18}$	$1.84^{+0.12}_{-0.13}$	$1.39^{+0.04}_{-0.06}$	$1.32^{+0.02}_{-0.09}$
$i^{(a)}$ [°]		$43.5^{+0.5}_{-0.3}$		
Γ	$3.13^{+0.10}_{-0.11}$	$2.58^{+0.06}_{-0.10}$	$2.68^{+0.02}_{-0.03}$	$2.81^{+0.02}_{-0.02}$
$\rm A_{Fe}^{(b)}$	$20.0^{+0}_{-4.5}$	$13.1^{+4.1}_{-1.4}$	$18.9^{+1.1}_{-5.2}$	$20.0^{+0}_{-2.1}$
$\log_{10}(\xi)$	$3.7^{+0.2}_{-0.2}$	$3.3^{+0.1}_{-0.1}$	$3.4^{+0.1}_{-0.1}$	$3.5^{+0.1}_{-0.1}$
$\mathcal{R}$	$1.1^{+2.3}_{-0.3}$	$1.4^{+1.0}_{-0.2}$	$1.4^{+0.7}_{-0.2}$	$0.2^{+0.1}_{-0.1}$
norm ($\times 10^{-4}$)	$3.6^{+2.2}_{-0.9}$	$3.2^{+0.4}_{-0.7}$	$7.5^{+0.7}_{-2.0}$	$14.1^{+0.5}_{-0.7}$
χ^2/DoF		662/546		
χ^2	112	188	181	181

Notes: (a) linked for all four spectra; (b) $\rm A_{Fe} = 20$ is the maximum value in `reflionx`. All column densities, $N_{\rm H}$, are given in the unit of $[10^{22}]$ cm^{-2}. $r_{\rm c,out}$, $h_{\rm max}$, and $r_{\rm in}$ are in the unit of $[R_{\rm g}]$.

Table 3: Fitting results with model `1[x]` (using `xillverD`) to 1H 0707–495. The model definitions and setting of the model parameters is the same as in Table 2.

	VL	L	M	H
		`tbabs`		
$N_{\rm H}$	$0.077^{+0.013}_{-0.011}$	$0.073^{+0.004}_{-0.003}$	$0.080^{+0.001}_{-0.001}$	$0.080^{+0.002}_{-0.003}$
		`zxipcf`$_1$		
$N_{\rm H}$	$14.2^{+1.2}_{-1.3}$	117^{+14}_{-23}	134^{+16}_{-16}	145^{+7}_{-13}
$\log_{10}(\xi)$	$1.1^{+0.1}_{-0.2}$	$2.5^{+0.5}_{-0.1}$	$2.9^{+0.1}_{-0.1}$	$3.1^{+0.1}_{-0.2}$
$f_{\rm cov}$	$0.98^{+0.01}_{-0.03}$	$0.70^{+0.10}_{-0.10}$	$0.60^{+0.10}_{-0.10}$	$0.64^{+0.04}_{-0.04}$
z	$0.04^{+0}_{-0.02}$	$-0.00^{+0.01}_{-0.01}$	$-0.02^{+0.01}_{-0.01}$	$-0.03^{+0.01}_{-0.01}$
		`zxipcf`$_2$		
$N_{\rm H}$	$0.3^{+0.1}_{-0.1}$	97^{+37}_{-37}	65^{+8}_{-34}	65^{+6}_{-4}
$\log_{10}(\xi)$	$0.1^{+0.2}_{-0.3}$	$3.5^{+0.4}_{-0.2}$	$3.4^{+0.2}_{-0.1}$	$3.5^{+0.1}_{-0.1}$
$f_{\rm cov}$	$1.00^{+0}_{-0.27}$	$0.88^{+0.12}_{-0.14}$	$0.81^{+0.05}_{-0.05}$	$0.80^{+0.06}_{-0.05}$
z	$-0.07^{+0.03}_{-0.03}$	$-0.09^{+0.01}_{-0.01}$	$-0.10^{+0.01}_{-0.01}$	$-0.13^{+0.01}_{-0.01}$
		`bbody`		
$kT_{\rm bb}$ [keV]	-	$0.11^{+0.01}_{-0.01}$	< 0.12	< 0.12
norm ($\times 10^{-5}$)	-	$4.5^{+0.5}_{-1.9}$	< 4.9	< 6.2
		`gaussian`$_1$		
E [keV]	$0.84^{+0.05}_{-0.05}$	$0.86^{+0.01}_{-0.01}$	$0.86^{+0.01}_{-0.01}$	$0.88^{+0.01}_{-0.01}$
σ [keV]	$0.06^{+0.01}_{-0.04}$	$0.07^{+0}_{-0.01}$	$0.07^{+0}_{-0.01}$	$0.07^{+0}_{-0.01}$
norm ($\times 10^{-4}$)	27^{+35}_{-22}	$6.9^{+1.1}_{-1.1}$	$6.5^{+0.1}_{-0.4}$	$5.5^{+0.2}_{-1.3}$
		`gaussian`$_2$		
E [keV]	-	$6.48^{+0.07}_{-0.07}$	$6.70^{+0.04}_{-0.04}$	$6.74^{+0.05}_{-0.10}$
σ [keV]	-	$0.15^{+0p}_{-0.03}$	$0.12^{+0.03}_{-0.05}$	$0.15^{+0}_{-0.01}$
norm ($\times 10^{-6}$)	-	$2.4^{+0.7}_{-0.7}$	$2.3^{+0.6}_{-0.6}$	$3.0^{+0.6}_{-0.7}$
		`reflkerr_elp`		
$r_{\rm c,out}$	$1.85^{+0.32}_{-0.73}$	$0.19^{+0.72}_{-0.09}$	$0.11^{+0.35}_{-0.01}$	$0.21^{+0.45}_{-0.11}$
$h_{\rm max}$	$1.99^{+0.56}_{-1.19}$	$1.55^{+0.07}_{-0.16}$	$1.64^{+0.09}_{-0.03}$	$1.86^{+0.13}_{-0.03}$
$r_{\rm in}$	$1.99^{+0.30}_{-0.34}$	$1.32^{+0.04}_{-0.05}$	$1.32^{+0.02}_{-0.03}$	$1.32^{+0.02}_{-0.02}$
$i^{(a)}$ [°]		$40.5^{+1.5}_{-0.9}$		
$\Gamma^{(b)}$	$3.40^{+0}_{-0.16}$	$2.54^{+0.02}_{-0.12}$	$2.68^{+0.01}_{-0.09}$	$2.76^{+0.01}_{-0.02}$
$\rm A_{Fe}^{(c)}$	$10^{+0}_{-2.0}$	$10^{+0}_{-0.8}$	$10^{+0}_{-0.2}$	$10^{+0}_{-0.1}$
$\log_{10}(\xi)$	$4.0^{+0.1}_{-0.2}$	$3.3^{+0.1}_{-0.2}$	$3.5^{+0.1}_{-0.1}$	$3.7^{+0.1}_{-0.1}$
$\log_{10}(n_{\rm e})$	$17.0^{+0.1}_{-0.2}$	$18.1^{+0.4}_{-0.1}$	$17.4^{+0.5}_{-0.1}$	$17.8^{+0.6}_{-0.1}$
$\mathcal{R}$	$1.5^{+\infty}_{-0.8}$	$1.1^{+3.4}_{-0.9}$	$1.1^{+1.6}_{-0.3}$	$1.0^{+0.2}_{-0.1}$
norm ($\times 10^{-4}$)	$1.4^{+3.1}_{-0.8}$	$2.9^{+7.1}_{-1.0}$	$5.1^{+8.9}_{-0.3}$	$9.9^{+1.5}_{-0.7}$
χ^2/DoF		727/542		
χ^2	114	199	192	222

Notes: (a) linked for all four spectra; (b) $\Gamma = 3.4$ is the maximum value of Γ in `xillverD`; (c) $\rm A_{Fe} = 10$ is (oficially; see the note for Table 5) the maximum value in `xillverD`. All the parameters units are the same as in Table 2.

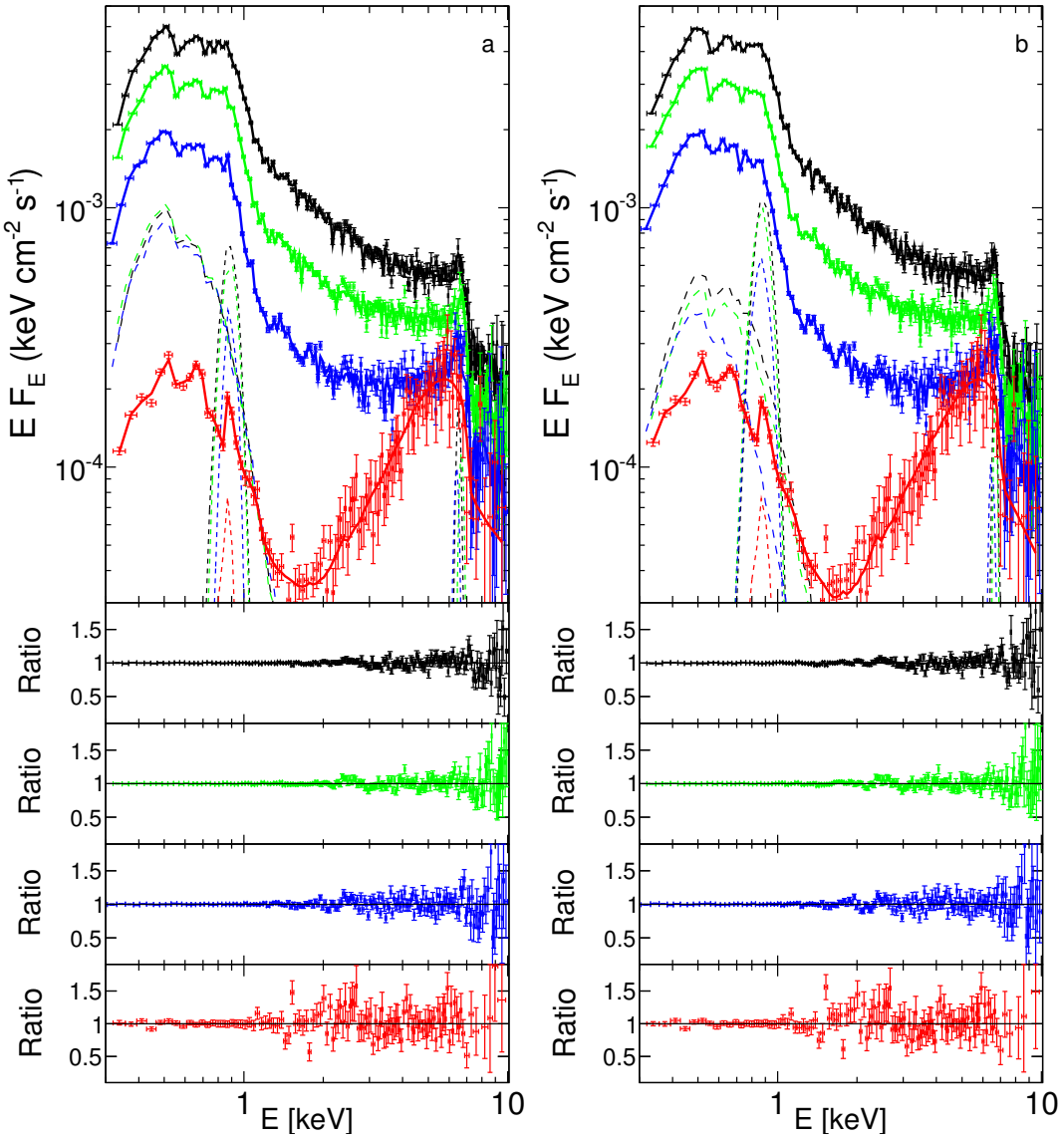

Figure 24: The upper panels show the unfolded data and model spectra for our best-fitted model (a) 1[r] and (b) 1[x] for VL (red), L (blue), M (green) and H (black). The model parameters are given in Tables 2 and 3, respectively. The total models are shown by the solid curve, the blackbody and Gaussian components are shown by the dashed and dotted curves, respectively. The lower panel shows the fit residuals given as the data-to-model ratio for VL, L, M, and H from bottom to top.

be truncated at a very small $r_{\rm in} \simeq 2$ in VL. Then, in model `1[r]` we find $r_{\rm in}$ progressively approaching $r = 1.32$ with the increasing X-ray flux, whereas in model `1[x]` the inner radius is tightly constrained in L, M and H at $r_{\rm in} \simeq 1.32$ (see also Figure 25). This value corresponds to $a \simeq 0.996$ if $r_{\rm in} = r_{\rm ISCO}$.

`xillverD` used in model `1[x]` allows to fit the density of the disk. We found $n_{\rm e} = 10^{17}\,{\rm cm}^{-3}$ in VL, and $n_{\rm e} \sim 10^{18}\,{\rm cm}^{-3}$ in higher states, which values are much larger than $n_{\rm e} = 10^{15}\,{\rm cm}^{-3}$ assumed in `reflionx`.

Figure 25 shows the probability distribution and correlation plots for the fitted parameters of `reflkerr_elp`. The parameters are tightly constrained, especially in model `1[x]`, and no obvious systematic trends are seen in the geometric parameters of the corona. On the other hand, we note systematic trends in Γ and ionization of the disk, which then likely determine the intrinsic spectral variability of 1H 0707–495.

4.4.2 Models 2

We now attempt to use the most self-consistent model possible, building it on the results presented in Section 4.4.1. We take into account the same spectral components, i.e. the neutral absorber, black-body emission, two ionized absorbers, photoionized emission and the intrinsic power-law emission and its reflection. However, the photoionized emission is now described with the physical model, `photem26`, and the ionized absorbers are described with `warm26` (more appropriate for 1H 0707–495 than `zxipcf`). The remaining components are described in the same manner as in Section 4.3.1. We also link the iron abundance across the four states for all relevant components, i.e. `warm26`, `photem26`, and `reflkerr_elp`. In `reflkerr_elp` we now use the physical normalization of the reflected component, i.e. we set $\mathcal{R} = 1$, however, we use the angular velocity of the corona as a free parameter. The definition of the models, referred to as model `2[r]` (in version using `reflionx`) and `2[x]` (in version using `xillverD`), and the fitting results are given in Tables 4 and 5 and the fitted spectra with contributions of `photem26` are shown in Figure 28.

The fits quality in models 2, $\chi^2/{\rm DoF} \simeq 1.4$, is notably worse than in models 1, $\chi^2/{\rm DoF} \simeq 1.2$. The worsening is mostly due to linking $A_{\rm Fe}$ in all components and using `photem26` instead of the Gaussian lines. In particular, `photem26` was calculated

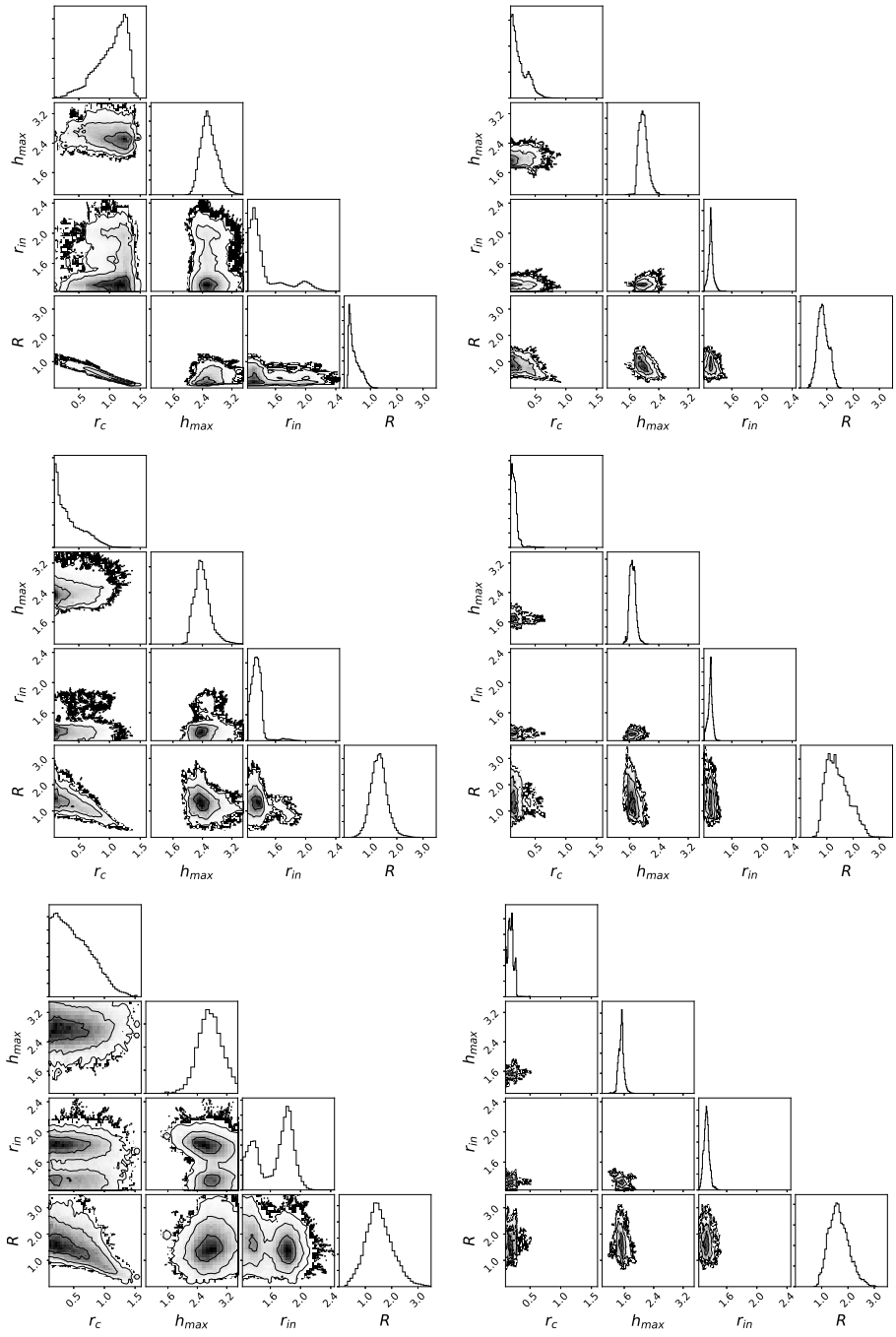

Figure 25: Probability distributions, obtained using the MCMC method, showing correlations between the $r_{\rm in}$, $r_{\rm c,out}$, $h_{\rm max}$ and $\mathcal{R}$ parameters of model `1[r]` (left column) and `1[x]` (right column) models, see Table 2 and 3, respectively, fitted in the 0.3–10 keV range to the H (top), M (middle) and L (bottom) spectrum. The parameter ranges in all panels are the same to allow for an easy comparison of parameter distributions obtained in the two models and to give a clear visualisation of the (lack of) evolution of parameters in different states.

for a fixed slope of ionizing continuum, $\Gamma = 2.6$, whereas the intrinsic emission of 1H 0707–495 exhibits clear, systematic changes around this value. Given that the intensity of the Fe Kα line predicted by the photoionization emission models is extremely sensitive to the value of Γ (see Appendix), it is not surprising that models 1, with a free normalization of the Gaussian at ~ 6.5 keV, give a better match to the data.

We note, however, that the spectra binned using the dedicated `XMM` software have a large number of counts in each bin, which then results in the relatively large value of χ^2 (we noted this in Szanecki et al. 2020). The other works on 1H 0707–495 typically used spectra binned using the `grppha` tool of the `HEASOFT` package. Using such spectra (binned using `grppha` with the condition of at least 25 counts in spectral bin) we get $\chi^2/\mathrm{DoF} \simeq 1.06$ in model `2[r]` and model $\chi^2/\mathrm{DoF} \simeq 1.08$ in model `2[x]`.

The `photem26` components were fitted with $\log_{10}\xi \sim 2.8$, at which the emitted spectrum indeed resembles the empirical Gaussian lines inferred with model 1, see Figure 39. The absorbers described by `warm26` in models 2 have either a larger ξ or smaller N_H than `zxipcf` in models 1, which compensates the larger values of $\mathrm{A_{Fe}}$ and Γ in the former model (see Appendix). The lower values of N_H actually mean that the model is more consistent, as the absorbers described by `zxipcf` were fitted with N_H above 10^{24} cm^{-2} in models 1, which implies the Thomson depth $\tau \sim 1$, whereas the models generated with XSTAR neglect the electron scattering. On the other hand, the absorbers described by `warm26` have $\tau \lesssim 0.3$, so the electron scattering is relatively unimportant. The overall effect of the ionized absorption is very different in model `2[r]`, see Figure 26, and model `2[x]`, see Figure 27, except for the VL state, where in both models it gives a similar, strong absorption of the whole continuum, reproducing the observed spectral inflection. The `warm26` components fitted to spectra L, M and H in model `2[x]` strongly absorb the continuum and significantly contribute to reproducing the shape of the feature at ~ 6 keV. In contrast, in model `2[r]` the `warm26` absorbers shape the L, M and H spectra mostly by imprinting narrow absorption features, with some minor, and decreasing with X-ray flux, continuum absorption.

We initially fixed the inner radius of the disk at the ISCO, this version is reported

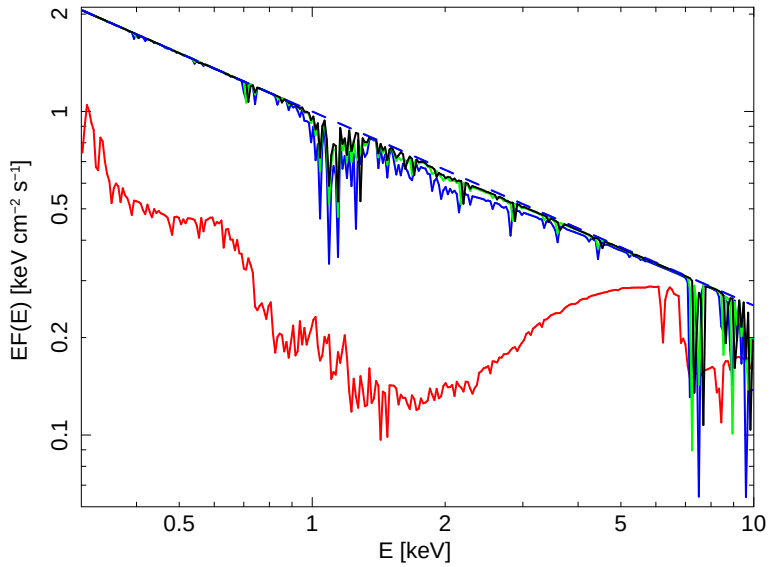

Figure 26: The combined effect of both ionized absorbers, `warm26`$_1$ and `warm26`$_2$, fitted in model `2[r]` (Table 4), acting on the same power-law spectrum with $\Gamma = 2.6$ shown by the dashed blue line. The color coding for reflection spectra is the same as in Figure 24, i.e. VL(red), L (blue), M (green) and H (black).

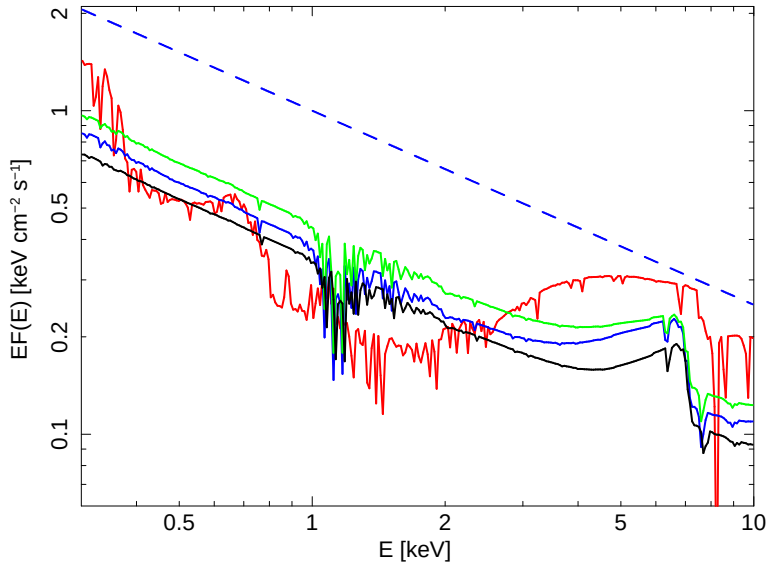

Figure 27: The combined effect of both ionized absorbers, `warm26`$_1$ and `warm26`$_2$, fitted in model `2[x]` (Table 5), acting on the same power-law spectrum with $\Gamma = 2.6$ shown by the dashed blue line. The color coding for reflection spectra is the same as in Figure 28, i.e. VL(red), L (blue), M (green) and H (black).

in Tables 4 and 5. Then we allowed $r_{\rm in}$ to vary and the inner radius was fitted at $r_{\rm in} = 2.26^{+0.29}_{-0.35}$ (VL), $1.31^{+0.05}_{-0.02}$ (L), $1.25^{+0.01}_{-0.02}$ (M), and $1.24^{+0.01}_{-0.01}$ (H) in model `2[r]`, and at $r_{\rm in} = 1.96^{+0.09}_{-0.11}$ (VL), $2.58^{+0.25}_{-0.28}$ (L), $1.32^{+0.18}_{-0.07}$ (M), and $1.33^{+0.08}_{-0.10}$ (H) in model `2[x]`, without a significant improvement of the fit. In either version of the model we find a rapid rotation of the black hole, see Figures 29 and 30. The angular velocity parameter is given in the unit of the Keplerian velocity and it is fitted at $\simeq 1$ in all cases except for model `1[r]` for spectrum H (in which the Keplerian rotation is within the 1σ uncertainty of the best fit).

The disk density was fitted in model `2[x]` at the upper limit of the `xillverD` model, i.e. $n_{\rm e} = 10^{19}\,{\rm cm}^{-3}$. We replaced `reflkerr_elp` in model `2[x]` with the newest version 2.3 of `relxilllpCp` model, in which the reflection spectra are tabulated for $n_{\rm e}$ up to $10^{20}\,{\rm cm}^{-3}$. In spectra M and H, $n_{\rm e}$ was fitted at the upper limit of $10^{20}\,{\rm cm}^{-3}$, however, it did not improve the fit (in the fit we allowed $\mathcal{R}$ to fit freely and we note that the point-like source assumed in `relxilllpCp` gives a good match for a corona with parameters fitted in our model `2[x]`). We also note that the public model `reflionxHD`, which includes reflection spectra for $n_{\rm e}$ exceeding $10^{20}\,{\rm cm}^{-3}$, is tabulated only for $\Gamma \leq 2.3$, and cannot be applied to 1H 0707–495.

Figure 31 shows the probability distribution and correlation plots for the fitted parameters of `reflkerr_elp`. In the version of the model reported here, we introduced an additional parameter for the corona geometry, $r_{\rm c,in}$, and we assume that the corona is empty inside it (i.e. the corona may have a ring-like shape now). For spectrum L we find a corona covering the innermost disk rather than forming a compact source on the symmetry axis, which is then markedly different than for other spectra. It is not clear whether this result is incidental or represents the actual change of geometry, because we do not see a systematic trend in the geometric parameters which would support such a change.

On the other hand, we again note systematic trends in Γ and ionization of the disk, which appear to determine the intrinsic spectral variability of 1H 0707–495.

4.4.3 Alternative model: double reflection

The XMM spectrum of 1H 0707–495 was previously described with the model including two reflection components subject to the same relativistic blurring but with

Table 4: Fitting results with model `2[r]` (using `reflionx`) to 1H 0707–495. In all cases `tbabs(photem26+warm26*warm26(reflkerr_elp + bbody))` and $r_{\rm in} = r_{\rm ISCO}$.

	VL	L	M	H
		`tbabs`		
$N_{\rm H}$	$0.081^{+0.009}_{-0.014}$	$0.059^{+0.002}_{-0.001}$	$0.074^{+0.002}_{-0.002}$	$0.082^{+0.003}_{-0.001}$
		`photem26`		
$\log_{10}(\xi)$	$2.2^{+0.4}_{-0.1}$	$2.7^{+0.1}_{-0.6}$	$2.7^{+0.2}_{-0.1}$	$2.8^{+0.1}_{-0.2}$
z	$-0.05^{+0.03}_{-0.02}$	$0.01^{+0.01}_{-0.05}$	$0.01^{+0.02}_{-0.02}$	$0.01^{+0.01}_{-0.02}$
norm	$0.06^{+0.06}_{-0.01}$	$0.27^{+0.08}_{-0.08}$	$0.55^{+0.18}_{-0.08}$	$0.96^{+0.19}_{-0.26}$
		`warm26`$_1$		
$N_{\rm H}$	$0.4^{+0.8}_{-0.3}$	$0.2^{+0.1}_{-0.1}$	$0.1^{+0.1}_{-0.1}$	$0.1^{+0.1}_{-0.1}$
$\log_{10}(\xi)$	$4.0^{+0.3}_{-0.4}$	$3.5^{+0.1}_{-0.1}$	$3.6^{+0.1}_{-0.1}$	$3.6^{+0.1}_{-0.1}$
$f_{\rm cov}$	$1.00^{+0}_{-0.69}$	$1.00^{+0}_{-0.24}$	$1.00^{+0}_{-0.04}$	$1.00^{+0}_{-0.03}$
z	$-0.21^{+0.03}_{-0}$	$-0.12^{+0.01}_{-0.01}$	$-0.12^{+0.01}_{-0.01}$	$-0.12^{+0.01}_{-0.01}$
		`warm26`$_2$		
$N_{\rm H}$	$5.7^{+0.9}_{-1.0}$	$87.7^{+14.1}_{-41.2}$	$47.6^{+31.8}_{-16.3}$	$47.6^{+30.4}_{-17.7}$
$\log_{10}(\xi)$	$2.8^{+0.1}_{-0.1}$	$6.0^{+0}_{-0.2}$	$6.0^{+0}_{-0.2}$	$6.0^{+0}_{-0.2}$
$f_{\rm cov}$	$0.84^{+0.04}_{-0.02}$	$1.00^{+0}_{-0.12}$	$1.00^{+0}_{-0.17}$	$1.00^{+0}_{-0.14}$
z	$0.04^{+0}_{-0.01}$	$-0.07^{+0.01}_{-0.01}$	$-0.08^{+0.01}_{-0.01}$	$-0.09^{+0.01}_{-0.02}$
		`bbody`		
$kT_{\rm bb}$ [keV]	$0.08^{+0.01}_{-0}$	$0.11^{+0.01}_{-0.01}$	$0.10^{+0.01}_{-0.01}$	$0.10^{+0.01}_{-0.01}$
norm ($\times 10^{-5}$)	$2.9^{+1.4}_{-0.9}$	$6.0^{+0.2}_{-0.1}$	$8.0^{+0}_{-0.2}$	$8.0^{+0}_{-0.3}$
		`reflkerr_elp`		
$a^{(a)}$		$0.990^{+0.008}_{-0.010}$		
$r_{\rm c,in}$	$0.55^{+1.04}_{-0.40}$	$1.56^{+1.99}_{-1.08}$	$0.29^{+0.27}_{-0.19}$	$0.38^{+0.61}_{-0.28}$
$r_{\rm c,out}$	$1.69^{+1.82}_{-0.83}$	$5.48^{+1.68}_{-2.00}$	$0.70^{+0.35}_{-0.23}$	$1.21^{+0.82}_{-0.78}$
$h_{\rm max}$	$2.52^{+0.82}_{-0.86}$	$2.90^{+1.75}_{-1.25}$	$4.04^{+0.36}_{-0.33}$	$4.01^{+0.35}_{-0.44}$
$\Omega_{\rm K}$	$0.83^{+0.56}_{-0.55}$	$0.90^{+0.17}_{-0.21}$	$0.98^{+0.52}_{-0.34}$	$0.42^{+0.48}_{-0.19}$
$i^{(a)}$ [°]		$39.6^{+0.5}_{-0.5}$		
Γ	$2.10^{+0.12}_{-0.08}$	$2.37^{+0.01}_{-0.02}$	$2.65^{+0.01}_{-0.01}$	$2.77^{+0.01}_{-0.01}$
$A_{\rm Fe}^{(a,b)}$		$16.6^{+1.2}_{-0.9}$		
$\log_{10}(\xi)$	$3.0^{+0.1}_{-0.1}$	$3.1^{+0.1}_{-0.1}$	$3.3^{+0.1}_{-0.1}$	$3.4^{+0.1}_{-0.1}$
norm ($\times 10^{-4}$)	$0.7^{+1.0}_{-0.2}$	$2.6^{+0.1}_{-0.1}$	$6.4^{+0.2}_{-0.2}$	$13.0^{+0.5}_{-0.4}$
χ^2/DoF		755/554		
χ^2	114	214	188	239

Notes: (a) linked for all four spectra. (b) $A_{\rm Fe}$ is additionally linked for `reflkerr_elp`, `warm26` and `photem26`. All the parameters units are the same as in Table 2.

Table 5: Fitting results with model `2[x]` (using `xillverD`) to 1H 0707–495. The model definitions and setting of the model parameters is the same as in Table 4.

	VL	L	M	H
		`tbabs`		
$N_{\rm H}$	$0.079^{+0.011}_{-0.020}$	$0.065^{+0.005}_{-0.004}$	$0.069^{+0.002}_{-0.001}$	$0.072^{+0.001}_{-0.002}$
		`photem26`		
$\log_{10}(\xi)$	$2.6^{+0.3}_{-0.3}$	$2.9^{+0.1}_{-0.1}$	$2.9^{+0.1}_{-0.1}$	$2.7^{+0.2}_{-0.1}$
z	$-0.03^{+0.03}_{-0.03}$	$0.03^{+0.01}_{-0.01}$	$0.03^{+0.01}_{-0.01}$	$0.01^{+0.01}_{-0.01}$
norm	$0.07^{+0.05}_{-0.03}$	$0.46^{+0.09}_{-0.06}$	$0.87^{+0.13}_{-0.04}$	$0.63^{+0.20}_{-0.05}$
		`warm26`$_1$		
$N_{\rm H}$	$2.6^{+1.7}_{-0.3}$	$35.2^{+7.0}_{-3.5}$	$36.6^{+3.4}_{-9.1}$	$56.8^{+4.7}_{-3.1}$
$\log_{10}(\xi)$	$2.5^{+0.2}_{-0.4}$	$2.8^{+0.1}_{-0}$	$2.8^{+0.1}_{-0}$	$2.8^{+0.1}_{-0}$
$f_{\rm cov}$	$0.78^{+0.16}_{-0.12}$	$0.61^{+0.03}_{-0.03}$	$0.55^{+0.03}_{-0.05}$	$0.68^{+0.02}_{-0.04}$
z	$-0.05^{+0.02}_{-0.01}$	$0.02^{+0.01}_{-0.01}$	$0.01^{+0.01}_{-0.01}$	$0.01^{+0.01}_{-0.01}$
		`warm26`$_2$		
$N_{\rm H}$	$8.4^{+22.7}_{-7.7}$	$0.2^{+0.2}_{-0.1}$	$0.1^{+0.1}_{-0.1}$	$0.1^{+0.1}_{-0.1}$
$\log_{10}(\xi)$	$4.8^{+1.2}_{-1.0}$	$3.6^{+0.1}_{-0.1}$	$3.6^{+0.1}_{-0.1}$	$3.7^{+0.1}_{-0.3}$
$f_{\rm cov}$	$0.95^{+0.05}_{-0.83}$	$0.95^{+0.05}_{-0.18}$	$1.00^{+0}_{-0.10}$	$0.95^{+0.05}_{-0.01}$
z	$-0.19^{+0.03}_{-0.02}$	$-0.14^{+0.01}_{-0.01}$	$-0.14^{+0.01}_{-0.01}$	$-0.15^{+0.01}_{-0.01}$
		`bbody`		
$kT_{\rm bb}$ [keV]	$0.11^{+0.01}_{-0.01}$	$0.10^{+0.01}_{-0.01}$	$0.08^{+0.02}_{-0}$	$0.08^{+0.01}_{-0}$
norm ($\times 10^{-5}$)	$2.0^{+1.7}_{-0}$	$8.0^{+0}_{-0.4}$	$8.0^{+0}_{-0.3}$	$8.0^{+0}_{-1.3}$
		`reflkerr_elp`		
$a^{(a)}$		$0.998^{+0}_{-0.001}$		
$r_{\rm c,in}$	$1.37^{+2.36}_{-1.37}$	$0.21^{+0.22}_{-0.01}$	$0.10^{+3.43}_{-0.01}$	$0.00^{+0.82}_{-0}$
$r_{\rm c,out}$	$1.55^{+0.61}_{-0.13}$	$0.24^{+0.30}_{-0.01}$	$0.50^{+0.09}_{-0.09}$	$0.12^{+0.02}_{-0.01}$
$h_{\rm max}$	$2.03^{+1.03}_{-0.54}$	$1.20^{+0.01}_{-0}$	$1.20^{+0.01}_{-0}$	$1.20^{+0.02}_{-0}$
$\Omega_{\rm K}$	$1.43^{+0.06}_{-0.33}$	$1.04^{+0.03}_{-0.10}$	$1.05^{+0.13}_{-0.01}$	$0.91^{+0.14}_{-0.09}$
$i^{(a)}$ [°]		$44.1^{+0.2}_{-0.2}$		
$\Gamma^{(b)}$	$2.46^{+0.04}_{-0.11}$	$2.49^{+0.03}_{-0.04}$	$2.58^{+0.02}_{-0.01}$	$2.70^{+0.04}_{-0.01}$
$A_{\rm Fe}^{(a,b)}$		$18.9^{+0.4}_{-0.2}$		
$\log_{10}(\xi)$	$0.0^{+0.8}_{-0}$	$3.0^{+0.1}_{-0.1}$	$3.1^{+0.1}_{-0.1}$	$3.3^{+0.1}_{-0.1}$
$\log_{10}(N)$	$18.5^{+0.1}_{-0.6}$	$19.0^{+0}_{-0.7}$	$19.0^{+0}_{-0.1}$	$18.9^{+0.1}_{-0.1}$
norm ($\times 10^{-4}$)	$1.5^{+0.8}_{-0.5}$	$2.8^{+0.3}_{-0.5}$	$4.5^{+0.5}_{-2.3}$	$16.0^{+13.0}_{-1.0}$
χ^2/DoF		802/550		
χ^2	107	254	239	202

Notes: (a) linked for all four spectra. (b) $A_{\rm Fe}$ is additionally linked for `reflkerr_elp`, `warm26` and `photem26`. For this analysis we realized that $A_{\rm Fe}$ can be fitted above 10 (which is a 'hidden' feature of `xillverD`), up to $A_{\rm Fe} = 20$. All the parameters units are the same as in Table 2.

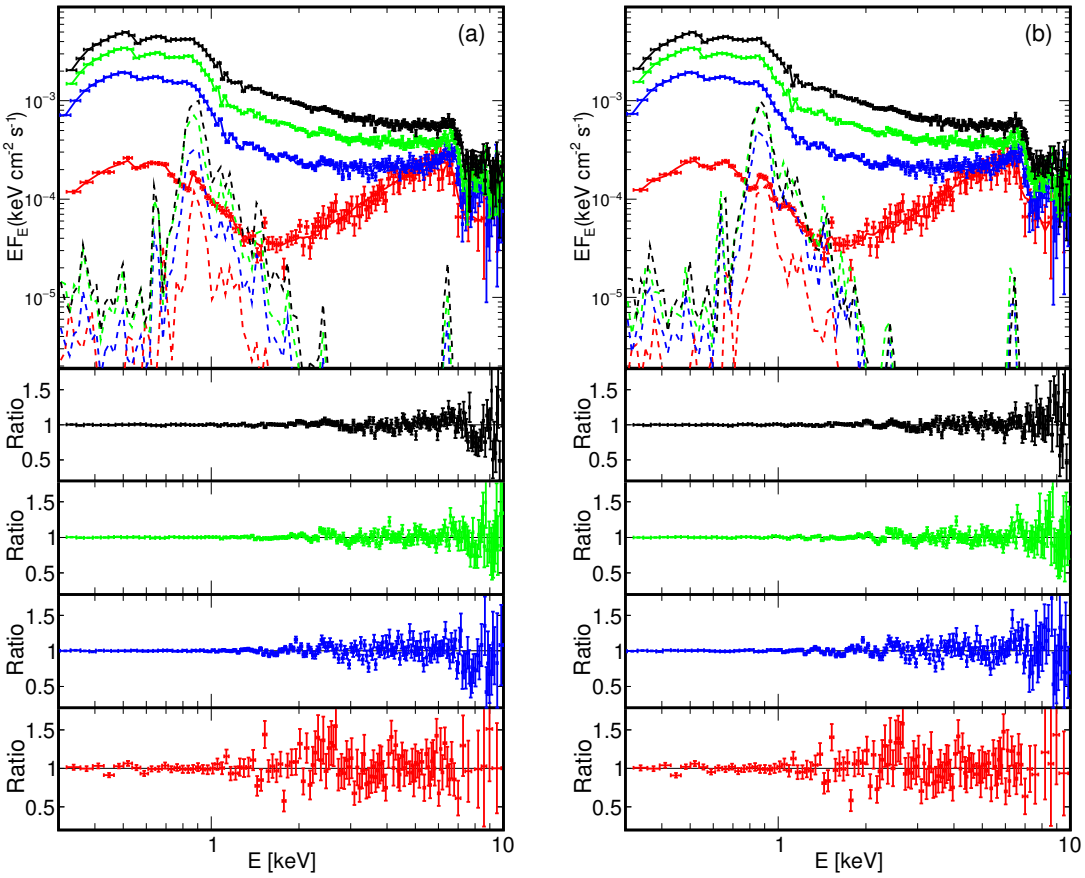

Figure 28: The upper panels show the unfolded data and model spectra for our best-fitted model (a) `2[r]` and (b) `2[x]`, using the self-consistent photoionized absorption and emission, for VL (red), L (blue), M (green) and H (black). The model parameters are given in Tables 4 and 5, respectively. The short-dashed lines show contributions of `photem26`. The lower panel shows the fit residuals given as the data-to-model ratio for VL, L, M, and H from bottom to top.

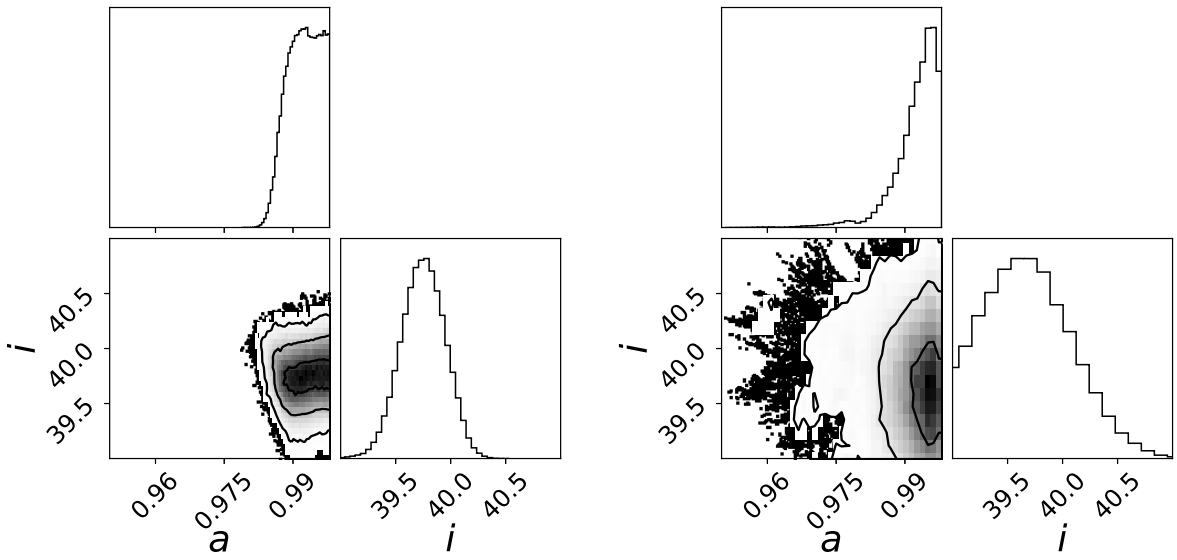

Figure 29: Probability distributions, obtained in the MCMC analysis, showing correlations between a and i parameters of model `2[r]` for $r_{\rm in} = r_{\rm ISCO}$ (left) and free $r_{\rm in}$ (right).

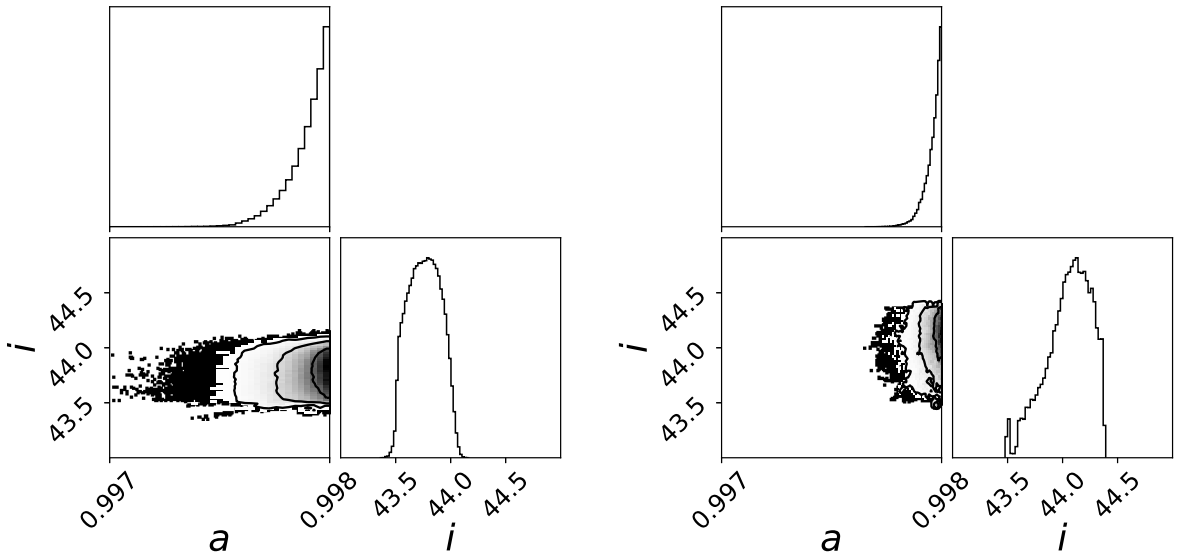

Figure 30: Probability distributions, obtained in the MCMC analysis, showing correlations between a and i parameters of model `2[x]` for $r_{\rm in} = r_{\rm ISCO}$ (left) and free $r_{\rm in}$ (right).

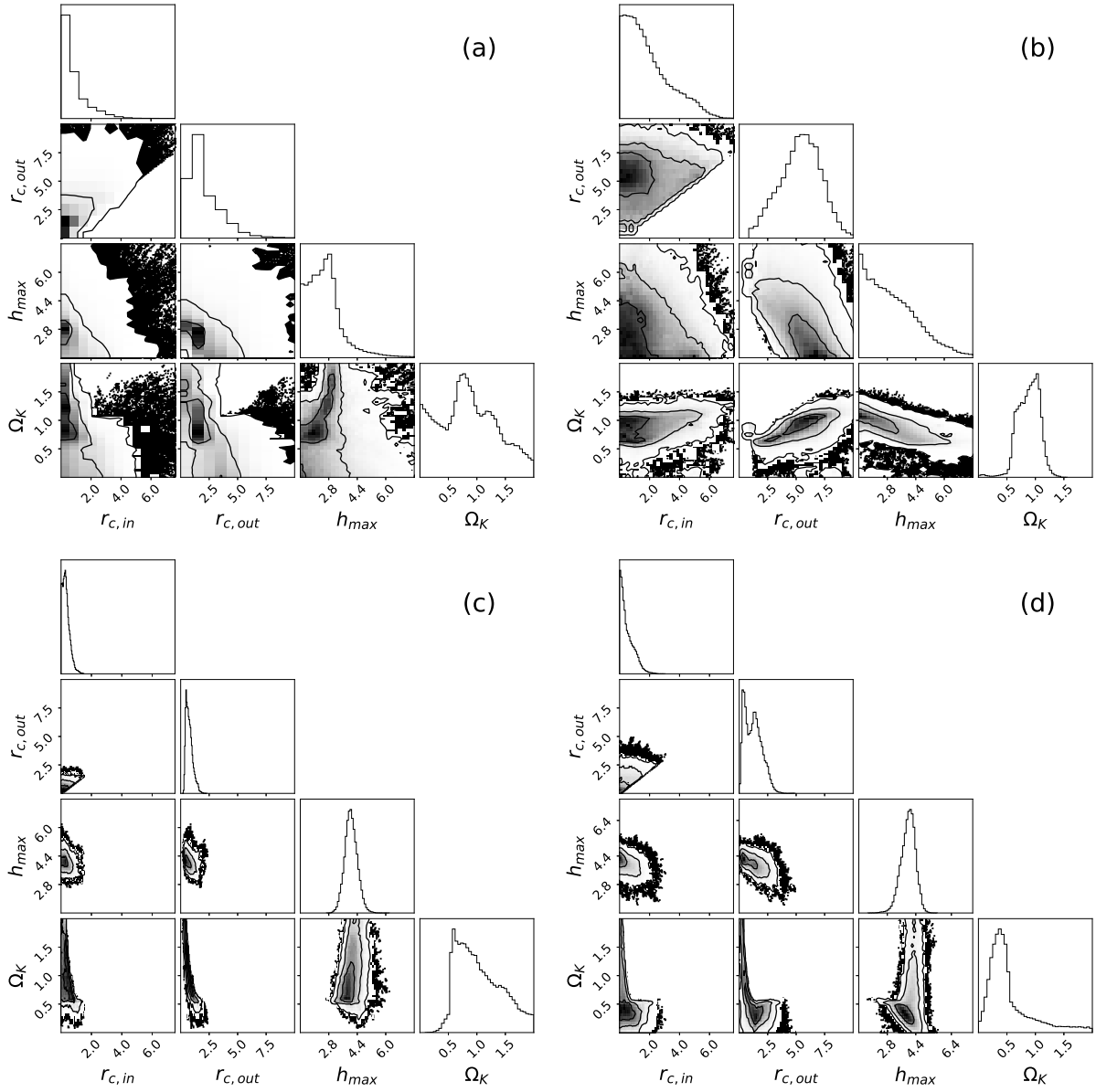

Figure 31: Probability distributions, obtained in the MCMC analysis, showing correlations between the $r_{\rm c,in}$, $r_{\rm c,out}$, $h_{\rm max}$ and $\Omega_{\rm K}$ parameters of model `2[r]` (see Table 4) for (a) VL, (b) L, (c) M, and (d) H.

different ionization parameters, $\xi_1 \sim 10$ and $\xi_2 \gtrsim 1000$, which dominate the reflection spectrum, respectively, above and below ~ 1.5 keV (e.g. Dauser et al. 2012; Fabian et al. 2012; Zoghbi et al. 2010). All those models used `reflionx` for rest-frame reflection. We attempted to apply such a model, strictly following Dauser et al. (2012), i.e. we used model `tbabs(swind1(relconv_lp*reflionx`$_1$ `+ relconv_lp*reflionx`$_2$ `+ bbody)` to our spectra L, M and H; `relconv_lp` is the convolution version of the lamp-post model in the `relxill` family, `swind1` is the model of partially ionized absorption, in which absorption tables calculated for $\Gamma = 2.4$ with an old version of `XSTAR` (released in 2006) are convolved with Gaussian smearing and the solar abundance of iron is assumed. The spectral indices of both `reflionx` components are linked and `relconv_lp` in both cases uses the same (linked) parameters. We found very similar parameters to those reported by Dauser et al. (2012), in particular $\xi_1 \simeq (10 - 20)$ and $\xi_2 \simeq 2000$, $A_{\rm Fe} \simeq 20$, $i \simeq 50°$, $a \simeq 0.998$ and $h \simeq (2 - 3)$ in all three states, however, the quality of the fit is very poor, $\chi^2/{\rm DoF} = 1976/484$ (however, using spectra binned using `grppha`, see Section 4.4.2, we found $\chi^2/{\rm DoF} \simeq 1.3$, comparable to that reported in Dauser et al. 2012). We then replaced `swind1` with our `warm26` and we found some improvements in the fit, $\chi^2/{\rm DoF} = 1617/487$ if $A_{\rm Fe} = 1$ in `warm26`, with parameters of `relconv_lp` and both `reflionx` almost the same as in the version with `swind1`. The fitted spectra with the contribution of reflection and power-law components are shown in Figure 32. After linking $A_{\rm Fe}$ in `warm26` to `reflionx` we get $\chi^2/{\rm DoF} = 1642/487$ for the fitted $A_{\rm Fe} \simeq 9$ and other parameters insignificantly changed. We then tried to use various versions of `xillver` instead of `relxill`, but this gave an even worse description of the data.

4.5 Summary and discussion

1H 0707–495 exhibits one of the most extreme relativistic distortions of reflection features and has been observed repeatedly by `XMM` with the total exposure of 1.3 Ms, possibly the longest among all AGNs. This represents an excellent case for the application of our model for constraining the corona and disk parameters. We developed a self-consistent model for this X-ray source involving significant contributions of reflection and photoionized absorption and emission components. The presence

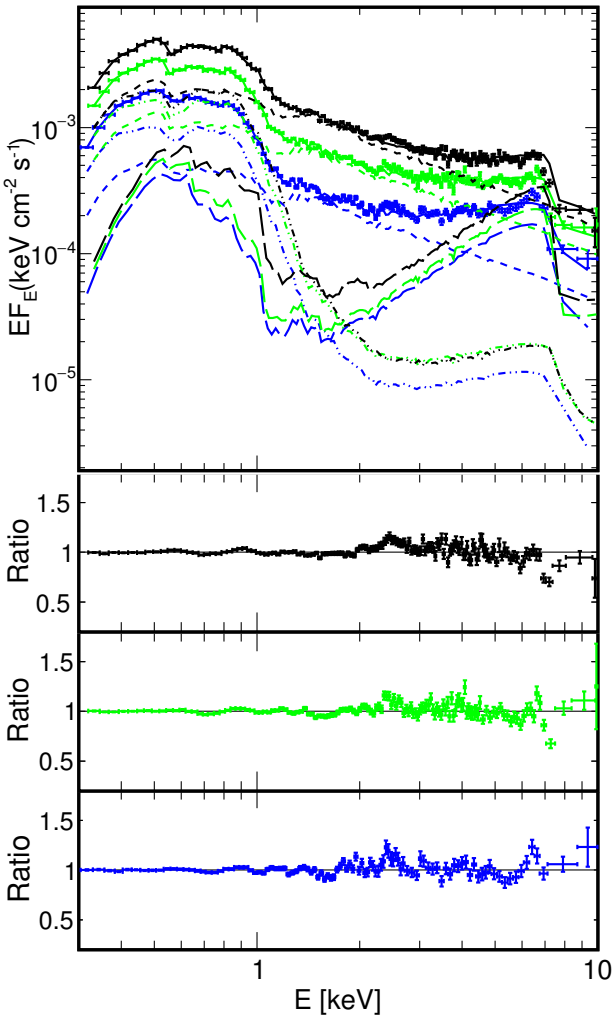

Figure 32: The upper panels show the unfolded data and model spectra for our best-fitted double-reflection model for L (blue), M (green) and H (black). The less- and more-ionized reflection is shown by the long-dashed and dot-dashed lines, respectively, and the power-law is shown by the short-dashed lines. The lower panel shows the fit residuals given as the data-to-model ratio for L, M, and H from bottom to top.

of the latter two with parameters similar to these found in our model was inferred from the RGS data by Kosec et al. (2018) and Dauser et al. (2012).

Our final fitted models have some systematic residuals, e.g. around 2–3 keV, see the residual plots in Figures 24 and 28, which is then reflected in the values of χ^2/DoF. The model could be further improved e.g. by considering the variable abundance of Si or S (which would possibly reduce the features at $\sim 2-3$ keV, likely representing photoionized emission of these elements), and by including the emission/absorption model dependent on Γ (which would likely improve the description at ~ 6.5 keV, as discussed above). Nevertheless, our models give a much better agreement with the X-ray spectrum of 1H 0707–495 than any previous model considered for this source (in particular, models including a double reflection). Furthermore, these previous models, in addition to giving a worse quality of spectral fits, used inconsistent spectral setups with a highly super-solar abundance of iron in the disk and a solar abundance of iron in absorbers (e.g. Dauser et al. 2012), and in some cases were limited to energy bands neglecting the soft excess (e.g. Hagino et al. 2016; Mizumoto et al. 2019; Wilkins & Fabian 2011).

Below we discuss properties of the corona and ionized outflow implied by our results.

4.5.1 Corona

Our conclusions regarding the X-ray corona are the same as in Szanecki et al. (2020), i.e. the corona must be very compact, at most a gravitational radius in size, and located at most a few gravitational radii from the black-hole horizon. However, we note a systematic difference between the parameters estimated using either `reflionx` or `xillverD`. Models using the former were fitted with the height of the corona $h_{\rm max} \simeq (3-4)$, which is consistent with the height of the X-ray source obtained by modeling the time lags by Caballero-García et al. (2018). Models using `xillverD` are fitted with much lower $h_{\rm max} < 2$, i.e. the X-ray source is here essentially on the event horizon, and all objectives to such models related to the strong advection of photons under the horizon (Niedźwiecki et al. 2016) become relevant. These differences in the geometrical parameters translate into the formation of the total spectrum, see Figures 33 and 34. The extremely low h fitted in models with `xillverD` implies that

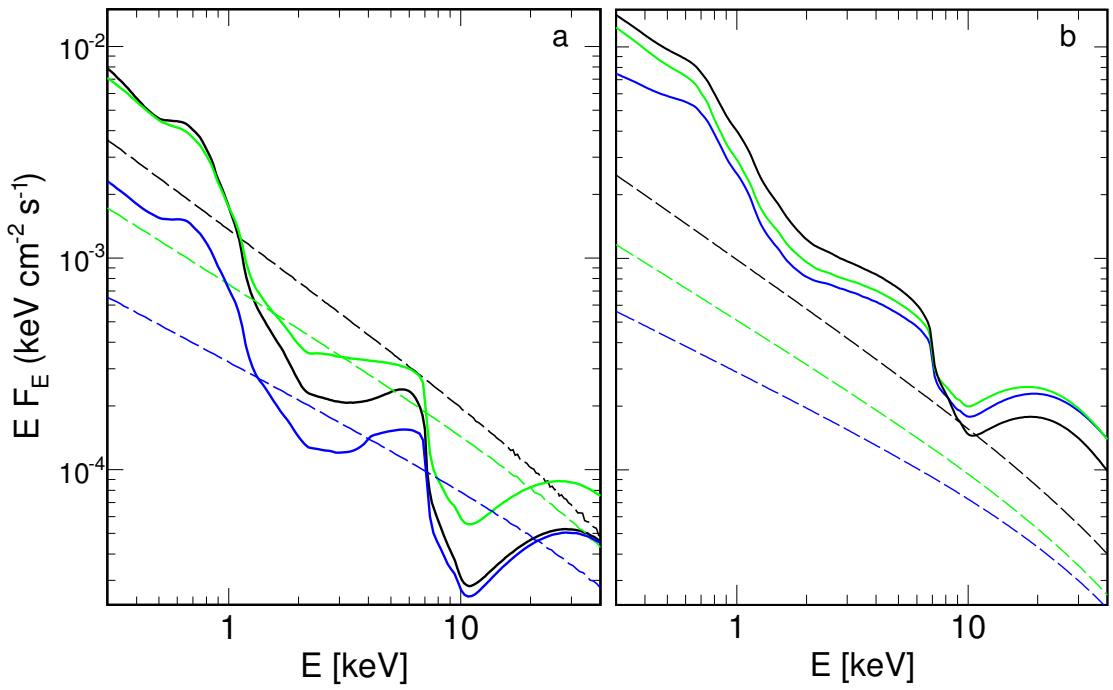

Figure 33: The unabsorbed `reflkerr_elp` spectra of our models shown in Figure 24 for L (blue), M (green) and H (black). (a) Model `1[r]`, (b) model `1[x]`. The primary and reflected spectra are shown separately by the dashed and solid curves, respectively.

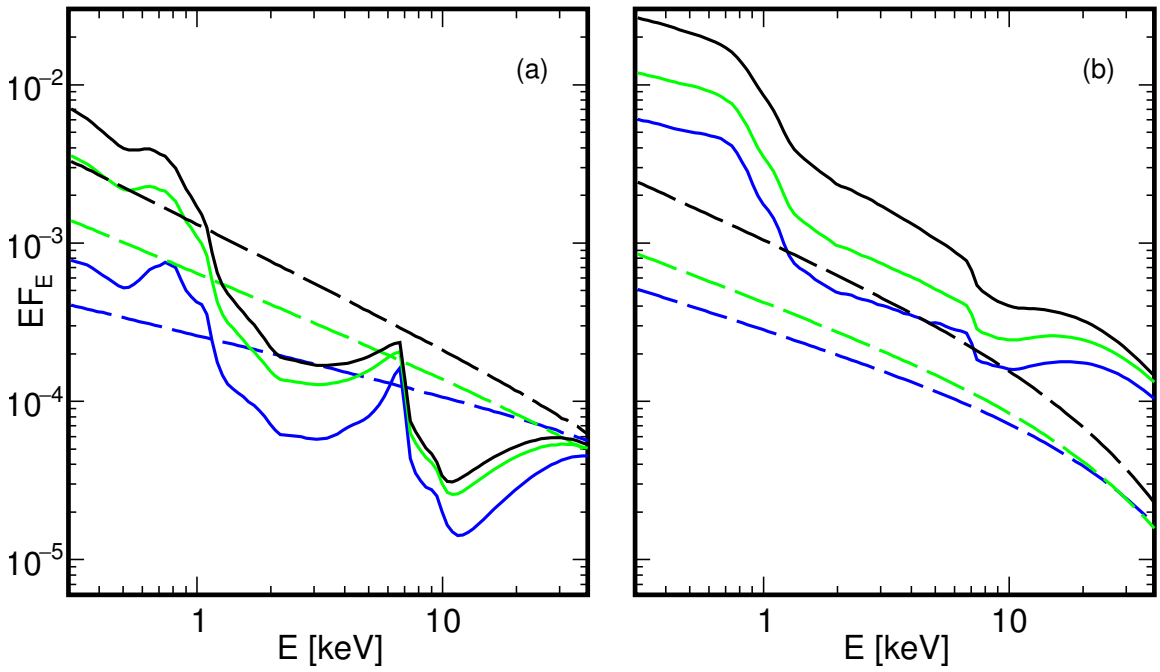

Figure 34: The unabsorbed `reflkerr_elp` spectra of our models shown in Figure 28 for L (blue), M (green) and H (black). (a) Model `2[r]`, (b) model `2[x]`. The primary and reflected spectra are shown separately by the dashed and solid curves, respectively.

the observed spectrum is fully dominated by reflection (due to the light bending, increasing the disk irradiation) as indeed seen in panels (b) of Figures 33 and 34, and we note that this property of the models fitted with the high density of the disk does not depend on the specific form of photoionized emission/absorption components (i.e. we find it both in model `1[x]` and `2[x]`). This form of the spectrum is in contradiction to the variability studies, in which the dominance of the direct power-law component in the 1–4 keV was inferred (see Section 4.1). On the other hand, models using `reflionx` are consistent with those variability properties, see panels (a) in Figure 33 and 34.

We do not find systematic changes in the geometrical parameters of the corona with the change of the X-ray flux; we note a fluctuation of the fitted parameters for spectrum L in model `2[r]`, which may be incidental. We also note an interesting indication of a Keplerian rotation of the corona, which we inferred both by fixing a Keplerian velocity and allowing the scaling parameter $\mathcal{R}$ to fit freely in models 1, and by allowing the angular velocity to fit freely in models 2.

The major systematic variability trend in the parameters of the X-ray source concerns the shape of the coronal spectrum, see Figure 35. The clear *softer-when-brighter* behavior revealed in our analysis is well known to characterize the X-ray spectral variability of moderate and high accretion rate AGNs (e.g. Sobolewska & Papadakis 2009; Soldi et al. 2014).

4.5.2 Ionized wind

We discuss here the properties of the ionized outflow based on parameters obtained in models 2, with `warm26` and `photem26`, which give a more consistent description of the photoionized absorption and emission (than models 1).

In the VL state, the absorber has different properties than during other observations, which is possibly related to the prolonged (over a month) period of X-ray faintness that preceded the VL observation (Fabian et al. 2012). The absorber in this state is weakly ionized (at $\Gamma = 2.6$, assumed in `warm26`, this low ionization corresponds to a relatively large ionization parameter, see Appendix) and strongly absorbs the continuum emission. Such a solution for the VL spectrum was discussed by Hagino et al. (2016). In the rest of this section, we discuss only the higher flux

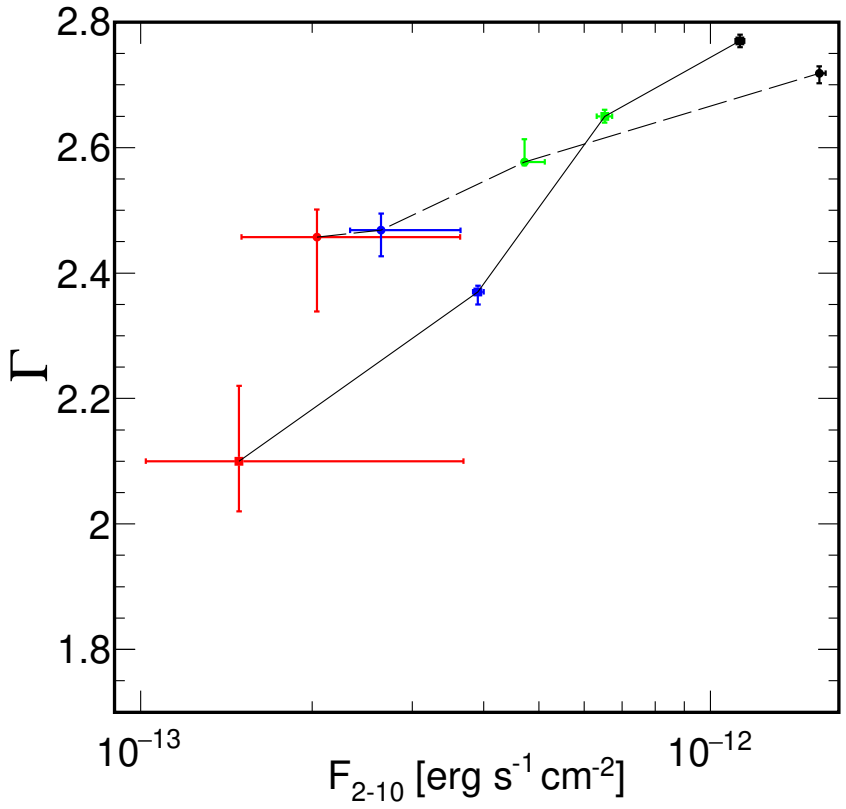

Figure 35: Parameters of the coronal emission fitted in VL (red), L (blue), M (green) and H (black) in model `2[r]` (points connected by the solid line) and `2[x]` (points connected by the dashed line). F_{2-10} is the flux in 2–10 keV range for the unabsorbed power-law component.

states.

The photem26 emitter was fitted in all cases with outflow velocity (in the host galaxy frame) $\simeq 7000$ km s^{-1}, which is consistent with that inferred by Kosec et al. (2018). Kosec et al. (2018) reported also changes in the emitter velocity, estimated from the shift of the O VIII revealed in the RGS data (RGS is the detector onboard XMM satellite with better spectral resolution capabilities below 1 keV than Epic pn). However, these reported changes, by $\Delta v \simeq 1000$ km s^{-1}, are smaller than the uncertainty of the outflow velocity in our spectral fits. The ionization parameter in photem26 is fitted in all cases at $\xi \sim 600$, higher than $\xi \sim 200$ found by Kosec et al. (2018), which may be due to differences in applied models (the differences between our photem26 and photemis used by Kosec et al. 2018; are illustrated in Figure 39). Notably, the spectrum predicted by photem26 for $\xi \sim 600$, see e.g. Figure 39b, qualitatively agrees with the presence of a very strong O VIII line at ~ 0.65 keV and a weaker N VII line at ~ 0.5 keV, and the apparent absence of an O VII line at ~ 0.56 keV inferred by Kosec et al. (2018) from the RGS data.

The velocity of absorbers in model 2[r], i.e. ~ 48000 km s^{-1} for the less ionized warm26$_1$ and ~ 36000 km s^{-1} for the more ionized warm26$_2$ are also in approximate agreement with estimates of Dauser et al. (2012) and Kosec et al. (2018). Specifically, Kosec et al. (2018) considered the flux-selected low luminosity spectrum, similar to our spectrum L, and found an absorber at ~ 40000 km s^{-1}, whereas Dauser et al. (2012) fitted the total spectra of long XMM observations in 2008 and 2010 and found ~ 31000 km s^{-1} and ~ 50000 km s^{-1}, respectively. The velocity of absorbers in model 2[x] (~ 8000 km s^{-1} and ~ 65000 km s^{-1}) do not agree with any previously reported value.

The ionization parameters of ionized absorbers in our models are larger than those estimated by Dauser et al. (2012) and Kosec et al. (2018), however, this property is strongly model dependent.

We find a systematic decrease in the strength of absorption lines with increasing X-ray flux (at least in model 2[r]). The decrease may be due to the increase of the ionization of the absorber and/or the decrease of the column density. In our model, we find the latter. Physically, the relationship between the flux and the ionization could be rather expected. We then note that the ionization parameter

fitted `warm26`$_2$, $\xi = 10^6$, is the maximum value in `warm26`, which may have affected this result of our model.

Apart from a systematic decrease of $N_{\rm H}$ in `warm26` and an increase of normalization in `photem26` (indicating the increase in the amount of the emitting gas; the column density cannot be measured in this model) with increasing X-ray flux, we also find a systematic increase of the velocity of `warm26`$_2$ (in model `2[r]`), which can be expected for a wind driven by radiation pressure of the central source. This apparent response to the changes in the X-ray flux constrains the distance of the wind. Investigating the `XMM` light curves of 1H 0707–495 we found that the typical time scale for the change of the X-ray flux level is $\sim 10^4$, which implies that absorbing material must be located within $\sim 10^{-4}$ pc ($\sim 10^3 R_{\rm g}$ for a $2 \times 10^6 M_\odot$ black hole) from the X-ray source. We note that similar properties of the ionized absorber, namely anti-correlation of the strength of the absorption lines with the flux and its response to changes of the X-ray source on a time scale of ~ 5 ks, were assessed by Parker et al. (2017) in IRAS 13224-3809, which is a NLSy1 galaxy showing a rapid variability similar to 1H 0707–495.

4.5.3 Disk and black hole

Our model with a high-density disk, using `xillverD` rest-frame reflection, is fully dominated by reflection in the total energy range (which is in contradiction to the observed variability), and has a very unlikely location of the X-ray source ($\lesssim 0.2 R_{\rm g}$ from the event horizon) as well as a rather unlikely model of absorption. We, therefore, disfavor this solution for 1 H0707–495. In turn, the low density model, using `reflionx`, has properties consistent with earlier estimates of the wind parameters and variability of this source.

The disk extends down to the ISCO (or very close to it) in all our models and an almost maximal rotation of the central black hole is strongly preferred.

5 Conclusions

The main conclusions of the results presented in this dissertation are summarized as follows:

(1) For an untruncated disk, the fitting results obtained with a point-like source can be reproduced only with a very small size of the corona (at most a gravitational radius).

(2) An extended corona (with a size much larger than the gravitational radius) not only does not reproduce the steep emissivities inferred in some fitted models but actually produces spectra consistent with a significantly truncated disk.

(3) Significant anisotropy of the X-ray source, which may reduce the reflection strength by a factor of several (or more), affects also significantly the relativistic distortion of the spectrum. Neglecting the latter makes the model non-physical. This concerns, in particular, the anisotropy due to an outflow.

(4) The spectrum of Cygnus X-1 in its hard state is consistent with two configurations: (i) a rather compact (the size of a few gravitational radii) X-ray source with a mildly relativistic outflow of electrons, at a height of several gravitational radii above the disk whose truncation is slightly preferred, or (ii) an inner corona with a moderate optical thickness (consistent with the X-ray spectral shape) irradiating the surrounding, truncated disk. In either scenario, the black-hole spin cannot be measured by reflection spectroscopy.

(5) The full X-ray spectrum of 1H 0707–495 (including its soft excess) can be explained by the model involving a compact (about a gravitational radius in size) corona located close (a few gravitational radii) from the black hole and irradiating an untruncated disk of a rapidly rotating black hole. This model requires a strong contribution of photoionized outflow, with parameters consistent with earlier estimations, and it provides a much better description of the observed spectra than the double-reflection model. Rotation of the corona with Keplerian angular velocity of the ISCO gives a proper amount of reflected radiation.

(6) The main spectral evolution trend observed in 1H 0707–495 concerns the softening of the X-ray continuum with the brightening of the source. No systematic changes in the source geometry are found.

(7) The solution for 1H 0707–495 involving high-density disk, proposed in some

earlier works, is disfavored.

The objects considered in this dissertation represent the two main spectral states observed in black-hole systems, hard and soft. The results for 1H 0707–495 support the model relating the soft state to an optically thick disk extending down to the black hole. A rather obvious development of this research would involve the application of the extended-corona model to objects with similar properties, in particular, MCG–6-30-15 and IRAS 13224-3809. The results for Cygnus X-1 support the model relating the hard state to the disk truncation. The model with an outflow in the corona can be applied to observations of other sources in their hard states to verify if they are consistent with an untruncated disk and reduction of reflection due to the outflow.

A Photoionized absorption and emission

Figure 36 illustrates how the spectrum of the ionizing radiation and the iron abundance affect the shape of the absorbed spectrum. In all panels the solid black line shows the absorbed spectrum computed with `zxipcf` with $\log \xi = 3.4$ and $N_{\rm H} = 10^{24}$ cm^{-2} (which characterize the larger-$N_{\rm H}$ absorber in our fits with model `1[r]` presented in Section 4.4.1). The solid red line in panel (a) shows the absorbed spectrum computed with `warm26` for the same parameters, so the only difference between the models is due to $\Gamma = 2.2$ assumed in `zxipcf` and $\Gamma = 2.6$ assumed in `warm26`. We see that for these parameters the `warm26` absorber is much less ionized and gives a much stronger absorption. As discussed in Section 1.6.1, for this large value of ξ ($\simeq 3000$), the heating is dominated by the Compton heating, and then the harder ionizing spectrum makes the absorber hotter and more ionized. The less efficient heating in `warm26` can be counterbalanced by increasing ξ (which implies a larger irradiating flux), as shown in panel (b). Then, panel (c) shows the effect of increasing $A_{\rm Fe}$. The increased opacity again gives a strongly absorbed spectrum, which effect may be partially compensated by a further increase of ξ, see panel (d).

We also note that changes in ξ and $N_{\rm H}$ cannot fully compensate the change of opacity related with higher values of $A_{\rm Fe}$ and Γ taken into account in `warm26`, and the overall effect of ionized absorption on the spectrum in model 1 is slightly different than in model 2, see Figure 37.

The effect of the less ionized absorber (i.e. $\texttt{zxipcf}_1$ or $\texttt{warm26}_1$) on the spectrum is to produce a continuum curvature rather than distinct ionized absorption lines, especially in models `[x]`. In turn, the more ionized absorber (i.e. $\texttt{zxipcf}_2$ or $\texttt{warm26}_2$) has rather a little continuum absorption and is instead dominated by ionized line features, as shown in Figure 38.

The dashed green lines in Figure 39 show the Gaussian components fitted in model `1[x]` to spectrum L. As discussed in Section 4, the inclusion of the Gaussian at ~ 0.9 keV is critical for a description of spectra L, M and H in both the model `1[r]` and `1[x]` and in all cases we found almost the same parameters of this component. We presume that this Gaussian component represents a blend of the Fe XVII–XIX lines from a photoionized outflow. Indeed, we checked that replacing this Gaussian with the photoionized emission model computed with `XSTAR` and implemented in

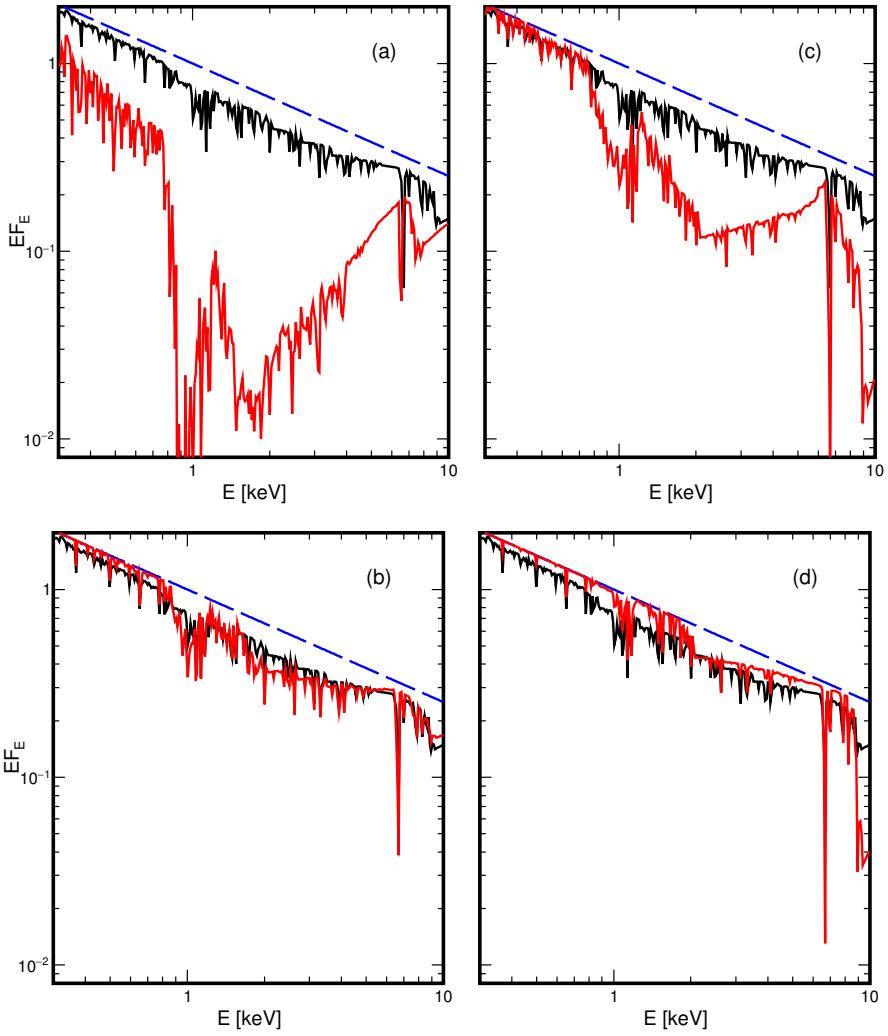

Figure 36: Effect of ionized absorption on power-law spectrum. The unabsorbed power-law with $\Gamma = 2.6$ is shown by the dashed blue line. The solid black line in all panels shows the spectrum absorbed by `zxipcf` with $\log \xi = 3.4$. The solid red line in all panels shows the spectrum absorbed by `warm26` with (a) $\log \xi = 3.4$ and $A_{Fe} = 1$, (b) $\log \xi = 4.6$ and $A_{Fe} = 1$, (c) $\log \xi = 4.6$ and $A_{Fe} = 10$, and (d) $\log \xi = 5.3$ and $A_{Fe} = 10$. In all panels both `zxipcf` and `warm26` assume the same $N_H = 10^{24}$ cm^{-2} and both are calculated for the same $v_{turb} = 200$ km s^{-1}. In all models a total covering of the source, i.e. $f_{cov} = 1$, is assumed.

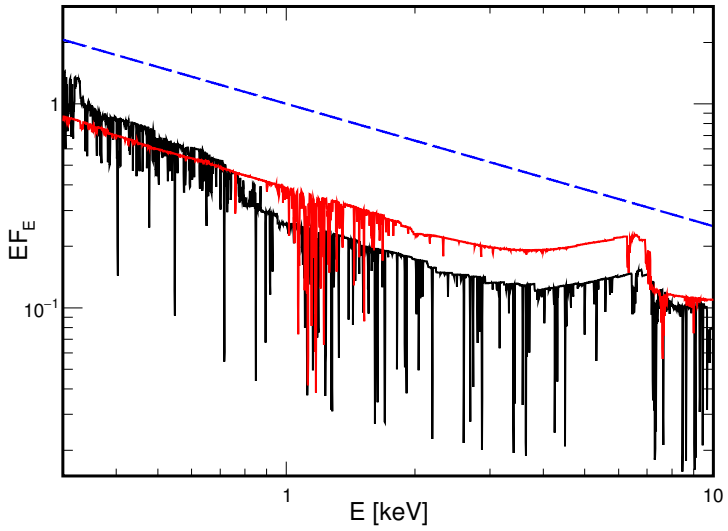

Figure 37: Total absorption to L in model `1[x]` (with `zxipcf`, Table 3; black) and `2[x]` (with `warm26`, Table 5; red)

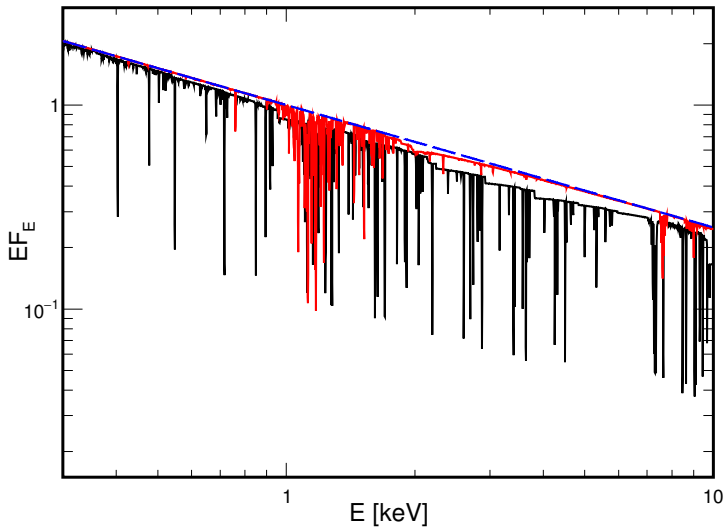

Figure 38: More ionized absorber fitted to L in model `1[x]` (with `zxipcf`, Table 3; black) and `2[x]` (with `warm26`, Table 5; red)

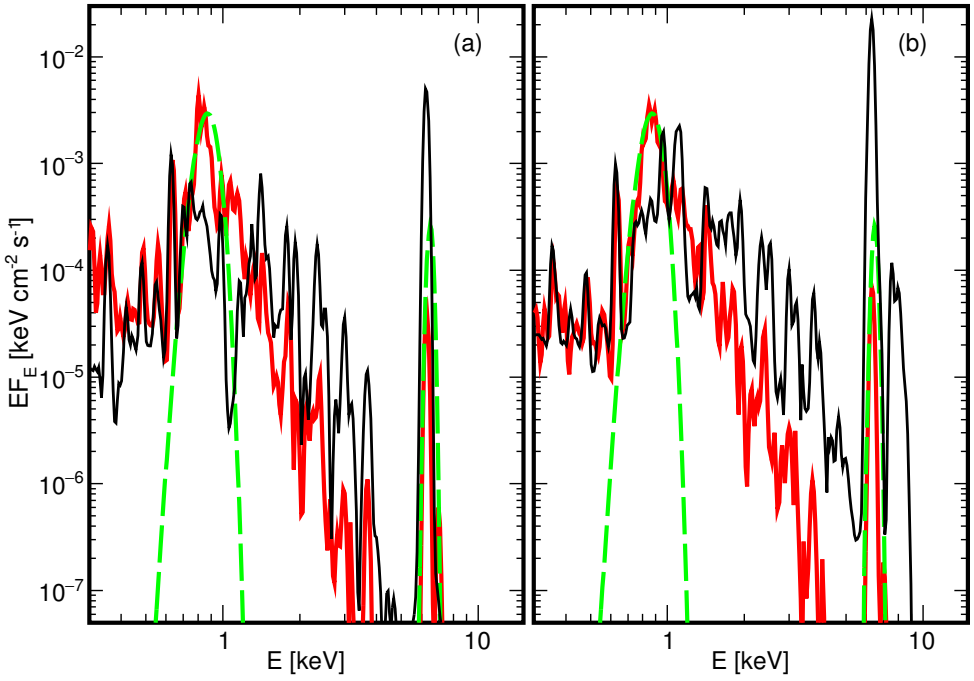

Figure 39: The dashed green lines show the Gaussian components fitted in our model `1[x]` to spectrum L (Table 3). The solid black lines show the `photemis` spectra solid red lines show the `photem26` spectra, both redshifted by $(1+z) = 1.02$, corresponding to outflow at ~ 6000 km s^{-1} (in the frame of the host galaxy of 1H 0707–495). Both `photemis` and `photem26` assume the same $A_{Fe} = 17$ and both are computed for the same $v_{turb} = 6000$ km s^{-1}. (a) $\log_{10}\xi = 2.3$, (b) $\log_{10}\xi = 2.8$.

`xspec`, `photemis`, we get an unaffected fit quality in our models at $E < 6$ keV (but not at $E > 6$ keV, see below) and the parameters of other spectral components are not affected. Then, at the energy resolution of the `EPIC pn` detector, the blend of the Fe lines around 0.9 keV, clearly visible in the model spectra in Figure 39, cannot be distinguished from a single broad Gaussian component. In such a fitted model, the ionization parameter in `photemis`, $\log \xi \simeq 2.3$, is in agreement with that assessed by Kosec et al. (2018) for outflowing emitter. However, the fitted outflow velocity, $\simeq 36000$ km s^{-1}, is much higher than $\simeq 7000$ km s^{-1} estimated by Kosec et al. (2018); as seen in Figure 39, the broad feature in the spectrum predicted by `photemis` is shifted to lower energies and should be indeed strongly blueshifted to match the Gaussian. The main problem with `photemis`, however, concerns the Fe Kα line, which is about two orders of magnitude stronger than allowed by the data (as seen in the comparison with the second Gaussian component in Figure 39). Therefore, attempts to describe the photoionized emission with `photemis` in the full energy range give a very strong residual around 6.5 keV and a very large χ^2.

The photon index assumed for computation of the ion population in `photemis`, $\Gamma = 2$, is much lower than that characterizing the intrinsic emission of 1H 0707–495 and we found that all the above problems can be solved if a softer ionizing continuum is assumed. The `photem26` model (for $\Gamma = 2.6$) matches very well the empirical Gaussian for $\log \xi \simeq 2.8$ (Figure 39b) and allows us to fit the 1H 0707–495 data for the outflow velocity $\simeq 7000$ km s^{-1}, in agreement with Kosec et al. (2018) estimation. The intensity of the Fe Kα line is now slightly too small. This intensity is very sensitive to the value of Γ and a better agreement could be obtained for a slightly harder spectrum.

References

Abbott B. P., et al., (2016), *Observation of Gravitational Waves from a Binary Black Hole Merger*, Phys. Rev. Lett., 116, 061102

Abbott R., et al., (2023), *Population of Merging Compact Binaries Inferred Using Gravitational Waves through GWTC-3*, Physical Review X, 13, 011048

Abramowicz M. A., Czerny B., Lasota J. P., Szuszkiewicz E., (1988), *Slim Accretion Disks*, The Astrophysical Journal, 332, 646

Abramowicz M. A., Chen X., Kato S., Lasota J., Regev O., (1995), *Thermal Equilibria of Accreting Disks*, The Astrophysical Journal, 438, L37

Abramowicz M. A., Chen X. M., Granath M., Lasota J. P., (1996), *Advection Dominated Accretion Flows Around Kerr Black Holes*, The Astrophysical Journal, 471, 762

Agazie G., et al., (2023), *The NANOGrav 15 yr Data Set: Evidence for a Gravitational-wave Background*, ApJ, 951, L8

Antonucci R., (1993), *Unified models for active galactic nuclei and quasars.*, ARA&A, 31, 473

Balbus S. A., Hawley J. F., (1998), *Instability, turbulence, and enhanced transport in accretion disks*, Reviews of Modern Physics, 70, 1

Bambi C., et al., (2021), *Towards Precision Measurements of Accreting Black Holes Using X-Ray Reflection Spectroscopy*, Space Sci. Rev., 217, 65

Barausse E., (2012), *The evolution of massive black holes and their spins in their galactic hosts*, MNRAS, 423, 2533

Bardeen J. M., Press W. H., Teukolsky S. A., (1972), *Rotating Black Holes: Locally Nonrotating Frames, Energy Extraction, and Scalar Synchrotron Radiation*, ApJ, 178, 347

Basak R., Zdziarski A. A., Parker M., Islam N., (2017), *Analysis of NuSTAR and Suzaku observations of Cyg X-1 in the hard state: evidence for a truncated disc geometry*, MNRAS, 472, 4220

Belczynski K., Done C., Hagen S., Lasota J. P., Sen K., (2021), *Common origin of black holes in high mass X-ray binaries and in gravitation-wave sources*, arXiv e-prints, p. arXiv:2111.09401

Beloborodov A. M., (1999), *Plasma Ejection from Magnetic Flares and the X-Ray Spectrum of Cygnus X-1*, ApJ, 510, L123

Boller T., Brandt W. N., Fink H., (1996), *Soft X-ray properties of narrow-line*

Seyfert 1 galaxies., A&A, 305, 53

Boller T., et al., (2002), *XMM-Newton discovery of a sharp spectral feature at ~7 keV in the narrow-line Seyfert 1 galaxy 1H 0707 - 49*, MNRAS, 329, L1

Brown G. E., Bethe H. A., (1994), *A Scenario for a Large Number of Low-Mass Black Holes in the Galaxy*, ApJ, 423, 659

Caballero-García M. D., Papadakis I. E., Dovčiak M., Bursa M., Epitropakis A., Karas V., Svoboda J., (2018), *Testing the X-ray reverberation model KYNREFREV in a sample of Seyfert 1 Active Galactic Nuclei*, MNRAS, 480, 2650

Coppi P. S., (1999), in Poutanen J., Svensson R., eds, Astronomical Society of the Pacific Conference Series Vol. 161, High Energy Processes in Accreting Black Holes. p. 375 (`arXiv:astro-ph/9903158`)

Crummy J., Fabian A. C., Gallo L., Ross R. R., (2006), *An explanation for the soft X-ray excess in active galactic nuclei*, MNRAS, 365, 1067

Dauser T., et al., (2012), *Spectral analysis of 1H 0707-495 with XMM-Newton*, MNRAS, 422, 1914

Dauser T., Garcia J., Wilms J., Böck M., Brenneman L. W., Falanga M., Fukumura K., Reynolds C. S., (2013), *Irradiation of an accretion disc by a jet: general properties and implications for spin measurements of black holes*, MNRAS, 430, 1694

Davis S. W., Laor A., (2011), *The Radiative Efficiency of Accretion Flows in Individual Active Galactic Nuclei*, ApJ, 728, 98

Di Salvo T., Done C., Życki P. T., Burderi L., Robba N. R., (2001), *Probing the Inner Region of Cygnus X-1 in the Low/Hard State through Its X-Ray Broadband Spectrum*, ApJ, 547, 1024

Done C., Jin C., (2016), *The mass and spin of the extreme Narrow Line Seyfert 1 Galaxy 1H 0707-495 and its implications for the trigger for relativistic jets*, MNRAS, 460, 1716

Done C., Zycki P. T., (1999), *Relativistic distortions in the X-ray spectrum of CYG X-1*, MNRAS, 305, 457

Done C., Mulchaey J. S., Mushotzky R. F., Arnaud K. A., (1992), *An Ionized Accretion Disk in Cygnus X-1*, ApJ, 395, 275

Done C., Wardziński G., Gierliński M., (2004), *GRS 1915+105: the brightest Galactic black hole*, MNRAS, 349, 393

Done C., Gierliński M., Kubota A., (2007), *Modelling the behaviour of accretion*

flows in X-ray binaries. Everything you always wanted to know about accretion but were afraid to ask, The Astronomy and Astrophysics Review, 15, 1

Dovčiak M., Karas V., Yaqoob T., (2004), *An Extended Scheme for Fitting X-Ray Data with Accretion Disk Spectra in the Strong Gravity Regime*, ApJS, 153, 205

Dziełak M. A., Zdziarski A. A., Szanecki M., De Marco B., Niedźwiecki A., Markowitz A., (2019), *Comparison of spectral models for disc truncation in the hard state of GX 339-4*, MNRAS, 485, 3845

Esin A. A., Narayan R., Cui W., Grove J. E., Zhang S.-N., (1998), *Spectral Transitions in Cygnus X-1 and Other Black Hole X-Ray Binaries*, ApJ, 505, 854

Event Horizon Telescope Collaboration et al., (2019), *First M87 Event Horizon Telescope Results. I. The Shadow of the Supermassive Black Hole*, ApJ, 875, L1

Event Horizon Telescope Collaboration et al., (2022), *First Sagittarius A* Event Horizon Telescope Results. I. The Shadow of the Supermassive Black Hole in the Center of the Milky Way*, ApJ, 930, L12

Fabian A. C., et al., (2009), *Broad line emission from iron K- and L-shell transitions in the active galaxy 1H0707-495*, Nature, 459, 540

Fabian A. C., et al., (2012), *1H 0707-495 in 2011: an X-ray source within a gravitational radius of the event horizon*, MNRAS, 419, 116

Fender R. P., Homan J., Belloni T. M., (2009), *Jets from black hole X-ray binaries: testing, refining and extending empirical models for the coupling to X-rays*, MNRAS, 396, 1370

Fishbach M., Kalogera V., (2022), *Apples and Oranges: Comparing Black Holes in X-Ray Binaries and Gravitational-wave Sources*, ApJ, 929, L26

Foreman-Mackey D., (2016), *corner.py: Scatterplot matrices in Python*, The Journal of Open Source Software, 24

Frank J., King A., Raine D., (2002), *Accretion Power in Astrophysics*, third edn. Cambridge University Press, Cambridge

Fukumura K., Kazanas D., (2007), *Accretion Disk Illumination in Schwarzschild and Kerr Geometries: Fitting Formulae*, ApJ, 664, 14

García J., Dauser T., Reynolds C. S., Kallman T. R., McClintock J. E., Wilms J., Eikmann W., (2013), *X-Ray Reflected Spectra from Accretion Disk Models. III. A Complete Grid of Ionized Reflection Calculations*, ApJ, 768, 146

García J. A., Dauser T., Steiner J. F., McClintock J. E., Keck M. L., Wilms J., (2015a), *On Estimating the High-energy Cutoff in the X-Ray Spectra of Black Holes*

via Reflection Spectroscopy, ApJ, 808, L37

García J. A., Steiner J. F., McClintock J. E., Remillard R. A., Grinberg V., Dauser T., (2015b), *X-Ray Reflection Spectroscopy of the Black Hole GX 339–4: Exploring the Hard State with Unprecedented Sensitivity*, ApJ, 813, 84

García J. A., Fabian A. C., Kallman T. R., Dauser T., Parker M. L., McClintock J. E., Steiner J. F., Wilms J., (2016), *The effects of high density on the X-ray spectrum reflected from accretion discs around black holes*, MNRAS, 462, 751

García J. A., Sokolova-Lapa E., Dauser T., Madej J., Różańska A., Majczyna A., Harrison F. A., Wilms J., (2020), *Accurate Treatment of Comptonization in X-Ray Illuminated Accretion Disks*, ApJ, 897, 67

Gendreau K. C., Arzoumanian Z., Okajima T., (2012), in Takahashi T., Murray S. S., den Herder J.-W. A., eds, Society of Photo-Optical Instrumentation Engineers (SPIE) Conference Series Vol. 8443, Space Telescopes and Instrumentation 2012: Ultraviolet to Gamma Ray. p. 844313, doi:10.1117/12.926396

Ghez A. M., et al., (2008), *Measuring Distance and Properties of the Milky Way's Central Supermassive Black Hole with Stellar Orbits*, ApJ, 689, 1044

Ghisellini G., Haardt F., Matt G., (2004), *Aborted jets and the X-ray emission of radio-quiet AGNs*, A&A, 413, 535

Gierlinski M., Zdziarski A. A., Done C., Johnson W. N., Ebisawa K., Ueda Y., Haardt F., Phlips B. F., (1997), *Simultaneous X-ray and gamma-ray observations of CYG X-1 in the hard state by GINGA and OSSE*, MNRAS, 288, 958

Gierliński M., Maciołek-Niedźwiecki A., Ebisawa K., (2001), *Application of a relativistic accretion disc model to X-ray spectra of LMC X-1 and GRO J1655-40*, MNRAS, 325, 1253

Hagino K., Odaka H., Done C., Tomaru R., Watanabe S., Takahashi T., (2016), *A disc wind interpretation of the strong Fe Kα features in 1H 0707-495*, MNRAS, 461, 3954

Harrison F. A., et al., (2013), *The Nuclear Spectroscopic Telescope Array (NuSTAR) High-energy X-Ray Mission*, ApJ, 770, 103

Ho L. C., (2008), *Nuclear activity in nearby galaxies.*, ARA&A, 46, 475

Ingram A., Mastroserio G., Dauser T., Hovenkamp P., van der Klis M., García J. A., (2019), *A public relativistic transfer function model for X-ray reverberation mapping of accreting black holes*, MNRAS, 488, 324

Jansen F., et al., (2001), *XMM-Newton observatory. I. The spacecraft and operations*,

A&A, 365, L1

Jiang J., et al., (2019), *High Density Reflection Spectroscopy - II. The density of the inner black hole accretion disc in AGN*, MNRAS, 489, 3436

Jin C., Done C., Ward M., Gierliński M., Mullaney J., (2009), *The Seyfert AGN RX J0136.9-3510 and the spectral state of super Eddington accretion flows*, MNRAS, 398, L16

Jin C., Done C., Ward M., (2017), *Super-Eddington QSO RX J0439.6-5311 - I. Origin of the soft X-ray excess and structure of the inner accretion flow*, MNRAS, 468, 3663

Kaastra J. S., Bleeker J. A. M., (2016), *Optimal binning of X-ray spectra and response matrix design*, A&A, 587, A151

Kallman T., Bautista M., (2001), *Photoionization and High-Density Gas*, ApJS, 133, 221

King A. R., Kolb U., (1999), *The evolution of black hole mass and angular momentum*, MNRAS, 305, 654

Klepczarek Ł., Niedźwiecki A., Szanecki M., (2023), *Lamp-post with an outflow and the hard state of Cyg X-1*, MNRAS, 519, L79

Kosec P., Buisson D. J. K., Parker M. L., Pinto C., Fabian A. C., Walton D. J., (2018), *A stratified ultrafast outflow in 1H0707-495?*, MNRAS, 481, 947

Krawczynski H., et al., (2022), *Polarized x-rays constrain the disk-jet geometry in the black hole x-ray binary Cygnus X-1*, Science, 378, 650

Kushwaha A., Agrawal V. K., Nandi A., (2021), *AstroSat and MAXI view of Cygnus X-1: Signature of an 'extreme' soft nature*, MNRAS, 507, 2602

Laor A., (1991), *Line Profiles from a Disk around a Rotating Black Hole*, ApJ, 376, 90

Laor A., Netzer H., Piran T., (1990), *Massive thin accretion discs. II - Polarization*, MNRAS, 242, 560

Lasota J.-P., (2001), *The disc instability model of dwarf novae and low-mass X-ray binary transients*, New Astron. Rev., 45, 449

Magdziarz P., Zdziarski A. A., (1995), *Angle-dependent Compton reflection of X-rays and gamma-rays*, MNRAS, 273, 837

Malzac J., Beloborodov A. M., Poutanen J., (2001), *X-ray spectra of accretion discs with dynamic coronae*, MNRAS, 326, 417

Malzac J., Belmont R., Fabian A. C., (2009), *Energetics of a black hole: constraints on the jet velocity and the nature of the X-ray emitting region in Cyg X-1*, MNRAS, 400, 1512

Martocchia A., Matt G., (1996), *Iron Kalpha line intensity from accretion discs around rotating black holes*, MNRAS, 282, L53

McClintock J. E., Narayan R., Steiner J. F., (2014), *Black Hole Spin via Continuum Fitting and the Role of Spin in Powering Transient Jets*, Space Sci. Rev., 183, 295

Miller J. M., Homan J., (2023), *The Black Hole GRS 1915+105 is Still Active in X-rays*, The Astronomer's Telegram, 15908, 1

Miller-Jones J. C. A., et al., (2021), *Cygnus X-1 contains a 21-solar mass black hole—Implications for massive star winds*, Science, 371, 1046

Miller L., Turner T. J., Reeves J. N., (2008), *An absorption origin for the X-ray spectral variability of MCG-6-30-15*, A&A, 483, 437

Miniutti G., Fabian A. C., (2004), *A light bending model for the X-ray temporal and spectral properties of accreting black holes*, MNRAS, 349, 1435

Mitsuda K., et al., (1984), *Energy spectra of low-mass binary X-ray sources observed from Tenma.*, PASJ, 36, 741

Mitsuda K., et al., (2007), *The X-Ray Observatory Suzaku*, PASJ, 59, S1

Miyoshi M., Moran J., Herrnstein J., Greenhill L., Nakai N., Diamond P., Inoue M., (1995), *Evidence for a black hole from high rotation velocities in a sub-parsec region of NGC4258*, Nature, 373, 127

Mizumoto M., Ebisawa K., Sameshima H., (2014), *Interpretation of the X-ray spectral variation of 1H 0707-495 with a variable double partial covering model*, PASJ, 66, 122

Mizumoto M., Ebisawa K., Tsujimoto M., Done C., Hagino K., Odaka H., (2019), *X-ray reverberation lags of the Fe-K line due to AGN disc winds*, MNRAS, 482, 5316

Narayan R., Yi I., (1995), *Advection-Dominated Accretion: Underfed Black Holes and Neutron Stars*, The Astrophysical Journal, 452, 710

Niedźwiecki A., Zdziarski A. A., (2018), *The lamppost model: effects of photon trapping, the bottom lamp, and disc truncation*, MNRAS, 477, 4269

Niedźwiecki A., Życki P. T., (2008), *On the variability and spectral distortion of fluorescent iron lines from black hole accretion discs*, MNRAS, 386, 759

Niedźwiecki A., Zdziarski A. A., Szanecki M., (2016), *On the Lamppost Model of Accreting Black Holes*, ApJ, 821, L1

Niedźwiecki A., Szanecki M., Zdziarski A. A., (2019), *Improved spectral models for relativistic reflection*, MNRAS, 485, 2942

Noda H., Done C., (2018), *Explaining changing-look AGN with state transition triggered by rapid mass accretion rate drop*, MNRAS, 480, 3898

Novikov I. D., Thorne K. S., (1973), *Astrophysics of black holes.*, Black holes (Les astres occlus), pp 343 – 450

Nowak M. A., Vaughan B. A., Wilms J., Dove J. B., Begelman M. C., (1999), *Rossi X-Ray Timing Explorer Observation of Cygnus X-1. II. Timing Analysis*, ApJ, 510, 874

Ohsuga K., Mineshige S., (2011), *Global Structure of Three Distinct Accretion Flows and Outflows around Black Holes from Two-dimensional Radiation-magnetohydrodynamic Simulations*, ApJ, 736, 2

Padovani P., et al., (2017), *Active galactic nuclei: what's in a name?*, A&ARv, 25, 2

Page D. N., Thorne K. S., (1974), *Disk-Accretion onto a Black Hole. Time-Averaged Structure of Accretion Disk*, ApJ, 191, 499

Parker M. L., et al., (2015), *NuSTAR and Suzaku Observations of the Hard State in Cygnus X-1: Locating the Inner Accretion Disk*, ApJ, 808, 9

Parker M. L., et al., (2017), *The response of relativistic outflowing gas to the inner accretion disk of a black hole*, Nature, 543, 83

Porquet D., Reeves J. N., Grosso N., Braito V., Lobban A., (2021), *The first simultaneous X-ray broadband view of Mrk 110 with XMM-Newton and NuSTAR*, A&A, 654, A89

Poutanen J., Svensson R., (1996), *The Two-Phase Pair Corona Model for Active Galactic Nuclei and X-Ray Binaries: How to Obtain Exact Solutions*, ApJ, 470, 249

Rees M. J., (1984), *Black Hole Models for Active Galactic Nuclei*, ARA&A, 22, 471

Reis R. C., Fabian A. C., Miller J. M., (2010), *Black hole accretion discs in the canonical low-hard state*, MNRAS, 402, 836

Remillard R. A., McClintock J. E., (2006), *X-Ray Properties of Black-Hole Binaries*, ARA&A, 44, 49

Reynolds C. S., (2021), *Observational Constraints on Black Hole Spin*, ARA&A, 59

Rhoades C. E., Ruffini R., (1974), *Maximum Mass of a Neutron Star*, Phys. Rev. Lett., 32, 324

Ross R. R., Fabian A. C., (2005), *A comprehensive range of X-ray ionized-reflection models*, MNRAS, 358, 211

Rybicki G. B., Lightman A. P., (1979), *Radiative processes in astrophysics*

Sabbadini A. G., Hartle J. B., (1973), *Upper Bound on the Mass of Non-Rotating*

Neutron Stars, Ap&SS, 25, 117

Salpeter E. E., (1964), *Accretion of Interstellar Matter by Massive Objects.*, ApJ, 140, 796

Schmidt M., (1963), *3C 273 : A Star-Like Object with Large Red-Shift*, Nature, 197, 1040

Sesana A., Barausse E., Dotti M., Rossi E. M., (2014), *Linking the Spin Evolution of Massive Black Holes to Galaxy Kinematics*, ApJ, 794, 104

Shakura N. I., Sunyaev R. A., (1973), *Black holes in binary systems. Observational appearance.*, Astronomy & Astrophysics, 24, 337

Shapiro S. L., Lightman A. P., Eardley D. M., (1976), *A two-temperature accretion disk model for Cygnus X-1: structure and spectrum.*, ApJ, 204, 187

Sobolewska M. A., Papadakis I. E., (2009), *The long-term X-ray spectral variability of AGN*, MNRAS, 399, 1597

Soldi S., et al., (2014), *Long-term variability of AGN at hard X-rays*, A&A, 563, A57

Steiner J. F., García J. A., Eikmann W., McClintock J. E., Brenneman L. W., Dauser T., Fabian A. C., (2017), *Self-consistent Black Hole Accretion Spectral Models and the Forgotten Role of Coronal Comptonization of Reflection Emission*, ApJ, 836, 119

Strüder L., et al., (2001), *The European Photon Imaging Camera on XMM-Newton: The pn-CCD camera*, A&A, 365, L18

Szanecki M., Niedźwiecki A., Done C., Klepczarek Ł., Lubiński P., Mizumoto M., (2020), *Geometry of the X-ray source 1H 0707-495*, A&A, 641, A89

Szanecki M., Niedźwiecki A., Zdziarski A. A., (2021), *Relativistic Reflection in NGC 4151*, ApJ, 909, 205

Tanaka Y., Inoue H., Holt S. S., (1994), *The X-Ray Astronomy Satellite ASCA*, PASJ, 46, L37

Tanaka Y., et al., (1995), *Gravitationally redshifted emission implying an accretion disk and massive black hole in the active galaxy MCG-6-30-15*, Nature, 375, 659

Tananbaum H., Gursky H., Kellogg E., Giacconi R., Jones C., (1972), *Observation of a Correlated X-Ray Transition in Cygnus X-1*, ApJ, 177, L5

Tchekhovskoy A., Narayan R., McKinney J. C., (2010), *Black Hole Spin and The Radio Loud/Quiet Dichotomy of Active Galactic Nuclei*, ApJ, 711, 50

Thorne K. S., (1974), *Disk-Accretion onto a Black Hole. II. Evolution of the Hole*, ApJ, 191, 507

Tombesi F., Sambruna R. M., Reeves J. N., Braito V., Ballo L., Gofford J., Cappi M., Mushotzky R. F., (2010), *Discovery of Ultra-fast Outflows in a Sample of Broad-line Radio Galaxies Observed with Suzaku*, ApJ, 719, 700

Turner M. J. L., et al., (1989), *The large area counter on Ginga.*, PASJ, 41, 345

Urry C. M., Padovani P., (1995), *Unified Schemes for Radio-Loud Active Galactic Nuclei*, PASP, 107, 803

Weisskopf M. C., Brinkman B., Canizares C., Garmire G., Murray S., Van Speybroeck L. P., (2002), *An Overview of the Performance and Scientific Results from the Chandra X-Ray Observatory*, PASP, 114, 1

Wilkins D. R., Fabian A. C., (2011), *Determination of the X-ray reflection emissivity profile of 1H 0707-495*, MNRAS, 414, 1269

Wilkins D. R., Fabian A. C., (2012), *Understanding X-ray reflection emissivity profiles in AGN: locating the X-ray source*, MNRAS, 424, 1284

Wilkins D. R., Kara E., Fabian A. C., Gallo L. C., (2014), *Caught in the act: measuring the changes in the corona that cause the extreme variability of 1H 0707-495*, MNRAS, 443, 2746

Yamada S., Makishima K., Done C., Torii S., Noda H., Sakurai S., (2013), *Evidence for a Cool Disk and Inhomogeneous Coronae from Wide-Band Temporal Spectroscopy of Cygnus X-1 with Suzaku*, PASJ, 65, 80

You B., et al., (2021), *Insight-HXMT observations of jet-like corona in a black hole X-ray binary MAXI J1820+070*, Nature Communications, 12, 1025

Zdziarski A. A., De Marco B., (2020), *Two Major Constraints on the Inner Radii of Accretion Disks*, ApJ, 896, L36

Zdziarski A. A., Gierliński M., (2004), *Radiative Processes, Spectral States and Variability of Black-Hole Binaries*, Progress of Theoretical Physics Supplement, 155, 99

Zdziarski A. A., Johnson W. N., Magdziarz P., (1996), *Broad-band γ-ray and X-ray spectra of NGC 4151 and their implications for physical processes and geometry.*, MNRAS, 283, 193

Zdziarski A. A., Banerjee S., Chand S., Dewangan G., Misra R., Szanecki M., Niedzwiecki A., (2023a), *Black hole spin measurements in LMC X-1 and Cyg X-1 are highly model-dependent*, arXiv e-prints, p. arXiv:2308.06167

Zdziarski A. A., Veledina A., Szanecki M., Green D. A., Bright J. S., Williams D. R. A., (2023b), *Evidence for a Black Hole Spin-Orbit Misalignment in the X-Ray Binary Cyg X-1*, ApJ, 951, L45

Zhang S. N., Cui W., Chen W., (1997), *Black Hole Spin in X-Ray Binaries: Observational Consequences*, ApJ, 482, L155

Zhang S.-N., et al., (2020), *Overview to the Hard X-ray Modulation Telescope (Insight-HXMT) Satellite*, Science China Physics, Mechanics, and Astronomy, 63, 249502

Zoghbi A., Fabian A. C., Uttley P., Miniutti G., Gallo L. C., Reynolds C. S., Miller J. M., Ponti G., (2010), *Broad iron L line and X-ray reverberation in 1H0707-495*, MNRAS, 401, 2419